IMPEDANCE-BASED ANALYSIS AND MATHEMATICAL MODELLING OF IMMUNOSENSOR BIOLAYERS

ANDREW PETER HENDERSON

Doctor of Philosophy (PhD)

Teesside University

October 2010

This research project was carried out as part of an Engineering and Physical Sciences Research Council (EPSRC) CASE studentship and was done in collaboration with Immunodiagnostic Systems (IDS) Ltd.

Teesside University in Middlesbrough

Impedance-based Analysis and Mathematical Modelling of Immunosensor Biolayers

ANDREW PETER HENDERSON

Doctor of Philosophy October 2010

Abstract

A study to optimise an IgG based immunosensor is presented, that has been carried out by absorbing monolayers to a gold transducer surface at varying immersion times and temperatures. The theory and kinetics of monolayer adsorption are analysed and discussed.

Existing mathematical models are reviewed and experimentally researched, to highlight gaps in knowledge that would facilitate high quality, cost effective immunosensor production. The creation of two mathematical models to predict monolayer adsorption kinetics and optimal immersion times are discussed. Details are provided of how the new mathematical models may be advanced, and how the production of immunosensors may be further improved.

The first novel mathematical model (PTCS) has been created to model the presence of two sequentially forming structures on the surface of a substrate. It gives an insight into the percentages of each structure on the surface, along with the actual adsorption process. This model provides a good fit to all applicable experimental data and has allowed the deduction of optimum immersion times. The second novel model (PIF) provides a greater insight than existing models into the individual contributions to surface coverage by both random and island growth. This allows an insight into how the monolayer surface is covered, which is critical to determine the optimum conditions for adsorption. This model also provides a good fit to the isotherm data it has been applied to.

To provide a thorough understanding of the bulk properties of monolayer formation over the gold transducer, and how these properties vary with immersion time and temperature, various measurement techniques have been employed. Electrochemical Impedance Spectroscopy (EIS) has been the principle measurement technique used to measure the bulk properties, but confirmation studies have also been carried out including, Contact angle measurements, FTIR microscopy with BSA molecular labels, Fluorescence microscopy for small adsorbed molecules and AFM for layers assembled from macromolecules. The data generated from the different techniques show consistency with the arguments discussed in each instance.

Two different IgG adsorption processes have been compared. These include direct IgG addition and a multilayered streptavidin-based process. The results indicate that IgG molecules adsorbed via the streptavidin based multilayer process are more vertically orientated and have a higher packing density of IgG molecules.

Keywords: Self Assembled Monolayer, impedance-based immunoassay, Streptavidin, biotinylated IgG, mathematical adsorption modelling.

“Any intelligent fool can make things bigger; more complex and more violent. It takes a touch of genius - and a lot of courage-to move in the opposite direction.”

Albert Einstein

Acknowledgements

First and foremost, I would like to thank my wife Sarah for the inspiration, understanding, devotion and support she has afforded me over the duration of my PhD project.

I would also like to thank: fellow PhD students for their co-operation, the Teesside University members of academic staff that supported me (in particular, Dr Paul Russell for choosing to formally become the second supervisor of my PhD project during my final year of study and for his help up until that point and my Director of Studies, Prof. Zulfiqur Ali for providing me with the opportunity of studying for this PhD and allowing me freedom to work autonomously). I would also like to thank the Teesside University technical staff who provided me with significant help, the Teesside University administrative staff for helping to progress my PhD and providing me with the opportunity to develop my transferable skills and Dr David Pritchard for his support.

I would like to thank the EPSRC and Immunodiagnostic Systems (IDS) Ltd for funding to carry out this research project.

Finally, I would like to thank my Mother, Father and Brother, Julie, Peter and Matthew, for their love and support.

Author‟s Declaration

I confirm that all the novel material presented in this thesis is solely the work of the author: Andrew Peter Henderson.

Signature……..

Contents

List of Figures

electrodes whilst they are immersed in electrochemical solution (yellow).

Figure 4.2: Nyquist plots from the report by Pruneanu et al (2008), of gold (a) and gold modified electrode: Au-SAM (b); Au-SAM-activated (c); SAM-avidin (d); SAM-avidin-Biotin (e).

Figure 5.1: Demonstrating erosion rates in electropolishing: the low charge density and protective double layer slow the rate of erosion of low lying features; protruding features are afforded little double layer protection and have a high charge density resulting in a fast rate of erosion.

Figure 5.2: A typical Anodic current/ Cell voltage profile, showing physical effects occurring at the electrode interface over given potentials.

Figure 5.3: Showing redox ion diffusion vectors (arrows), electrode solution boundaries (solid line) and lines of equal concentration (dashed lines).

Figure 5.4: Shows the evolution of a cleaned working electrode surface as a function of piranha solution immersion time in an ultrasonic bath. Measurements were taken after the post mechanical polishing purified water ultrasonication step (initial) and after 15 minute intervals of piranha solution ultrasonication, up to an overall immersion time of 60 min.

Figure 5.5: Where: ―piranha clean" corresponds to a typical Nyquist plot yielded from an electrode that has undergone piranha cleaning. ―Contaminated electrode" corresponds to the post piranha clean EIS for the electrode which was tarnished.

Figure 5.6: Optical microscope images of the contaminated electrode (A), after polishing using 30 μm, 6 μm and 1μm (B), after 0.05μm alumina slurry polish (C) and after 30 electropolishing sweeps (D).

Figure 6.3: A diagrammatic representation of the structure of a mercaptopropionic acid monolayer. MPA molecules are shown as circles, with an MPA structure highlighted in grey; substrate molecules are shown in white and the black rhombus shows the inter-structural spacing.

Figure 6.4: A normalized impedance plot comparing the predicted values of the proposed adsorption isotherm models (H 40 ^{o}C, H 30 ^{o}C, H 25 ^{o}C, H 20 ^{o}C and H 4 ^{o}C), to the normalised experimental impedance data, obtained at 0.1 Hz, (D 40 ^{o}C, D 30 ^{o}C, D 25 ^{o}C, D 20 ^{o}C and D 4 ^{o}C).

Figure 6.5: Showing how final monolayer normalized impedance measured at 0.1Hz varies with immersion temperature as a result of monolayer structural differences.

Figure 6.6: Equivalent circuit modelling the behaviour of MPA-coated gold working electrode.

Figure 6.7: Nyquist impedance plots of a cleaned gold electrode (A) with its equivalent circuit fit (A‘) and MPA modified electrodes corresponding to: the 1st plateau formed at 20 ^{o}C (B), the 2nd plateau formed at 20 ^{o}C (C), the 1st plateau formed at 4 ^{o}C (D), the 2nd plateau formed at 4 ^{o}C (E) and corresponding equivalent circuit fits (B‘, C‘, D‘ and E‘ respectively).

Figure 6.8: ATR-FTIR spectra of MPA deposited on an Au substrate.

Figure 6.9: IRRAS spectra of MPA monolayers immobilized at 5 min, 15 min and 16 hrs. The spectrum shows a weak but apparent mode (1717-1750 (acids) C=O (H-bonded)), [see region of interest] that revealed the composition of MPA monolayer.

Figure 6.10: Area A: bare Au working electrode substrate surface available for binding to MPA to form the first Au-MPA structure; Area B: the area

occupied by the first MPA-Au structure which is available for binding to more MPA in solution, causing the formation of the second structure; Area C: the coverage of second structure, on which no further adsorption or reordering takes place.

Figure 7.1: Activation reaction stages showing sequential formation of O-acylisourea from EDC and an MPA carboxyl group (A), NHS-ester formation from O-acylisourea and NHS (B), a ligand (for example: biotin) binding to the activated carboxyl group (C) and the final carboxyl-ligand structure (D).

Figure 7.2: The contact angle that double distilled water forms with an MPA surface modified with EDC and NHS at an EDC/NHS solution immersion time of: A, 0 hrs; B, 0.167 hrs; C, 0.667 hrs and D, 2.5 hrs.

Figure 7.3: The FTIR reflectance profile of BSA powder showing peaks occurring in the range of 1500-1800 cm^{-1}, corresponding to the BSA primary and secondary amine groups.

Figure 7.4: IR profile of the surface the green layer indicates presence of the island boundary where blue indicates the surface of the activated layer covered in BSA and green the area of unactivated MPA. The 100 micron scale interval indicates the bounday must be long and thus the island of activated surface covers a substantial continuous area.

Figure 7.5: Shows fluorescent images for a slide immersed in EDC/NHS solution for 30 minutes. Each image represents a different area of the same substrate. Dark areas are known to show the location of unactivated MPA. The light grey areas are thought to show location of O-acylisourea and the intense white areas are thought to show the location of NHS-ester.

Figure 7.6: Fluorescent images for a slide immersed in EDC/NHS solution for 2.5hours. The slide is completely grey. This indicates the surface is completely activated by NHS-ester. Note, the slide appears to be grey instead of white because the image intensity has been reduced to allow a viable image to be produced.

Figure 7.7: The normalized impedance–time plot for the 22 ^{o}C. Five different stages of layer growth (denoted by 1, 2, 3, 4 and 5 in bold) are suggested by the isotherm.

Figure 7.8: Normalised raw EIS data at temperatures less than the Gyepi-Garbrah critical temperature (Tc) (Gyepi-Garbrah and Šilerová, 2001) of the MPA monolayer, discrete points show the actual experimental data. The lines show the calculated impedance from the fitted Henderson-Kisliuk model.

Figure 7.9: Raw EIS data at temperatures at temperatures greater than the Gyepi-Garbrah critical temperature (Tc) (Gyepi-Garbrah and Šilerová, 2001) of the MPA monolayer. The isotherm at 22 °C is also included for comparison. The discrete points show the actual experimental data. The lines show the calculated impedance from the fitted Henderson-Kisliuk model.

Figure 7.10: Graphs showing the trends exhibited by the fitted constants of the PTCS-Kisliuk model as a function of temperature. The approximate Gyepi-Garbrah Critical Temperature of the MPA is shown to illustrate how constants respond to transition at this temperature.

Figure 7.11: Graphs showing the trends exhibited by the fitted constants of the PTCS-PIF model as a function of temperature. The approximate Gyepi-Garbrah Critical Temperature of the MPA is shown to illustrate how constants respond to transition at this temperature.

Figure 8.1: Atomic force microscope (AFM) pictures of the streptavidin layer (a) An AFM image of a Streptavidin monolayer on a modified gold slide after an immersion time of 2h (b) An AFM image of an activated SAM on a gold coated glass slide substrate(for reference)

Figure 8.2: The fits exhibited by the PIF, Kisliuk, Langmuir and RSA adsorption models with normalised experimental total impedance data, at 0.1Hz, which were measured from working electrodes that had been immersed in streptavidin solution for various periods. The three stages of growth are also outlined where: A is the 1st stage of formation, where random adsorption is dominant; B is the 2nd stage of formation, where crystal growth is dominant, and C is the 3rd stage of formation which is controlled by the occupation of potential formation sites.

Figure 8.3: Kinetics of Streptavidin adsorption, using PIF model principles, where: Fs encompasses all forces encouraging random adsorption of Streptavidin to the substrate and Fi represents the additional interactions that only exist around Streptavidin crystals present on the substrate surface.

Figure 8.4: (A) The equivalent circuit used to simulate the behaviour of the MPA baseline impedance signal and the signals yielded from a Streptavidin monolayer after an immersion time of 0.5 h and 2.6 h; (B) The equivalent circuit used to simulate the behaviour of the impedance signal yielded from a Streptavidin monolayer after an immersion 1.25 h.

Figure 8.5: A complex impedance plot showing the variation in imaginary (Z‘‘) and real (Z‘) impedance brought about by the presence of streptavidin monolayers on a modified work electrode, as a function of immersion time in streptavidin solution.

Figure 9.1: AFM profile of a Streptavidin monolayer

Figure 9.2: AFM profile of the glass slide after an immersion time of 45min in biotinylated IgG solution at 21^{o}C

Figure 9.3: AFM profile of the glass slide after an immersion time of 2 hours in biotinylated IgG solution at 21^{o}C, showing how the layer is restructured as the nanoscopic islands grow and merge into a single monolayer. High lying features indicate the presence of b-IgG. Low lying features indicate the presence of the Streptavidin monolayer.

Figure 9.4: A plot of normalised impedance, at 0.1Hz, as a function of biotinylated IgG solution immersion time on a Streptavidin modified substrate, showing the fit achieved by the Kisliuk and Langmuir adsorption isotherms.

Figure 9.5: The equivalent circuit used to simulate the behaviour of a cleaned gold working electrode signal, the Streptavidin baseline impedance signal and the signals yielded after a b-IgG solution immersion time of 0 h, 15 min, 30 min and 2 h.

Figure 9.6: A complex impedance plot showing the variation in imaginary (Z‘‘) and real (Z‘) impedance brought about by the presence of biotinylated IgG monolayers on a modified work electrode, as a function of immersion time in biotinylated IgG solution.

Figure 10.1: Plot of normalised impedance versus immersion time for the immobilisation of IgG directly on to the metal substrate. Five data sets are shown each corresponding to one of the five isotherms at 4, 20, 27, 32 and 40 °C. The data sets at 27, 32 and 40 °C each show maxima in the curve which is indicative of an equilibrium existing between rate of formation of IgG orientated in the first structure and the rate of formation of second structure at these temperatures.

Figure 10.2: The AFM close contact profile of a gold surface at an adsorption temperature of 20 ^{o}C, showing a surface roughness of less than 1 nm;

Figure 10.3: The AFM close contact profile of an IgG monolayer adsorbed to a gold substrate surface.

Figure 10.4: Plot of the normalised impedance versus the immersion time for isotherms measured at 4 and 20 °C the graph also shows the curves derived from the Kisliuk and PIF models for the both isotherms. For the 4°C data set it is clear that the PIF model gives a much better fit of the data. For the 20°C data set no discernable difference is seen.

Figure 10.5: Plot of the normalised impedance versus the immersion time for isotherms measured at 27, 32 and 40 °C. The graph also shows the curves derived from the PTCS-Kisliuk and PTCS-PIF models for all isotherms. The fits achieved by the models appear to be in line with the uncertainty in the data.

Figure 10.6: Plot of the normalised impedance versus the immersion time for isotherms measured at 27, 32 and 40 °C with erroneous data points removed. The graph also shows the curves derived from the PTCS-Kisliuk and PTCS-PIF for the 27°C isotherm now line up perfectly indicating the Kisliuk model is less reliable when the base data set contain spurious data points.

Figure A2.1: Normalised Raw EIS data at temperatures less than the Gyepi-Garbrah critical temperature (Tc) (Gyepi-Garbrah and Šilerová, 2001) of the MPA monolayer. Discrete points show the actual experimental data, the lines show the calculated impedance from the fitted PTCS-Kisliuk model and PTCS-PIF model.

Figure A2.2: Raw EIS data at temperatures greater than the Gyepi-Garbrah critical temperature (Tc) (Gyepi-Garbrah and Šilerová, 2001) of the MPA monolayer. The isotherm at 22 °C is also included for comparison. The discrete points show the actual experimental data. The lines show the calculated impedance from the fitted PTCS-Kisliuk model and the PTCS-PIF model.

List of Tables

Table A5.3: Experimental and calculated impedances for the fitted Kisliuk model for the 40 °C isotherm.

Table A5.4: Experimental and calculated impedances for the fitted PTCS-PIF model for the 40 °C isotherm

Chapter 1: Introduction

Immunoassay involves employing antibodies to identify analyte molecules which are then detected as part of a diagnostic test. This technique is a well established method of testing and has been employed in a number of different industries including clinical chemistry analysis (Oellerich, 1980), medicine, domestic tests (such as pregnancy tests), veterinary diagnostics, drug screening, food, biowarfare and environmental tests (Ward and Morgan, 1993, Heineman et. al., 2001).

Target analyte molecules were first quantified in immunoassay tests using radiation measurements in conjunction with radioactive molecular labels (Yalow and Berson, 1960). In this test, target analyte molecules are bound to a known number of moles of monoclonal IgG antibodies, serving to block antigen binding sites on the antibodies. Radio labelled antigen molecules are then added to the solution and saturate the remaining unblocked antigen binding sites on the remaining antibodies. The radiation emitted by the end processed sample, consisting solely of radio labelled-antibody conjugates and target analyte-antibody conjugates, is then measured and correlated to the amount of analyte present in the sample.

This method of measurement has the obvious disadvantage in that radiation is hazardous to health. To eliminate this problem, the Enzyme Linked Immunosorbent Assay (ELISA) was developed (Van Weemen and Schuurs, 1971), which involves the use of enzymes to facilitate the conversion of a species of aqueous molecule to a fluorescing compound from a non-fluorescing compound. The initial rate at which these molecules are made to fluoresce is either proportional or inversely proportional to the concentration of target analyte in the sample (depending on the type of ELISA used). The preferred method of quantification for ELISA is therefore spectroscopy based.

Though ELISA is still a widely used type of immunoassay, electrochemical immunoassays (ECIAs) have recently been developed, which rely on the direct application of electrical current to the immunoassay system to quantify the amount of analyte present (Heineman et. al., 2001). Advantages that electrochemical immunoassays have over ELISA are that electrochemical immunoassay can be used to

detect analyte in optically dense samples and it is more amenable to miniaturisation without compromising sensitivity or increasing cost. Moreover, certain types of electrochemical immunoassay can detect the target analyte directly, eliminating the need for costly and time consuming labelling procedures (Tweedie et. al., 2006).

As immunoassays have been so widely used, there has been a great deal of research conducted into improving the reproducibility, stability, sensitivity, shelf life and limit of detection of immunoassay sensors (also known as immunosensors). In instances where the immunosensor is dependent on the target analyte binding to an antibody modified planar surface, these factors are normally largely dictated by the means in which the antibodies have been attached to the antibody modified surface (Diaz-Gonzalez et al., 2005).

For example, the method of antibody immobilisation to the surface dictates a number of antibody monolayer properties including: the degree of freedom antibodies have to move over the surface whilst in solution, the orientation in which antibodies bind to the surface and how readily the antibody layer will desorb from the surface during measurement. Hence, the effective attachment of antibody monolayers to the surface of a substrate usually involves the prior attachment of one or more molecular layers to fasten the antibody layer to the surface in the desired manner.

One method of achieving this is through direct adsorption. Here, the surface that is eventually to be modified with antibodies is immersed in a solution containing the appropriate molecular layer molecule in the aqueous phase. The surface is then left in solution for a certain immersion time to enable a complete molecular layer to form across it. Monomolecular layers (monolayers) are commonly adsorbed to the surface using this method and it is normal to sequentially adsorb several monolayers to the surface before antibody attachment. In this report, the antibody layer and the monolayers associated with binding the antibodies to the surface are collectively referred to as the ~~"b~~iolayer."

From an economic and efficiency point of view, it is important to weigh sensitivity, time of response, reproducibility and accuracy against the cost of immunosensor

manufacture, including the cost of the time taken to manufacture them. It is therefore, important to design each molecular layer required to attach the antibody to the surface. Such design work commonly involves the use of mathematical models. However, little academic literature exists regarding the cost effective design and optimisation of these layers using mathematical design equations.

1.1 Project brief

The aim of this project was to help to address this issue by developing mathematical design equations for use in immunosensor design. This allows the optimum immersion time to be determined via calculation. These equations were then compared to existing models and fitted to adsorption data obtained at different temperatures. The mathematical models developed could then be used in conjunction with experimental studies to provide insight into adsorption kinetics involved in monolayer formation. This would facilitate understanding of how monolayers form across the surface, providing an indication into how adhesion of subsequent monolayers would be affected by employing immersion times that are either too long or too short.

Chapter 2 Measurement and Electrochemical Modelling Techniques for Individual Monolayer Formation

2.1 Introduction

Before any systematic study of biosensor manufacture can be initiated, a thorough understanding of the techniques used to measure biolayer characteristics and possible modelling techniques are required. This chapter discusses the extant techniques used to evaluate the formation processes and surface properties of biosensors. It pays particular attention to the use of electrochemical impedance spectroscopy (EIS, as defined by Bard and Faulkner, 2001, Guan et al, 2004), which is the principle measurement technique used over the course of this project. This technique has grown in importance recently as a means of sensitive, non-destructive testing for electrode surface characterisation, as it provides valuable information pertaining to the kinetic processes occurring at the electrode surface (Norlin et al, 2002) and has been featured in studies by Casalini et. al. (1997), Sapper et. al. (2006), Garc et. al. (2008), Booth et al (2009).

2.2 Surface profiling techniques.

A wide range of techniques have been used to characterise the surface properties of protein layers. The particular technique selected to measure a surface property depends on the property being measured and the accuracy that is required.

2.2.1 Photon-based Spectroscopic techniques

Spectroscopic techniques are widely used and can give very accurate detailed information about the nature of the surface of the biolayer for point measurements. In some cases the surface of the sample examined can be increased from a point source to a very small area by the use of a raster scan, involving sweeping the detection beam over the area being profiled. The method however is not practicable for examining the whole surface of the biolayer for biosensors. Specific details of individual techniques are given below.

2.2.1.1 Auger electron spectroscopy (AES)

This Technique uses a focused electron beam to stimulate the emission of Auger electrons on the protein layer under vacuum. Individual atoms are identified by measuring the energies of the emitted electrons, which are unique to an atom of a

specific element. This technique is very accurate but it has a number of disadvantages over alternative techniques. The method is damaging to organic material and is generally not recommended for use for protein layer measurement (B. D. Ratner, 1993). Other disadvantages are that it is only practicable to measure at a single point and that a vacuum must be maintained during measurement, which does not allow insitu measurements.

2.2.1.2 X-ray Photoelectron Spectroscopy (XPS)

During this procedure, X-rays are used to cause the emission of electrons with an energy that is characteristic of a particular element. XPS is capable of extracting surface information such as the empirical formula, chemical state, molecular orientation and electronic state of the elements. This technique is also a very accurate means of surface profiling. However, there are two main disadvantages to using this technique. These are that a very low pressure vacuum must be maintained above the substrate for the technique to be effective and that only a small area can be practicably profiled using the technique in conjunction with a raster scan.

2.2.1.3 Secondary ion mass spectrometry (SIMS)

This procedure analyses the composition of a surface by sputtering the sample surface under vacuum with a focused primary ion beam and collecting and analysing ejected secondary ions. The secondary ions are measured using a mass spectrometer to determine the elemental, isotopic, or molecular composition of the surface. SIMS has an even greater sensitivity than XPS and AES and is able to detect elements present in the parts per billion range.

2.2.1.4 Scanning electron microscopy (SEM)

A SEM is often employed for two uses, including imaging both the topography and composition of a small sample of the substrate surface. This procedure is a profiling technique that sweeps a high energy electron beam over the surface of a sample in a raster scan pattern, whereby a small area of the sample surface is profiled. The interactions between the beam electrons and the electrons of the sample surface atoms cause the emission of secondary electrons, Back Scattered Electrons (BSE) and X-rays. All of which are quantifiable signals.

Secondary electrons are normally used to determine surface topography as the number of secondary atoms to hit the detector is dictated by the sample surface topography. The BSE signal consists of back scattered beam electrons, resulting from an inelastic collision between the electron beam and an atom on the sample substrate. Heavy elements have a greater tendency to scatter the beam electrons than light elements, hence, surface composition can be calculated by monitoring the BSE signal. Similarly, X-rays are emitted when the electron beam stimulates the removal of an inner shell electron from an atom on the substrate surface. This causes a higher energy electron from an outer orbital to transfer to the inner shell and release energy, in the form of a characteristic X-rays. These X-rays are used to identify the substrate composition and to measure the abundance of elements on the substrate surface.

The resolutions obtained using a SEM varies between models as the resolution is dictated by the size of the electron spot. Typically resolution falls between 1 nm and 20 nm although recent SEMs have been able to produce resolutions in the order of 10^{-1} nm (Roussel, 2009).

This method of spectroscopy has advantages over other types of conventional spectroscopy as it usually employs a raster scan, enabling the system to image a small area of the substrate instead of a single point on the surface.

2.2.1.5 Infra-Red spectroscopy

This method of measurement encompasses a wide range of techniques, for example IRRAS, FTIR, ATR-FTIR and ATR-IR. All of these techniques utilise focussed beam of Infra-Red radiation, hence they will all be considered together. The infrared spectrum of a sample is collected by passing a beam of infrared (IR) photons through the sample at three different wavelengths: near infra-red (14000–4000 cm^{-1}), medium infra-red (4000–400 cm^{-4}) and far infra-red (400–10 cm^{-1}).

As the IR beam passes through the sample, sample molecules rotate or vibrate when they absorb and are excited by IR photons at the particular wavelength that corresponds to the molecules‘ discrete energy levels. Hence, different covalent bonds absorb at different IR wavelengths allowing different molecules to be identified within the sample.

The advantage of this technique over other spectroscopic techniques is that it requires minimal sample preparation and no vacuum, however, it is not as sensitive as the spectroscopic techniques mentioned previously in sections 2.1.1.1. and 2.1.1.4.

2.1.1.6 Raman spectroscopy

This method of measurement involves a number of variations known widely as: SERS, SERRS and TERS. Raman spectroscopy involves using a beam of photons to excite analyte molecules from the ground state to a virtual energy state. The molecule then relaxes and emits a photon as it returns to a different rotational or vibrational state. The difference in energy between the original state and the new state causes the emitted photon's frequency to shift further away from the excitation wavelength (Turrell and Corset, 1996).

Emitted photons, therefore, provide vibrational information that is specific to the chemical bonds and the symmetry of molecules. This allows the identification of molecules on the surface via their ―fingerprint” spectra. Photons used in Raman spectroscopy are usually either in the visible range, near IR or near ultraviolet range.

Like IR techniques and unlike other spectroscopic methods, Raman spectroscopy measurements are convenient as they are not taken under a vacuum and have a sensitivity comparable to IR.

2.2.2 Scanning probe microscope techniques (SPM)

Scanning Probe Microscopy (SPM) is a microscopy discipline that measures and generates images of a planar surface using a fine probe to scan the sample. This probe moves across the surface in a raster scan of the specimen, and interacts with the surface as it does so. This raster scan typically encompasses a maximum area of the order of 10^2 μm. The quantitative data obtained from the probe-surface interaction is stored over the process of the raster scan and displayed as a function of position in a computer generated image when the scan is complete. Hence, qualitative and quantitative data is obtained during the use of SPM techniques.

The resolution provided by SPM techniques varies depending on the method of measurement used and some techniques have been found to provide atomic resolution. This can largely be attributed to the use of piezoelectric actuators, which are computer controlled and have the ability to move with a high degree of precision. Examples of SPM techniques include: Atomic Force Microscopy (AFM), Ballistic Electron Emission Microscopy (BEEM), Scanning Tunnelling Microscopy (STM), Scanning Electrochemical Microscopy (SECM) and Chemical Force Microscopy (CFM). SPM samples are often easy to prepare and don‘t require a vacuum, giving it an advantage over some spectroscopic techniques.

2.2.3 Quartz Crystal Microbalance (QCM)

Quartz Crystal Microbalances (QCMs) measure a mass deposited on a crystal by measuring the change in frequency of the quartz crystal resonator. The resonance of the crystal is altered by the addition or removal of a small mass at the surface of the acoustic resonator. QCM sensors have been found to be highly effective at quantifying the affinity of molecules, macromolecules and microscopic organisms to surfaces functionalized with recognition sites (Dean, 2008).

QCMs can be used under vacuum, in the gas phase and in liquid environments. By relating the change in mass to the change in frequency of the QCM‘s quartz crystal

resonator, mass densities down to a level of below 1 μg/cm^2 can easily be measured. Dissipation can also be measured to help analysis, which is a parameter quantifying the damping in the system and is related to the sample's viscoelastic properties. Unlike SPM and spectroscopic measurements, QCM takes into account the material present across the entire crystal surface, however, it is substantially less sensitive than some of the spectroscopic techniques.

2.2.4 Ellipsometry

Ellipsometry analyses the change of polarization of incident light, which is reflected off a sample, and has been reported to be able to measure down to a single atomic layer, Khoshman (2005). Ellipsometry is classified as being an optical technique for the investigation of the dielectric properties (complex refractive index or dielectric function) of thin films. This allows an insight to be gained into the fundamental physical parameters of the film and can be related to a variety of sample properties. These include electrical conductivity, chemical composition, crystal quality, and morphology.

2.2.5 Surface Plasmon Resonance (SPR)

SPR utilises surface plasmons to quantify the presence of adsorbate molecules across the surface of a thin film by causing them to resonate across the substrate surface. Surface plasmons are electromagnetic waves that travel in a direction parallel and in close proximity to the substrate surface interfacial boundary. Because the waves travel along the boundary of the substrate, surface plasmon oscillations are very sensitive to any change in the boundary. This allows features such as imperfections in the substrate surface and the adsorption of molecules to the substrate surface to be detected. The sizes of features reportedly detected by this technique are in the nanometre range (Schasfoort and Tudos, 2008).

2.2.6 Contact angle measurement

Contact angle measurements involve spotting an ultra–pure water droplet onto a surface under analysis and measuring the angle that the side of the droplet makes with the substrate surface (Figure 2.1). This droplet is approximately 1 mm in diameter and the ~~–e~~ontact angle" measured is used to deduce the average hydrophobicity of a particular layer. This is useful when attempting to detect the growth of a monolayer over a substrate.

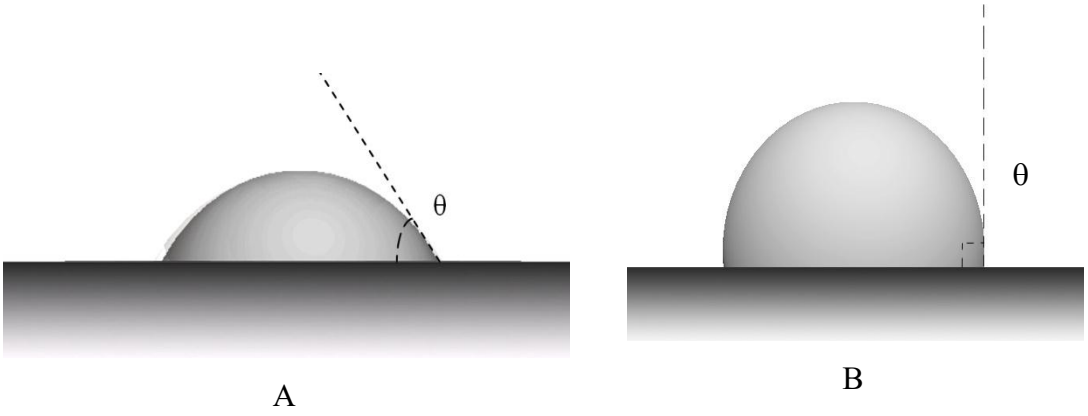

Figure 2.1 Contact angle measurement schematic, showing the water drop (semicircle), surface under analysis (rectangle) and angle under measurement (θ) for hydrophilic (A) and hydrophobic surfaces (B).

2.2.7 Electrochemical techniques

Such techniques commonly include EIS and Voltammetry. These techniques pass current through the metal substrate surface and are dependent on the charge transfer resistance, contributed to the circuit by the adsorbed layer over the surface of the substrate. Voltammetry involves applying a DC signal to an electrochemical cell causing current to flow between the electrochemical solution and substrate surface, making these techniques entirely dependent on measured charge transfer resistance. EIS, however, is dependent on an AC signal being applied between the electrochemical solution and working electrode. Hence, the EIS signal is also dictated by the dielectric properties of the monolayer, allowing additional monolayer properties to be measured (Yang et al, 2010).

2.3 Selection of the measuring techniques to be used in this study

The primary measurement technique for this study must be able to quantitatively detect the gradual adsorption of electrically insulating organic monolayers onto other insulating organic monolayers across the entire surface. In two instances, the adsorbate molecule of interest is in the order of Angstroms in size, making it difficult to detect using many conventional measurement techniques.

Labelling monolayer molecules with larger molecules or molecules that would emit light or increase the conductivity of the solution was considered as a primary quantitative method of measurement to facilitate the detection of the monolayers. However, molecular labels are often expensive and large labels introduce an element of steric hindrance, limiting the detection reaction rate and yield, contributing to measurement inaccuracies.

EIS was chosen as the primary measurement technique for this study because it is quantitative, non-destructive and able to measure the properties of thin layers by taking an average measurement of all monolayer molecules over the entire substrate surface. A number of back up techniques analysing a small portion of the substrate surface were selected to support the primary measurements. These techniques were selected on an individual basis where the specific properties of the layer formed were considered in conjunction with the advantages of the measurement technique employed. The measurements used included Contact angle measurement (as discussed in section 2.2.7), Fourier Transform Infra Red (FTIR) Microscopy and Fluorophore labelling and imaging for carboxylic group activation analysis. Larger protein molecules were profiled using an Atomic Force Microscope.

2.4 Electrochemical impedance spectroscopy

2.4.1 Introduction

The detection of microbes using impedance was first proposed by Stewart et al (1899) who observed changes in the electrical impedance of a solution due to growth of bacteria and an increase in the levels of compounds that the bacteria produced. This type of impedance based detection is now known as Electrochemical Impedance Spectroscopy (EIS), as described by Bard and Faulkner (2001).

EIS, when used in conjunction with an aqueous solution of electrolyte and a redox mediator, is particularly well suited to the detection of adsorbed molecular species on the working electrode (Campuzano et al, 2006). The electrical properties of the adsorbed species can either be conductive or insulating and the information obtained by mathematically modelling the spectra can provide a useful insight into the properties of the adsorbed analyte layer and the kinetic processes occurring in the layer and at the solution interface.

2.4.2 The EIS method

The EIS detection signal is typically a low amplitude alternating current (AC) applied between two oppositely charged electrodes, usually in a solid or liquid electrochemical cell. The dielectric properties of electrochemical cell shift the applied signal giving a measurable response. The manner in which the signal alters is dictated by the type of EIS used. Both current and voltage are functions of impedance and can be used to determine the impedance of the electrochemical cell. During potentiostatic measurements, a fixed voltage is applied to the cell and the current response is measured, whereas in galvanostatic measurements a fixed current is applied to the cell and voltage shift is the measured response.

The size of the impedance signal is dictated by the impedance of the electrochemical cell, which in turn, is dependent on two factors: ―real" impedance and ―imaginary" impedance. Real impedance, also known as resistance, is dictated by the ability of the system to transfer charge from one electrode through an electrochemical cell to an electrode of opposite charge. Imaginary impedance, also known as reactance, is dictated by the ability of the electrochemical cell to block the electric field that induces the electrical detection signal. This ability is reflected in the electrochemical cell's ―relative permittivity" value (discussed in section 2.4.3).

Standard electrochemical impedance measurement systems normally consist of a ―working electrode," which periodically changes from being positively charged to being negatively charged, and a ―counter electrode," which always holds an equal and opposite charged to the working electrode. A third electrode is included to compensate for uneven charging effects in liquid electrochemical cells, which are due to small redox ion concentration gradients in solution that can shift electrode potential and increase noise. This electrode holds a constant potential, is situated near the working electrode and is termed the ―reference electrode." Other electrode configurations exist, which possess unique geometry and do not require a reference electrode as a result (Štulik et al, 2000).

Measurements are made by recording a number of A.C. detection signal measurements at different A.C. electrical frequencies to form a spectra usually displayed in either a ―Nyquist plot," also known as a complex impedance plot, or a ―Bode plot," which is a plot of total impedance and phase angle against frequency (Bard and Faulkner, 2001).

2.4.3 Electrochemical theory

2.4.3.1 Equivalent circuits

Even though EIS measurements do alter as a function of monolayer structure and fractional coverage of the substrate, it is often difficult to determine what the exact physical and chemical properties of the layer are directly from EIS measurements. To this end, ―equivalent circuits" were developed to provide a mathematical model for

the EIS behaviour of monolayers. These circuits are purely theoretical, where each component relates to a different physical property of the layer.

The first attempt to model electrochemical cells using equivalent circuits was proposed by Helmholtz (1853). He proposed that the models are simplified by treating the cells as a standard electric circuits and by using capacitors and resistors to simulate the resistive and capacitive effects of the electrochemical cell. To construct such an equivalent circuit, a basic knowledge of the electrochemical system‘s sources of imaginary and real impedance contributions is required coupled with a knowledge of standard equivalent circuit models.

Since Helmholtz used the first equivalent circuit to model an electrochemical system, equivalent circuit systems have been refined by adding theoretical components to provide more advanced insights into the properties of the layer. One such element is the Warburg element (W1, Figure 2.2) that models mass transfer effects of redox ions on system impedance.

An example of a modern standard equivalent circuit for a bare working electrode in a standard three electrode, aqueous, electrochemical cell is shown in Figure 2.2, where R_s represents solution resistance, C_{dl} represents the double layer capacitance of the cell and R_{ct} represents charge transfer resistance.

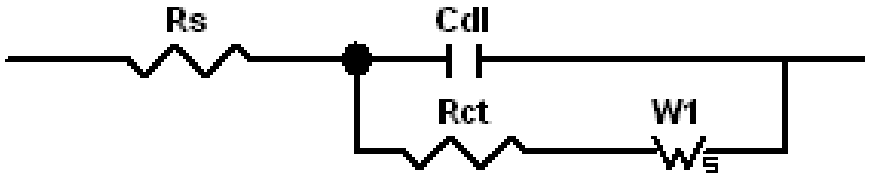

Figure 2.2 Standard equivalent circuit used for fitting the experimental results: R_{sol}, electrolyte resistance; R_{ct}, charge transfer resistance; C_{dl}, double-layer capacitance and W1, the finite-length Warburg impedance.

Both resistors and capacitors are assumed to be ~~“i~~deal,” which is to say that resistors do not make any contribution to the imaginary impedance and capacitors do not make any contribution to the real impedance. Thus, the real impedance for a resistor in an equivalent circuit is defined by Ohm‘s law, defined in equation (2.1), where Z‘ is real

impedance, I is electrical current flowing through the electrochemical system, and V is potential difference across the electrochemical system.

$$Z' = \frac{V}{I} \qquad (2.1)$$

2.4.3.1.1. Resistance elements

Resistors in equivalent circuits are used to model Ohmic resistances, contributed to the system through the leads and connections within the detection circuit; the resistance of the solution, which is independent of frequency but increases as a function of working electrode-counter electrode spacing, and the potential difference arising from electron transfer from a redox ion to an electrode.

2.4.3.1.2 Capacitance elements

The capacitance arises from the work of Helmholtz (1853). He observed that a double-layer is formed when an electrical current is passed through an electrode in a liquid electrochemical cell containing an electrolyte. The double layer consists of two layers: the inner Helmholtz plane (IHP), containing adsorbed solvent molecules, and the outer Helmholtz plane (OHP), consisting of ions electrostatically bound to the electrode. Further he drew an analogy between the electrochemical system and an ideal capacitor where the positively and negatively charged plates of the capacitor represent the electrode surface and OHP, respectively, in the electrochemical system. He proposed that the capacitance of the electrolytic cell is modelled to an acceptable degree of error in some electrochemical systems using an ideal capacitor in a circuit.

The capacitance of the equivalent circuit capacitor Helmholtz used to represent the electrolytic cell is defined in (2.2).

$$C = \frac{\varepsilon_r A}{d} \qquad (2.2)$$

where C is capacitance; ε_r is the relative permittivity of a homogeneous, dielectric layer; A is working electrode area; d is monolayer thickness; f is frequency, ω is radial frequency and Z'' is imaginary impedance. The relationship of capacitance to the imaginary impedance of the capacitor is defined in equation (2.3).

$$Z'' = \frac{1}{2\pi fC} = \frac{1}{\omega C} \qquad (2.3)$$

2.4.3.1.3 Gouy-Chapman theory.

Double layer capacitance can be modelled in some electrochemical systems using a capacitor in an equivalent circuit; the model is inaccurate as it fails to take into account the effects of electric field potential gradient on ion concentration as a function of distance perpendicular to the electrode surface. This effect becomes apparent at low electric field potentials and ionic concentrations (Bard and Faulkner, 2001), where the electric field potential weakens significantly as distance normal to the electrode surface increases.

The ion concentration profile along the surface normal gives the highest concentration of ions nearest to the electrode surface and decreases at an exponential rate with decreased field potential (which is inversely proportional to the square of distance along the electrode surface normal). Thus, a large potential gradient near the surface of the electrode, a low electrode potential or low concentration of ions in the bulk results in double layer thinning (Bard and Faulkner, 2001). Here, double layer thickness is defined as being the distance along the electrode surface normal where the ionic concentration is above that of the bulk solution.

To model this observation, Gouy and Chapman independently produced the idea of the existence of laminae consisting of different densities of charged ions, in place of the OHP, along the electrode surface normal (Bard and Faulkner, 2001). This gave rise to the model shown in equation (2.4), where n_i is the population of ions at a particular distance along the electrode surface normal, n_i^0 is the bulk concentration ion population, ϕ is measured potential with respect to the bulk solution, k_B is the Boltzmann constant, T is absolute temperature, z_i is the charge on ion i and e is the charge on an electron.

$$n_i = n_i^0 \exp\left(\frac{-z_i e\phi}{k_B T}\right) \qquad (2.4)$$

In terms of equivalent circuit design, when Gouy-Chapman behaviour is evident, it inevitably causes the double layer impedance behaviour to deviate from that of an ideal capacitor. For this reason, it can be helpful to model the double layer using a Constant Phase Element (CPE).

2.4.3.1.4 Constant Phase Element (CPE)

The constant phase element (CPE) was developed to model non-ideal capacitor behaviour which could include Gouy Chapman behaviour and non-homogenous, porous or incomplete dielectric layers, as the non-uniformity of the system commonly introduces a real impedance element. The CPE is shown in Figure 2.3 and defined by equation (2.5) where $|Z|_{CPE}$ is total impedance introduced by the CPE, n is a constant dictated by the non-ideal behaviour of the dielectric layer and Y_0 is a constant that is equal to capacitance when n is 1.

Figure 2.3: Standard CPE element notation

$$|Z|_{CPE} = \frac{1}{Y_0(j\omega)^n} \tag{2.5}$$

The amount of real and imaginary impedance contributed by this element is dictated by the constant: n, which occupies a value between 0 and 1, with n=0 being representative of a purely resistive component and 1 being representative of a purely capacitive element. Thus, the phase angle (ϕ, degrees) of the impedance contributed to the circuit by this element can be defined by equation (2.6).

$$\phi = 90n \tag{2.6}$$

2.4.3.1.5. Warburg Impedance elements

High frequency electrochemical system can be modelled successfully using capacitive and resistive elements alone. At lower frequencies mass transfer of redox ions in the system via diffusion have an increasing effect on the removal of charge from the surface of the electrodes thereby affecting the resistance and imaginary impedance, of the cell. This must be taken into account by using either infinite Warburg or finite Warburg impedance elements, defined in equations (2.7) and (2.9).

$$|Z| = \sigma/\omega^{0.5} - j\sigma/\omega^{0.5} \qquad (2.7)$$

The ‗infinite' Warburg impedance element equation (2.7) is most commonly used to model semi-infinite linear diffusion, i.e. the unrestricted diffusion of redox ions to a large planar electrode surface. An example of this is the transfer of redox indicator ions to and from a bare electrode in a single liquid phase. The Warburg coefficient ―σ," is used to account for the semi-infinite linear diffusion and is defined by equation (2.8).

$$\sigma = \frac{RT}{n^2F^2A\sqrt{2}}\left(\frac{1}{C_O^*\sqrt{D_O}} + \frac{1}{C_r^*\sqrt{D_r}}\right) \qquad (2.8)$$

Where A is electrode area, R is the universal gas constant, T is absolute temperature, F is the faraday constant, D_o is oxidant diffusion coefficient, D_r is reductant diffusion coefficient, C^*_o is oxidant concentration at the electrode surface, C^*_r is reductant concentration at the electrode surface and n is the number of electrons transferred in the electrochemical reaction (as dictated by electrochemical reaction stochiometry).

The ‗finite' Warburg impedance element is defined by equation (2.9) and is used to model the presence of thin porous layers over the surface of the electrodes. This term was originally developed to describe the diffusion of redox ions through a stagnant liquid film over the surface of an electrode and has been successfully applied to model the mass transfer effects brought about by a porous or inhomogeneous layer on the surface of an electrode. This is made possible through the use of the δ function, which

represents Nernst diffusion layer thickness. In this instance, D represents the diffusion coefficient for redox ions through the diffusion layer on the surface of the electrode.

$$|Z| = \frac{\sigma}{\sqrt{\omega}}(1 - j)\tanh\left(\delta\left(\frac{j\omega}{D}\right)^{0.5}\right) \qquad (2.9)$$

It can also be seen from equations (2.7) and equation (2.9) that the phase angle of the impedance contributed by the Warburg elements, are independent of frequency. The complex Warburg impedance yielded by the element remains constant at 45^{o}. As none of the Warburg element's variables alter with frequency other than radial frequency, it should be noted that a constant phase element can successfully substitute a Warburg impedance element in a complex impedance plot, provided the CPE constant _n' is 0.5. However, the Warburg element provides a better insight into monolayer properties.

2.4.3.2 Simulated Equivalent circuit elements in "ZView2" by Scribner associates, Inc.

Construction of an equivalent circuit is relatively simple however fitting parameters to accurately model the impedance data is complicated and time consuming. Commercial simulation packages such as –ZView2" by Scribner associates, Inc have been developed to overcome these difficulties (see Appendix 1 for further information).

2.4.4 Adapting the standard EIS measurements for use in surface adsorption studies.

EIS is an effective tool for determining the dielectric properties of an insulating layer over the surface of a working electrode and, when the data is analysed using equivalent circuits, it is a useful tool for determining the properties and fractional coverage of the adsorbed monolayer. However, to monitor the evolution and restructuring of an adsorbed layer it is necessary to make measurements at various time intervals.

A novel procedure is required to produce the time dependant measurements as it is not possible to make real time insitu measurements in the adsorption coating material. The recommended method involves submerging several working electrodes in an adsorption solution and sequentially withdrawing an electrode after each prescribed time interval. As each electrode is removed it is cleaned and immersed in the working electrochemical solution containing electrolyte and a redox mediator to form part of a standard electro chemical cell. It then requires a further 10 minutes to generate spectra. The resulting measurements can then be used to determine the time dependence of the measured normalised impedance.

2.5 Fourier Transform Infra Red (FTIR) Microscopy

Fourier Transform Infra Red (FTIR) Microscopy is a surface profiling technique used to obtain an Infra Red profile raster scan of a small portion of sample surface. The principle of operation is that a narrow beam of light (approximately 10 μm in diameter, to obtain optimum resolution) is directed at a particular point on the substrate surface and the IR spectrum at that point is measured. The beam then automatically moves to an adjacent 10 μm point and measures the IR spectra at that point. This process is repeated for each 10 μm wide row in turn until an IR profile for every 10 μm point in the sample area is obtained. A reference point is then measured to allow the FTIR equipment to distinguish between the IR profile of the substrate and the IR profile of the layer of interest. A specific wavelength is then selected and a 3 dimensional IR surface profile of the sample area is generated for that wavelength, measuring absorbance as a function of distance along the x and y axis.

In theory, the entire sample surface can be scanned using this technique but the practical maximum scan area is 325 μm x 500 μm and takes several hours to complete. Scans above this size are possible but can cause the detector to overheat resulting in a reduction of scan resolution.

2.6 Fluorophore labelling and imaging

The molecule size used to form some of the layers in this study was very small and the resolution of conventional microscopy techniques was too small to detect the layer growth. One option used to overcome this problem was to use fluorescent labelling. Fluorophore labelled molecules will emit light when excited by photons of a particular wavelength. These labels are attached only to the monolayer of interest.

Once the sample surface is labelled with the fluorophore molecule, it is placed under a microscope and a broad beam of monochromatic excitation light is projected onto the sample. The photons of monochromatic light excite electrons of the fluorophore molecules from a ground state to a high energy state. Once the molecules are no longer being excited by monochromatic light, they emit a photon of light from the lowest excited state and revert back to their ground state.

The emitted light is at a higher wavelength due to the Stokes shift and is observed through an optical microscope to reveal the position of the molecules of interest over the substrate surface.

2.7 Atomic Force Microscope (AFM)

The AFM is a scanning probe microscopy technique that images structures in the order of nanometres over a maximum area of 150 μm x 150 μm. This displays visible images of adsorbed biological species over the scanned surface of the substrate and provides definitive insights into molecular arrangement across the surface. It is only sensitive enough to measure macromolecule-based monolayers, such as protein monolayers and must be used in non contact mode to avoid damage to the layer of interest during measurement.

One of the most important components of the AFM is the probe tip, commonly with a tip radius of curvature in the order of nanometres, which is attached to a cantilever. The cantilever is suspended nanometres above the sample surface and oscillated at a frequency slightly above that of its resonant frequency, where the amplitude of oscillation is ≤ 10 nm. The oscillation frequency of the cantilever is decreased by the long range molecular forces that the sample surface exerts on the tip. Hence, the size of the change in oscillation is heavily dependent on surface topography.

To measure the change in cantilever oscillation, a laser beam is projected onto the cantilever and reflected to a detector consisting of an array of photodiodes (Figure 2.4). The manner in which the reflected laser beam travels over the detector array is dictated by the oscillating frequency of the cantilever, which is dictated by the topography of the sample. Once the topography of the sample has been measured in a particular position, the sample is moved so that the tip can profile a different point on the substrate. The tip is rastered over the sample surface in this way enabling an x-y plane to be profiled. As the data is gathered, computer software interprets the data and displays it as a 3D image. It also allows feature heights to be quantified.

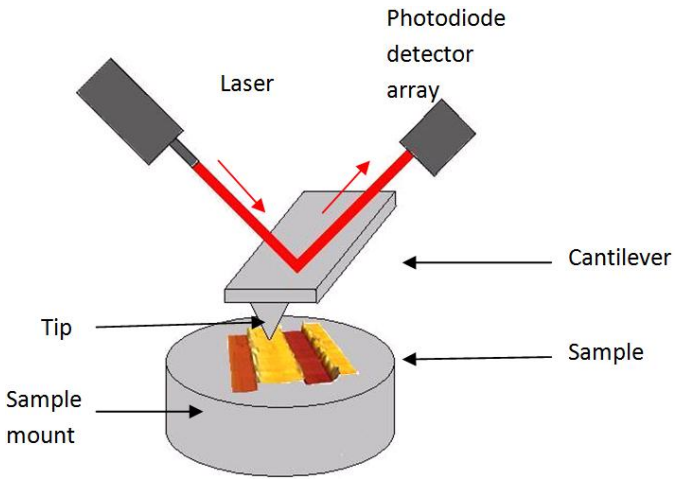

Figure 2.4: An AFM arrangement consisting of an oscillating cantilever profiling a sample surface as the changes in cantilever oscillating frequency are measured via laser beam.

2.8 Summary

EIS has been identified as principle measurement technique to be used to measure the bulk properties of the monolayers formed during biosensor construction. Equivalent circuit models are to be used to aid the interpretation of EIS data and provide an additional insight into adsorption kinetics. Confirmation studies can be carried out to support the EIS findings using a combination of different techniques including Contact angle measurements, FTIR microscopy and Fluorescence microscopy for small adsorbed molecules and AFM for layers assembled from macromolecules.

Chapter 3 Mathematical modelling of monolayer adsorption processes

3.1 Introduction

The individual stages of formation of a sequentially formed biosensor are basically a series of steps involving adsorption of a species onto either the bare metal substrate or a previously deposited monolayer. Given this, it should be possible to model any experimental data which describe the layer formation process using accepted adsorption models derived for other applications. If a suitable model is found, fitting the said model to the measured experimental data will provide values for the models' constants and will give some insight into the mechanisms taking place during monolayer formation.

To this end, different mathematical models have been applied to provide an insight into the kinetics and thermodynamics of monolayer systems, including the Kisliuk and Langmuir adsorption isotherm models to emulate small adsorbate molecule monolayers (Dannenberger et al, 1999) and the Random Sequential Adsorption model to emulate protein adsorption (Talbot, 2000).

However, experimental data often differs from these mathematical models for monolayer systems. The implication of this is that monolayer formation is more complicated than adsorption in gas systems which have formed the basis for most extant adsorption studies. Therefore, a re-evaluation of time and temperature adsorption theory with respect to monolayer processes is required. This is chapter will attempt to address this limitation.

3.2 Extant adsorption models

This section will give a brief overview of the main adsorption models that have been used to model adsorption in monolayers and their short comings. It concentrates on the time dependant forms of the equations that are of particular interest to modelling the monolayer formation processes.

3.2.1 The Freundlich adsorption isotherm

The first gas adsorption model was derived by Küster (1894) before it was modified in a report by Freundlich (1907) and subsequently termed the "Freundlich adsorption isotherm." This isotherm is empirical and is expressed in equation 3.1 where x is the

mass of final adsorbate present on the adsorbent, m is adsorbent mass, P is equilibrium adsorbate pressure and K and n are constants that are determined experimentally. As temperature increases, so too do the values of n and K.

$$\frac{x}{m} = KP^{\frac{1}{n}} \qquad (3.1)$$

This relationship has also been applied to adsorbates adsorbing to a solid adsorbent from a liquid phase see equation (3.2), where c is concentration of the adsorbate in the liquid.

$$\frac{x}{m} = Kc^{\frac{1}{n}} \qquad (3.2)$$

3.2.2 The Lagergren adsorption isotherm

Lagergren (1898) presented the earliest known semi-empirical first-order rate equation (Qui et al, 2009), describing the adsorption kinetic process in a liquid-solid phase system. The adsorbates used in the study were oxalic acid and malonic acid and the adsorbent was charcoal. The Lagergren adsorption isotherm equation is shown in equation (3.3), where the change of mass of adsorbate on the surface (q_t) with respect to time (t) is expressed as a function of the rate constant k_{pl} and the mass of adsorbate on the surface at equilibrium (q_e).

$$\frac{dq_t}{dt} = k_{pl}(q_e - q_t) \qquad (3.3)$$

Equation (3.3) can be expressed in terms of fractional coverage at time t ($\Theta_{(t)}$) by integrating between the limits of $q_t=0$ at t=0 and $q_t=q_t$ at t=t, and rearranged into equation (3.4).

$$\Theta = \frac{q_t}{q_e} = 1 - e^{-k_{p1}.t} \qquad (3.4)$$

3.2.3 The Langmuir adsorption isotherm

In reports published by Langmuir (1916 and 1918), another semi empirical model was developed to emulate the adsorption of gases to a solid adsorbate at equilibrium. This has proven to be the most popular adsorption model to date. Langmuir expressed the relationship shown in equation (3.5), between empty surface sites (S^*), adsorbate molecules (M) and filled particle sites (SM) was true for gas adsorbates adsorbing to

solid adsorbents. This allows the equilibrium constant for this process (K) to be expressed in equation (3.6).

$$S^* + M \leftrightarrow SM \tag{3.5}$$

$$K = \frac{[SM]}{[S^*].[M]} \tag{3.6}$$

Assuming SM is proportional to fractional coverage of the adsorbent (Θ), S* is proportional to 1-Θ, and M is proportional to the gas pressure or concentration (P), equation (3.6) can be rewritten as the "Langmuir adsorption isotherm" equation (3.7). This equation shows a relationship with a different rate constant, R.

$$R = \frac{\Theta}{(1-\Theta).P} \tag{3.7}$$

To maximize adsorbent surface coverage of adsorbate, an excess of adsorbate is often used in real adsorption systems. This makes the number of empty binding sites on the adsorbent the rate limiting step and P can be disregarded. This allows the Langmuir adsorption isotherm equation to be expressed using equation (3.8). Solving this equation forΘ, yields equation (3.9), where t is immersion time and $\Theta_{(t)}$ is the fractional coverage of the substrate surface at time t.

$$\frac{d\Theta}{dt} = R.(1-\Theta) \tag{3.8}$$

$$\Theta_{(t)} = 1 - e^{-Rt} \tag{3.9}$$

Equation (3.9) is similar to the Lagergren adsorption isotherm model reported as (3.4). However, fractional coverage described by Langmuir relates to a ratio of surface concentration at time t to surface concentration at equilibrium.

The objective function for the Langmuir adsorption isotherm model can be expressed as equation (3.10), where $z_{t(expt)}$ is the measured normalised impedance of the layer,

which varies depending upon fractional coverage and is the experimental data to which adsorption models are fitted in subsequent chapters. φ is a proportionality constant and is equal to the normalised impedance exhibited by the monolayer at equilibrium, which is 1 unless otherwise stated.

$$F(R,\varphi) = \sum \sqrt{\left(\varphi(1-e^{-Rt}) - z_{t(expt)}\right)^2} \qquad (3.10)$$

The Langmuir adsorption isotherm has been shown to provide an adequate fit to both gas-solid adsorption systems and liquid-solid adsorption systems. However, the model is based on the following assumptions, which are not true for all adsorption systems:

1. That the surface of the adsorbent is uniform and adsorption to every site is equally as probable.
2. Adsorbed molecules do not interact with themselves or with adsorbate in the adsorbate phase.
3. All adsorption occurs via the same kinetics.
4. At saturation, a monolayer is formed, potential binding sites are blocked by adsorbate molecules and molecules of adsorbate cannot form on molecules that have previously been adsorbed to the adsorbent.

3.2.4 Kisliuk adsorption isotherm

In some gas-solid adsorption systems, significant intermolecular interactions exist between adsorbed gas molecules and immobilised adsorbate at the adsorbent interface with the gas phase. This violates three of the four main assumptions upon which the Langmuir model is based, as the intermolecular interactions that are not modeled in the Langmuir model make adsorption of gas molecules to the surface more likely to occur around adsorbate molecules that are already present on the adsorbent surface and gives rise to two different types of adsorption mechanism. One of these two mechanisms is predominant for adsorbate forming around immobilised adsorbate on the adsorbent surface and the other is predominant for adsorbate forming in a remote

location on the adsorbent, where only interactions between the adsorbate and the adsorbent exist.

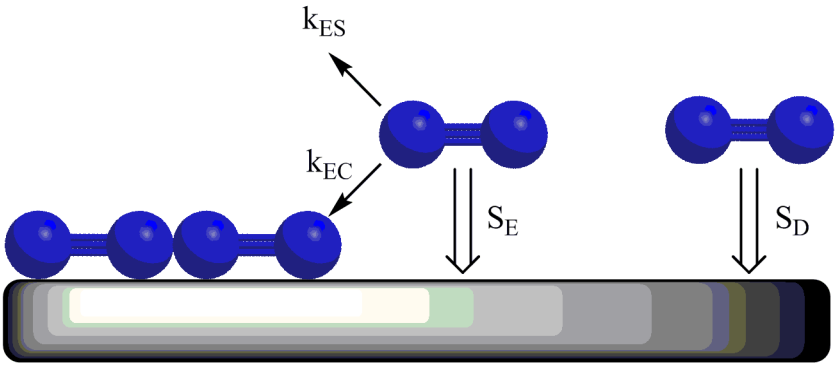

Figure 3.1: The experiment reported by Kisliuk (1957) where nitrogen adsorbate molecules (blue) are adsorbed to a tungsten adsorbent (faded grey surface). S_D is the probability of an adsorbate molecule randomly adsorbing to the surface from the precursor state, S_E is the probability of a molecule forming around an adsorbate molecule on the adsorbate surface from the precursor state, k_{EC} is the rate of adsorption around adsorbate molecules on the surface from the precursor state and k_{ES} is the rate of desorption from the precursor state into the bulk solution.

The effect of these intermolecular interactions on the Langmuir model was studied by Kisliuk **(**1957), where nitrogen was the gaseous adsorbate and tungsten was the solid adsorbent. To compensate for the affect of molecular interactions, Kisliuk proposed a ~~"~~precursor state" theory, which is present at the interface between the adsorbent and adsorbate. Nitrogen molecules would enter this state and would either adsorb to the tungsten surface or desorb back into the gaseous phase. The probability of adsorption occurring from the precursor state is dependent on the dominant adsorption mechanism. Kisliuk allocated different ~~"~~sticking probabilities" to the two adsorption mechanisms and used different constants to represent these probabilities in his mathematical model. The S_E constant alters depending on the probability of an adsorbate molecule forming around immobilised gas molecules on the adsorbent, from the precursor state (where there are significant interactions between gas on the adsorbent and adsorbate in the precursor state). If the adsorbate molecule is successfully adsorbed to the surface from the precursor state, it will do so at a rate of k_{EC} otherwise it will pass back into the gaseous phase at rate of k_{ES}. The S_D constant alters depending on the probability of an adsorbate molecule forming on the adsorbent at a location where intermolecular interactions only exist between the adsorbent and the molecule being adsorbed from the precursor state.

Each of these factors is illustrated in Figure 3.1 and were taken into account using a single –sticking coefficient" (k_E) in the adsorption model developed by Kisliuk. The relationship between k_E and the other constants is shown in equation (3.11).

$$k_E = \frac{S_E}{k_{ES} . S_D} \tag{3.11}$$

As all of the assumptions made in the development of the Langmuir adsorption isotherm hold true for the adsorption mechanism that dictates S_D, this constant can be assumed to be the adsorption rate constant. However, the rate constant for the Kisliuk model is expressed by R' as the additional variables introduced to the Kisliuk model affect the value of this rate constant, so it cannot be assumed to be the same as the Langmuir rate constant. In the case of the Kisliuk adsorption isotherm, R' is proportional to the square root of the adsorbate's diffusion coefficient and is representative of the sticking probability of an adsorbate molecule to a location that is remote from any immobilised gas molecules on the adsorbent surface (Dannenberger, 1999).

The precursor theory lead Kisliuk to derive the adsorption isotherm shown in equation (3.12) and expressed in terms of $\Theta_{(t)}$ in equation (3.13), where $\Theta_{(t)}$ is fractional coverage of the adsorbent with adsorbate, at immersion time t.

$$\frac{d\Theta}{dt} = R'(1-\Theta)(1+k_E\Theta) \tag{3.12}$$

$$\Theta(t) = \frac{1-e^{-R'(1+k_E)t}}{1+k_E e^{-R'(1+k_E)t}} \tag{3.13}$$

Hence, the objective function can be expressed in equation (3.14).

$$F(R', k_{E1}, \varphi) = \sum \sqrt{\left(\varphi \left[\frac{1-e^{-R'(1+k_E)t}}{1+k_E e^{-R'(1+k_E)t}} \right] - z_{t(expt)} \right)^2} \tag{3.14}$$

3.2.5 RSA adsorption isotherms

Random Sequential Adsorption (RSA) models are conventionally developed using statistical probability. One of the first RSA models was developed for a one dimensional adsorption model and was reported by Cohen et. al. (1963). This model related adsorption site occupancy and the time for which the adsorbent had been immersed in the adsorbate phase. As immersion time progressed, the model emulated the affect of depletion of adsorption sites leading to a decrease in adsorption rate with increased immersion time. The RSA model effectively emulated steric hindrance introduced by large adsorbate molecules, which prevents adsorption occurring to some unoccupied sites up to an infinite immersion time.

Around the same time, Rényi (1958) developed and published another one dimensional RSA model. This report introduced the theoretical concept of the ~~"c~~ar parking problem," which drew the analogy that the adsorbate molecules could be likened to theoretical ~~"r~~ods" (of length σ) adsorbing onto a line, representing the adsorbent (See Figure 3.2). Each of these Rods are randomly and sequentially dropped onto the surface of the line, at a rate of k_a. If the rods land on a site that is available for binding, they are adsorbed. However, they are rejected if they land across a rod, or two rods, which have been previously adsorbed to the surface.

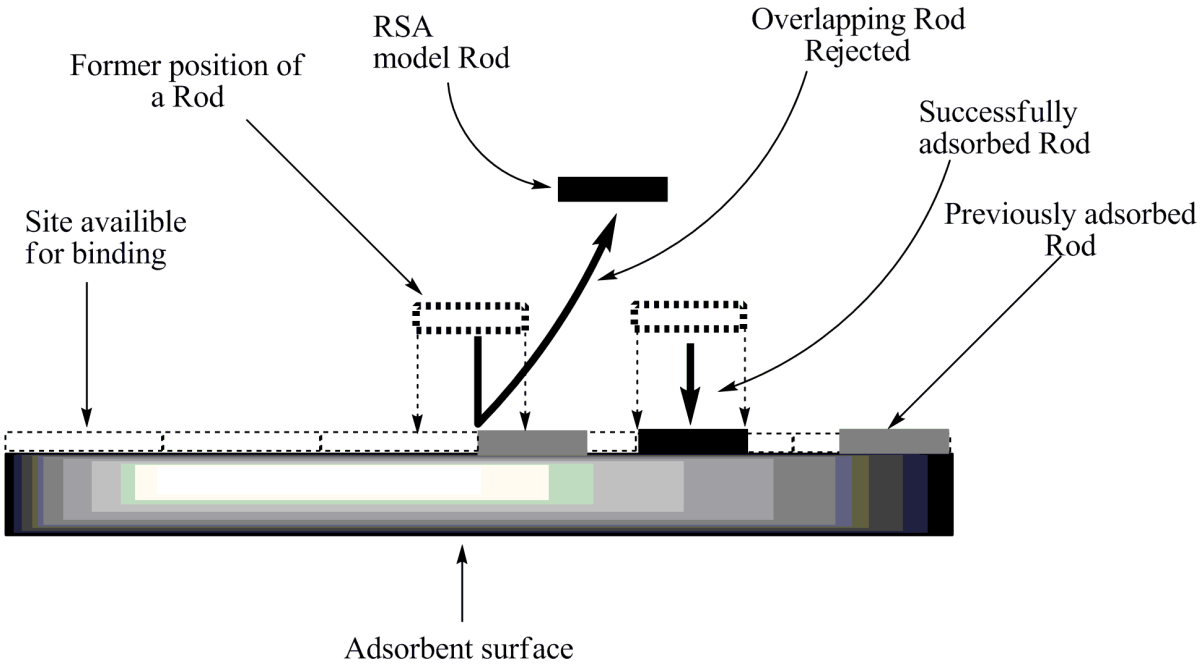

Figure 3.2: The car parking problem, as defined by Rényi (1958), where there are a fixed number of sites available for rod adsorption on the adsorbent surface, no forces exist between rods that encourage adsorption and a rod is rejected and desorbs into the adsorbate phase if it attempts to occupy a binding site already occupied with a previously adsorbed rod.

The initial rate of adsorption is high when there are only a few occupied sites and becomes increasingly unlikely as adsorption time increases and the number of available adsorption sites decrease. This relationship was expressed by Rényi (1958) in terms of rod number density on the surface, $\rho(t)\sigma$, after a given adsorption period, t (see equation 3.15), where $\rho(\infty)\sigma$ is the saturated rod density, k_a is the rate at which the rods are added to the surface, σ is the length of a rod and γ is the Euler constant.

$$\rho(t)\sigma \approx \rho(\infty)\sigma - \left(\frac{e^{-2\gamma}}{k_a\sigma}\right)\frac{1}{t} \tag{3.15}$$

This model was expanded on by Pomeau (1980) and Swendsen (1981) to model the adsorption of discs (representing the adsorbate) to a two dimensional adsorbent and assumes that no interactions exist between the discs being adsorbed to the substrate. The relationship is shown in equation (3.16), where D is the number of dimensions involved in adsorption and D = 2 in the case of adsorption to a planar adsorbent.

$$\rho(t) \approx \rho(\infty) - t^{-\frac{1}{D}} \qquad (3.16)$$

In another study, Schaaf et al. (1991) analysed the effect of diffusion on the accuracy of the model in equation (3.16) and found that a source of systematic error was introduced by diffusion. A new random sequential adsorption model was then developed (3.17) and was found to approximate the experimental data more accurately.

$$\rho(t) \approx \rho(\infty) - t^{-\frac{2}{3}} \qquad (3.17)$$

3.2.5.1 Monte Carlo Algorithms

An accurate computational way of predicting surface coverage, adsorption thermodynamics and rate of adsorption is to use Monte Carlo simulations. At each step in a Monte Carlo algorithm, a particle or molecule is potentially adsorbed in the simulation cell with periodic boundary conditions. The position of the adsorbed particle is dictated by a uniform probability distribution function dictated by interactions between the adsorbate and adsorbent, and between adsorbate molecules. Most adsorbents have a finite range, so most Monte Carlo algorithms divide the adsorbent area using a grid (Hinrichsen et al, 1986). As the grid sites become occupied with adsorbed molecules and the jamming limit is approached, the number of successful binding events asymptotically approaches zero. These grid sites are often sized to accommodate one particle to achieve the best results, where trial adsorption events of adsorbate particles or molecules take place within each element.

These Monte Carlo algorithms have been used extensively in various adsorption models, including RSA of non-spherical particles (Ricci et al, 1994), polymer adsorption (Wang, 1998), gas adsorption (Grabowski, 2002) and protein adsorption (Al-Mekhnaqi, 2006).

3.2.5.2 Adsorption of „Real" anisotropic molecules

Molecules and macromolecules often have a non-spherical shape and, in the case of biological molecules, adsorb irreversibly when a large surface area of the biological adsorbate is in contact with the adsorbent. Schaaf et al. (1992) empirically

determined that the maximum coverage of the adsorbent, which occurred during the adsorption of fibrinogen (a nonspherical protein with an aspect ratio of approximately 7.5) was around 40%, which was less than the saturation coverage predicted by the RSA of hard disks (55%). Similar effects were observed by Feder, (1980a), Feder, (1980b), Ramsden, (1993) and Mura-Galelli, (1991). A way to compensate for these effects involves considering the adsorption of anisotropic particles onto an adsorbent surface as being irreversible and applying a generalised rules to the RSA model, allowing the positions and orientations of the adsorbing particles to be chosen randomly from uniform distributions.

One such generalised RSA model was recently presented by Cortés and Valencia (2002). This model was determined by using a Monte Carlo algorithm to emulate adsorption of dimers and trimers on geometrically disordered substrates. The data that the Monte Carlo algorithm provided was then simplified into a semi-empirical formula that related adsorption time (t) to fractional coverage at time t [$\Theta_{(t)}$] and fractional coverage of a saturated substrate [$\Theta(\infty)$], using the semi-empirical proportionality constant: B. This formula is shown in equation (3.18) and is rearranged to express $\Theta(t)$ as a function of time in equation (3.19).

$$t = \frac{B}{\Theta(\infty) - \Theta(t)} . \Theta(t) \qquad (3.18)$$

$$\Theta(t) = \frac{t}{B + t} . \Theta(\infty) = \frac{t}{B + t} \qquad (3.19)$$

The objective function for the simplified RSA model is shown in equation (3.20).

$$F(B,\varphi) = \sum \sqrt{\left(\varphi \left[\frac{t}{B + t} \right] - z_{t(expt)} \right)^2} \qquad (3.20)$$

3.3 New adsorption isotherms

In spite of the wide variety of adsorption models that currently exist, there are two main short comings in adsorption theory that makes biosensor design difficult. The first is that there are no isotherm models in existence that use rate constants to describe island formation with time. Kisliuk made some progress by using empirically determined sticking coefficients but a rate constant based model would be more useful because it would enable direct comparison of island growth to random adsorption and provide an insight into the relative strengths of the interactions encouraging adsorption. This is especially useful when monitoring adsorption to the sensor surface where interactions exist between immobilised adsorbate on the surface and adsorbate in solution.

The second short coming is the absence of a model which emulates the formation of two different structures on an adsorbent, where the formation of one is a prerequisite to the formation of the other. Such a mathematical model is critical to emulate the formation of monolayers that form two different structures (sequentially). The mathematical model is also critical for the purposes of modelling the sequential adsorption of two different adsorbates to the surface, where one adsorbate forms over the surface as a function of time and the other adsorbate either replaces or forms a different structure on the adsorbent surface.

3.3.1 Proposed Island Formation (PIF) Adsorption Isotherm

The Proposed Island Formation (PIF) Adsorption Isotherm was developed to address problems arising from island formation. This new semi-empirical adsorption isotherm was developed specifically as part of the investigation featured in Chapter 8. The model considers adsorption to the surface as occurring through one of two mechanisms, either by ~~–r~~andom adsorption" (represented in equation (3.21)) or by ~~–i~~sland formation" (represented in equation (3.27)).

The model was specifically tailored to overcome the limitations of the extant adsorption isotherms in modelling the carboxyl group activation process but was also found to be applicable to adsorption processes featured in Chapters 8 to 10, where it frequently gave a much better insight into activation kinetics than extant models.

In order to develop a model that provides a better insight into the relative rates of random adsorption and island formation, it was decided to return to the original ideas proposed by Lagergern (1898) who assumed the adsorption process could be treated as being analogous to an equilibrium reaction. For example:

$$S + B \rightarrow SB \tag{3.21}$$

Where S is the sites available for adsorption, B the number of particles in solution and SB is the number of sites successfully occupied. In order for first order kinetics to apply the reaction must depend solely on the concentration of S therefore B is assumed to be very large and relatively unchanged by the reaction. From this equation a rate expression is derived for the rate of occupation of sites assuming the reaction proceeds as a pseudo first order process:

$$-\frac{dN_S}{dt} = k_R N_s \tag{3.22}$$

Where N_S is the moles of vacant sites at any time t and k_R is the rate constant for adsorption by random seeding.

On integration this becomes:

$$-(\ln N_{St} - \ln N_{S0}) = k_R t \tag{3.23}$$

And on rearrangement:

$$\left(\frac{N_{St}}{N_{S0}}\right) = e^{-k_R t} \tag{3.24}$$

Now the fractional surface coverage of the adsorbed species (Θ) can be defined as:

$$\Theta = \frac{(N_{S0} - N_{St})}{N_{S0}} \tag{3.25}$$

on substitution into equation (3.24) this gives:

$$\Theta = 1 - e^{-k_R t} \tag{3.26}$$

This equation could be used as the starting point for the new model. In the case of this adsorption process the desorption of bound species is thought to be small but there is a competing mechanism where adsorption takes place on the surface due to island growth around points where adsorption has already taken place due to random

adsorption. This process is therefore dependant on the concentration of adsorbed species already on the surface. It could be treated as being analogous to an auto catalytic reaction as shown in equation (3.27).

$$S + B + SB \rightarrow SB + SB \tag{3.27}$$

The equivalent rate equation for this autocatalytic process is:

$$-\frac{dN_S}{dt} = k_I N_S (N_{S0} - N_S) \tag{3.28}$$

For the new model the reactions described by equations (3.21) and (3.27) can be treated as parallel reactions to derive the rate expression given in equation (3.29)

$$\frac{dN_{SB}}{dt} = -\frac{dN_S}{dt} = k_I N_S (N_{S0} - N_S) + k_R N_S \tag{3.29}$$

This can be rearranged to separate the variables

$$\left[\frac{1}{(k_I (N_{S0} - N_S) + k_R) N_S}\right] dN_S = -dt \tag{3.30}$$

The RHS of equation (3.30) can now be manipulated by the use of partial fractions

$$\frac{1}{(k_I (N_{S0} - N_S) + k_R) N_S} = \frac{A}{(k_I (N_{S0} - N_S) + k_R)} + \frac{C}{N_S} \tag{3.31}$$

The constants A and C are given in equations (3.32) and (3.33).

$$\text{A} = \frac{k_I}{k_R + k_I N_{S0}} \tag{3.32}$$

$$\text{C} = \frac{1}{k_R + k_I N_{S0}} \tag{3.33}$$

Substitution of equations (3.31)-(3.33) into equation (3.30) and multiplying both sides by ~~–(~~$k_R + k_I N_{SO}$)" yields equation (3.34).

$$-\int_{N_{S0}}^{N_{St}} \left[\frac{k_I}{k_I (N_{S0} - N_S) + k_R} + \frac{1}{N_S}\right] dN_S = \int_0^t (k_I N_{S0} + k_R) dt \tag{3.34}$$

On integration this becomes:

$$\ln\left[\frac{N_{S(t)}k_R}{N_{S(0)}\left(N_{S0}k_I + k_R - k_I N_{S(t)}\right)}\right] = -(k_R + k_I N_{S0})t \tag{3.35}$$

Equation (3.35) can be rearranged to give:

$$\frac{N_{S(t)}}{N_{S0}} = \frac{(k_R + k_i N_{S0})e^{-(k_R + k_i N_{S0})t}}{k_R + k_I N_{S0} e^{-(k_R + k_i N_{S0})t}} \tag{3.36}$$

It is now possible to substitute using equation (3.25)

$$\Theta = 1 - \frac{(k_R + k_I N_{S0})e^{-(k_R + k_i N_{S0})t}}{k_R + k_I N_{S0} e^{-(k_R + k_i N_{S0})t}} \tag{3.37}$$

Note $k_I N_{S0}$ is a constant that depends on the initial concentration of sites available and could be represented as k_I' and equation (3.37) could be further simplified to give the working equation:

$$\Theta = \frac{k_R - k_R e^{-\left(k_R + k_I'\right)t}}{k_R + k_I' e^{-\left(k_R + k_I'\right)t}} \tag{3.38}$$

Hence, the PIF's objective function is defined as:

$$F(k_R, k'_I, \varphi) = \sum \sqrt{\left(\varphi\left[\frac{k_R - k_R e^{-\left(k_R + k'_I\right)t}}{k_R + k'_I e^{-\left(k_R + k'_I\right)t}}\right] - Z_{(t)expt}\right)^2} \tag{3.39}$$

3.3.2 Proposed Two Component Sequential (PTCS) Adsorption Isotherm

The Proposed Two Component Sequential (PTCS) Adsorption Isotherm was developed to address the problems of the sequential formation of different structures on a surface. It was specifically required as part of this work to emulate the adsorption and behaviour of SAM molecules on the surface of a gold substrate, and is discussed

in greater detail in Chapter 6 section 6.5.1 and was published as Henderson et al (2009). The EIS study that was conducted to obtain the data which formed the basis for the model, showed the evolution of two different structures over the surface of the substrate, one of which formed rapidly and had high impedance, the other took significantly longer to form and had a much lower impedance. However, it was necessary for the first structure to form on an area of the substrate before the second structure could form. Hence, the expressions in equations (3.40), (3.41) and (3.42) were derived to describe the system, where Θ_{Total} is the total fractional coverage of the substrate with adsorbate, Θ_1 is the fraction of the surface covered with the first structure at a certain immersion time, Θ_2 is the fractional coverage of the substrate surface with the second structure, Θ_{S0} is the available fraction of the substrate for adsorbate to form on and $\Theta_{1(t)}$ and $\Theta_{2(t)}$ are fractional coverage of structure one and structure two as a function of immersion time.

$$\Theta_{Total} = \Theta_1 + \Theta_2 \tag{3.40}$$

$$\Theta_1 = \Theta_{S0}.\ \Theta_{1(t)} - \Theta_2 \tag{3.41}$$

$$\Theta_2 = \Theta_{1(t)} - \Theta_{2(t)} \tag{3.42}$$

The impedance signals yielded by a complete covering of each structure are known to be different. To account for these differences constant φ_1 is said to correspond to the peak coverage of structure 1 on the surface and constant φ_2, corresponds to the final concentration of structure 2 on the surface. These expressions were combined to give the PTCS model (shown in equation (3.43)), which predicts the normalised impedance signal yielded from the adsorbate monolayer layer (z_t) as a function of immersion time. The values of $\Theta_{1(t)}$ and $\Theta_{2(t)}$ are determined using standard single component adsorption isotherms such as the Langmuir, RSA, Kisliuk and PIF models. In the instance of the PTCS model used in this investigation, the Kisliuk and PIF adsorption isotherms were used to calculate $\Theta_{1(t)}$ and $\Theta_{2(t)}$ values. The specific

formulae used to define $\Theta_{1(t)}$ and $\Theta_{2(t)}$ are shown in equations (3.44) and (3.45), where the subscript ~~"n~~" can either be equal to 1 (denoting variables relating to structure 1) or 2 (denoting variables relating to structure 2).

$z_t = \Theta_{1(t)}.[\varphi_1(1-\Theta_{2(t)}) + \varphi_{2.}\Theta_{2(t)}]$

$$\Theta_{n(t)} = \frac{1 - e^{-R_n'(1+k_{En})t}}{1 + k_{En}e^{-R_n'(1+k_{En})t}} \tag{3.44}$$

$$\Theta_{n(t)} = \frac{k_{Rn} - k_{Rn}e^{-\left(k_{Rn}+k'_{In}\right)t}}{k_{Rn} + k'_{In}e^{-\left(k_{Rn}+k'_{In}\right)t}} \tag{3.45}$$

The objective functions can therefore be defined in equations (3.46) and (3.47) for the PTCS-Kisliuk and PTCS-PIF models respectively.

$$F\left(R_1, R_{2,} k_{E1}, k_{E2}, \varphi_1\ , \varphi_2\right) = \sum \sqrt{\left(\frac{1-\mathrm{e}^{-\mathrm{R}_1(1+\mathrm{k}_{\mathrm{E}1})\mathrm{t}}}{1+\mathrm{k}_{\mathrm{E}1}\mathrm{e}^{-\mathrm{R}_1(1+\mathrm{k}_{\mathrm{E}1})\mathrm{t}}}\left(\ {}_1\left(1-\frac{1-e^{-R_2(1+k_{E2})t}}{1+k_{E1}e^{-R_2(1+k_{E2})t}}\right)+\ {}_2\left(\frac{1-e^{-R_2(1+k_{E2})t}}{1+k_{E2}e^{-R_2(1+k_{E2})t}}\right)\right)-\mathrm{Z}_{(\mathrm{t})\mathrm{expt}}\right)^2} \tag{3.46}$$

$$F\left(\mathrm{k}_{\mathrm{R}1}, \mathrm{k}_{\mathrm{R}2}, \mathrm{k}_{\mathrm{I}1}, \mathrm{k}_{\mathrm{I}2}, \varphi_1\ , \varphi_2\right) = \sum \sqrt{\left(\frac{\mathrm{k}_{\mathrm{R}1}-\mathrm{k}_{\mathrm{R}1}\mathrm{e}^{-\left(\mathrm{k}_{\mathrm{R}1}+\mathrm{k}_{\mathrm{I}1}\right)\mathrm{t}}}{\mathrm{k}_{\mathrm{R}1}+\mathrm{k}_{\mathrm{I}1}\mathrm{e}^{-\left(\mathrm{k}_{\mathrm{R}1}+\mathrm{k}_{\mathrm{I}1}\right)\mathrm{t}}}\left(\ {}_1\left(1-\frac{\mathrm{k}_{\mathrm{R}2}-\mathrm{k}_{\mathrm{R}2}\mathrm{e}^{-\left(\mathrm{k}_{\mathrm{R}2}+\mathrm{k}_{\mathrm{I}2}\right)\mathrm{t}}}{\mathrm{k}_{\mathrm{R}2}+\mathrm{k}_{\mathrm{I}2}\mathrm{e}^{-\left(\mathrm{k}_{\mathrm{R}2}+\mathrm{k}_{\mathrm{I}2}\right)\mathrm{t}}}\right)+\ {}_2\left(\frac{\mathrm{k}_{\mathrm{R}2}-\mathrm{k}_{\mathrm{R}2}\mathrm{e}^{-\left(\mathrm{k}_{\mathrm{R}2}+\mathrm{k}_{\mathrm{I}2}\right)\mathrm{t}}}{\mathrm{k}_{\mathrm{R}2}+\mathrm{k}_{\mathrm{I}2}\mathrm{e}^{-\left(\mathrm{k}_{\mathrm{R}2}+\mathrm{k}_{\mathrm{I}2}\right)\mathrm{t}}}\right)\right)-\mathrm{Z}_{(\mathrm{t})\mathrm{expt}}\right)^2} \tag{3.47}$$

3.4 Summary

The extant adsorption models and their limitations when applied to monolayer construction have been discussed. Two main limitations have been highlighted, in that extant models cannot account for sequential processes or the affects of preadsorbed species on the surface on the adsorption process. Two new models the PTCS and PIF models have been developed to address these limitations.

Chapter 4 Preliminary Biolayer Study

4.1 Introduction

The method of tethering antibody (IgG) macromolecules to the surface of a transducer has the ability to influence the shelf-life, reproducibility and sensitivity of an electrochemical immunosensor. Hence, it is one of the most important aspects of electrochemical immunosensor manufacture. There are a number of methods by which IgG can be attached to the surface of a transducer, the cheapest of which is direct attachment where the antibody attaches directly to the inert metal transducer via nitrogen atom electron lone pairs, present on antibody amino acid side chains (Diaz-Gonzalez et al, 2005). However, this method was found to yield immunosensors with low sensitivity, reproducibility and shelf-life when compared to other immunosensors utilising alternative antibody tethering techniques (Diaz-Gonzalez et al, 2005).

The number of methods available to produce an electrochemical immunosensor is therefore vast and a detailed study of all of them is impractical. Therefore it was decided to confine the scope of this study to examine two processes one the direct attachment of a IgG to the metal substrate and a second process representing the most promising method currently available.

This chapter deals with the selection of the second process, investigates if a viable sensor can be made by said process and if so can the chosen analytical techniques produce the desired measurements for each stage of the sensor manufacture.

4.2 Method selection

Two main methods have been developed to tether IgG molecules to the surface of a transducer. One involves the use of polymer films to tether IgG to the surface of a transducer and the other involves the use of modified thioalkane-based self assembled monolayers (SAMs).

4.2.1 Polymer films

Polymer films are normally attached directly to the metal transducer. The reason for employing such films is that molecules in the film are strongly bound together so the

ability of the polymerised film to desorb is limited by the size of the film, which has many interactions with the metal surface (Cosiner, 2005).

The first use of polymer films in biosensors was reported by Foulds et al. (1986) and Umana et al. (1986), who described the entrapment of enzymes within a conducting polypyrrole film (Cosiner, 2005). Since then, a wide variety of studies have been carried out using polymer films in biosensors. A large number of these are included in a review by Cosiner (2005).

Recent examples featuring IgG tethered to a planar surface using Electropolymerized films have been reported by Barton et al (2009) and Das et al (2009). In the first study, Poly(1,2,diaminobenzene) was sonicated to form micropores before the IgG was attached to the film. The second IgG tethering method used a microporous silicone layer, which was formed by anodizing silicone in hydrofluoric acid and N,N-dimethylformamide.

Whilst there have been many successful studies conducted into the production of immunosensors using polymer films, the preparation of many of these films involve the use of either highly poisonous, carcinogenic or volatile chemicals at high temperature (Das et al, 2009, Gondran et al, 2010). This necessitates the use of stringent safety precautions which can inhibit sensor manufacturing efficiency and increase the overall cost of sensor production. Moreover, the production of some monomers for polypyyrole films (the most popular type of polymer film) are time consuming. Das et al, 2009 and Gondran et al, 2010 reported preparation time in excess of twelve days. With these reasons in mind it was decided that this study would not proceed with the analysis of any of these processes.

4.2.2. Self Assembled Monolayers (SAMs)

The alternative to polymeric films to attach IgG to the surface of the transducer is to use SAMs. This root seems to offer a safer and more viable route to a working sensor and has been chosen for further consideration. However if this process is to be used then the following choices needed to be to be made:

1) Type of SAM
2) Method of attachment of IgG to The SAM Monolayer

4.2.2.1 Type of SAM

The type of SAM to be used to tether the IgG required careful consideration because interactions between the individual SAM molecules and with the supporting substrate will determine the ability of the molecules to stick to the surface. Interactions between different SAM molecules vary in strength depending on the functional group present on the SAM and the molecule‘s alkyl chain length (Schreiber, 2000) and can affect the quality and stability of the layer formed .

Many authors have chosen to use mercaptocarboxylic acid SAMs with long alkyl chains (Wang et al, 2008, Kim et al, 2005, Liu et al, 2008). The strong hydrogen bonding and Van Der Waals interactions between the SAM molecules in the monolayer cause each molecule to be tethered to the surface via the adjacent molecules as well as via each molecule‘s Au-S interaction. The monolayer can therefore be considered to act as a film with many interactions existing between the film and the metal surface. These include Van Der Waals interactions and Au-S interactions, each of which serves to inhibit SAM molecule desorption from the surface. However the use of long alkyl chain mercaptocarboxylic acids can lead to nonspecific hydrophobic adsorption of contaminants (Cosiner, 2005). This can inhibit the adsorption of subsequent molecules, thereby affecting biolayer stability. Gauche defects are also apparent in SAMs formed from long alkyl chains (Schreiber, 2000) that will affect adsorption of subsequent layers to the SAM layer and can result in loss of biosensor sensitivity.

To overcome these problems, recent reports (Kaur et al, 2008, Mitchell, 2006; Liu, 2006) have featured immunosensors based on short chain mercaptocarboxylic acid SAMs. Even though the use of smaller molecules in the monolayer results in a reduced number of Van Der Waals interactions between SAM molecules, it is thought that these interactions are minimal in comparison to the magnitude of the intermolecular hydrogen bonds (Henderson et al, 2009) and the stability of the manufactured layer is not impaired. Therefore it was decided to use this type of SAM layer and Mercaptopropionic acid (MPA) was chosen as the SAM for further study

4.2.2.2 Method of attachment of IgG to the SAM Monolayer

Direct attachment of the IgG to the surface is the simplest and least expensive way of attaching IgG and a number of immunosensors have been reported that are constructed in this manner (Tili et al, 2006, Barreiros Dos Santos et al, 2009, Hnaien et al, 2008, Buchatip et al, 2010, Kyprianou, 2010, Zhang et al, 2009). In such instances, it is normal for the carboxyl groups to be activated using an activation agent that enables the carboxyl groups to bind covalently to amino groups on the IgG molecules. This reaction can occur at any amino group on the IgG molecule, including the amino groups on the Fab fragments. Binding to the Fab fragments in this manner increases steric hindrance during the IgG – analyte immobilisation stage, compromising sensor sensitivity (Dos Santos et al, 2009). Sensor sensitivity is further reduced because the IgG molecules are fixed to the surface by many covalent bonds between carboxyl groups on the modified metal surface and the IgG molecules. During the target molecule immobilisation stage, this restricts the movement of the Fab fragments from the surface, reducing the chance of collisions occurring between the target molecules and the IgG molecules.

The modified surface binding to the Fab fragments can be limited by first covalently binding a protein A layer or protein G layer to the SAM modified surface before immobilising IgG. As protein A and G have an affinity toward Fc fragment binding, all IgG Fab fragments are orientated toward the surface maximising the number of potential target analyte binding sites and maximising sensor sensitivity (Hao et al, 2009, Choi et al, 2008, Ribaut et al, 2008, Briand et al, 2006).

Alternatively other studies have reported the attachment of IgG to a metal transducer surface using various Streptavidin/Avidin-Biotin based tethering methods (Ding et al, 2005, Cui et al, 2003, Hays et al, 2006, Hafaid et al, 2009). The most common method involves first modifying the SAM with Streptavidin or Avidin then attaching the IgG as a biotinylated IgG to the modified surface. As Streptavidin and Avidin are proteins consisting of amino groups, these macromolecules will readily covalently bind to activated carboxyl groups on a SAM modified metal transducer surface. After the Avidin or Streptavidin layer has bound to the surface, the remaining activated SAM carboxyl groups are deactivated to prevent non-specific binding by adding small molecules consisting of amino groups to the surface. These molecules are unlikely to affect subsequent molecular binding to the Avidin or Streptavidin, but covalently bind to the exposed, activated carboxyl groups of the SAM layer. IgG labelled with Biotin (Biotinylated IgG, b-IgG) is then added to the Avidin or Streptavidin modified surface.

The Streptavidin or Avidin based immunosensors tend to be more stable than the protein A or protein G based sensors because IgG molecules bound to protein A or protein G do not have as greater degree of freedom as IgG molecules tethered to the surface using the high affinity interactions that exist between Streptavidin or Avidin and Biotin. Moreover, protein A or protein G monolayers bind to the IgG Fc fragments with less affinity than Streptavidin or Avidin monolayers bind to biotinylated IgG again reducing stability. For this reason it was decided to use Streptavidin to attach the IgG to the SAM in this study

4.3 Experimental work

Once the preferred method of assembly of the sensor had been decided upon a series of scouting experiments were carried out to determine if the sensor could be assembled and if the preferred measurement technique of EIS could measure the surface coverage achieved during most stages of manufacture.

To minimize costs at this stage the process was simplified by using Avidin in place of Streptavidin as a substitute molecule. Avidin itself is unsuitable as the active layer on the proposed sensor because it promotes the hydrolysis of the covalent bond linking

Biotin to a Biotinylated macromolecule (Huberman, 2001) inhibiting tethering Biotinylated-IgG to the modified surface of an impedance-based immunosensor. However, as the preliminary study was to test the formation of the Streptavidin layer and no Biotinylated macromolecules were involved, its use was appropriate.

4.3.1 Chemicals and solutions

Mercaptopropionic acid (MPA) was purchased from Sigma and used without purification at a dilution of 0.0529 M in ethanol. The electrochemical cell solution consisted of 0.1 M phosphate buffer solution (PBS, pH = 7.4), which contained 0.1 M KCl as supporting electrolyte and 0.05 M $K_3Fe(CN)_6$ as redox mediator. All DI water used over the course of this experiment was 15 MΩ, unless stated otherwise. The relative concentrations of EDC (Fluka) and NHS (Sigma) in 0.1 M PBS solution (pH=7.4) were 0.5 mg/ml and 5mg/ml respectively. Avidin and biotin, were obtained from Sigma.

4.3.2 Cleaning

All glassware was rinsed with aqua regia (25% v\v HNO_3, 75% v\v HCl) followed by a concentrated NaOH solution rinse and then a DI water rinse to remove sources of organic and ionic contamination. The working electrode was cleaned in accordance to the manufacturer‘s instructions, i.e. they were polished using 0.05 μm alumina powder, followed by ultrasonic cleaning for 10 min in DI water, before being ultrasonicated in piranha solution (75% v/v H_2SO_4, 25% v/v H_2O_2) to remove organic contaminants.

To ensure effective electrode cleaning, 5 cyclic voltammogram sweeps were performed between a potential of -0.5V and 0.5V at a current of 0.1mA. Overlapping scans inferred that non-atomically bound matter was no longer transferring into the bulk PBS solution from the electrode, thus the working electrode was assumed to be clean at this point.

4.3.3 Electrochemical measurements

The tests were performed using a conventional three electrode system with an Autolab potentiostat/galvanostat in conjunction with Frequency Response Analyser (FRA) and General Purpose Electrochemical System (GPES) software (Eco Chemie B.V.), for

EIS and Cyclic Voltammetry (CV) measurements respectively. The Ag/AgCl reference electrode, platinum wire counter electrode and gold working electrode (MF-2014) were all purchased from BASi instruments Inc and all electrochemical measurements were performed in PBS buffer solution.

To ensure that each of the electrodes in the cell remained at an equal distance from each other over the course of the experiment, an electrode holder was manufactured (Figure 4.1).

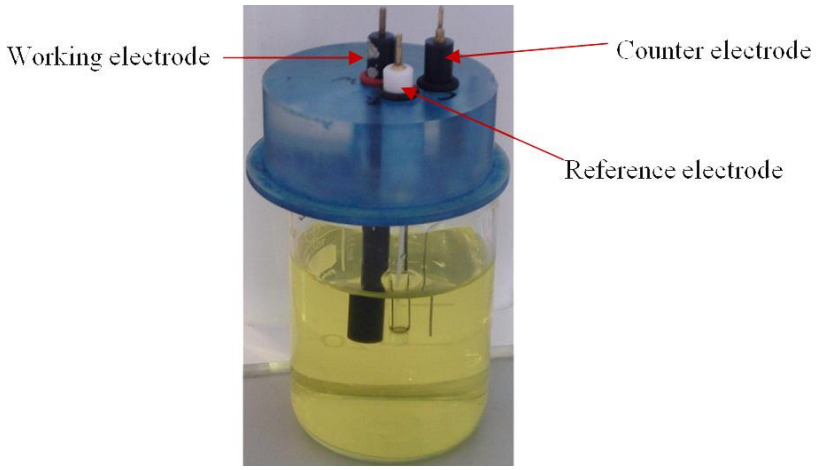

Figure 4.1: Showing an electrode holder (blue) that was 20 mm thick to preserve a constant distance between the reference, counter and working electrodes whilst they are immersed in electrochemical solution (yellow).

For EIS, a 0.1 mV amplitude sine wave was applied to the working electrode in the tested frequency range of 0.1 Hz to 1 MHz. The working electrode was polarized at a potential of +0.25 V/Ag(AgCl) during measurements, which was shown via CV to be the oxidation potential of the redox indicator. EIS measurements were performed after the working electrode had been cleaned, after it had been immersed EDC/NHS solution, after Avidin immersion and after it had been immersed in Biotin.

4.3.4 SAM growth procedure

The working electrode was rinsed in ethanol after the initial measurement, to avoid MPA solution contamination with PBS, before being immersed in MPA solution at room temperature (21 ^{o}C) for 12 hrs. The working electrode was subsequently ultrasonicated for 2 min 30 s in ethanol, to remove non-chemisorbed MPA molecules.

4.3.5 EDC/NHS activation procedure

Following the SAM growth procedure, the modified working electrode was thoroughly rinsed in DI water before and after EIS measurements. It was then immersed in EDC/NHS solution at room temperature (21^{o}C) for 2h. The modified working electrode was then rinsed in PBS to remove NHS and EDC molecules which were not covalently bound to the surface prior to EIS measurements.

4.3.6 Streptavidin growth procedure

Following the SAM activation procedure and EIS measurement, the working electrode was thoroughly rinsed in DI water and immersed in Streptavidin solution at room temperature (21^{o}C) for 2 h. The modified working electrode was removed from the Streptavidin solution before being thoroughly rinsed to remove Streptavidin molecules which were not covalently bound to the surface prior to EIS measurements.

4.3.7 Biotin immobilisation procedure

The working electrode was rinsed in DI water before being immersed in Biotin solution for 2 hrs. Upon being removed from the Biotin solution the electrode was rinsed to remove loosely bound Biotin.

4.4 Results

The impedance measurements recorded for the tests performed for each stage of biosensor construction are recorded as a Nyquist plot in Figure 4.2 and have been published (See Pruneanu et al, 2008).

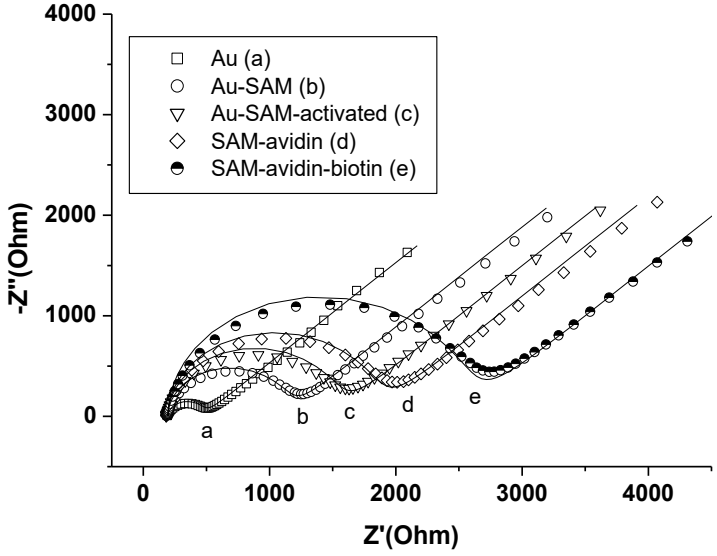

Figure 4.2:. Nyquist plots from the report by Pruneanu et al (2008), of gold (a) and gold modified electrode: Au-SAM (b); Au-SAM-activated (c); SAM-avidin (d); SAM-avidin-Biotin (e).

Each of the plots in Figure 4.2 consists of two parts, a semicircular part at high frequency and a linear part at low frequency. The semicircular part is dictated by solution resistance, ohmic resistance, charge transfer resistance and the capacitance of the electrochemical cell, which is dictated mostly by the dielectric properties of the double layer and the modified biolayer. Hence, non-ideal capacitor behaviour is observed. Mass transfer in this instance is negligible as the charge on the counter and working electrode changes too rapidly to cause significant diffusion.

At low frequencies electrodes hold a particular charge for a long period and mass transfer of redox ions to and from the electrodes becomes a significant factor. This causes the measured electrochemical cell impedance profile to differ from that of a non-ideal capacitor and the complex impedance profiles exhibit a straight line relationship.

The lowest frequency measurements exhibit the highest –Z‘‘ and Z‘ values. They also appear at the point at which the largest difference between monolayer impedances exists. Impedance values at this point clearly vary depending on the fractional coverage of the substrate with a certain monolayer. Hence, a frequency of 0.1 Hz will be used to measure and mathematically model the relationship between impedance arising from monolayer adsorption and immersion time.

All of the complex impedance plots originate from the same impedance, where Z‘ is 195 and –Z‘‘ is 0. This reflects that Ohmic resistance remained constant and that solution resistance encountered between the counter electrode and working electrode remained constant as a result of the electrodes being held at a constant distance from each other by the electrode holder.

Taken as a whole for each layer modification to the surface the impedance profile is observed to change systematically. This confirms that the impedance measurements can be used to measure the change in surface coverage as each layer is formed.

4.4.1 The impedance behaviour of the MPA layer

The shapes of the other impedance plots clearly demonstrate that a Streptavidin-Biotin layer was successfully tethered to the surface of the gold working electrode transducer using activated MPA (Figure 4.2). The adsorption of MPA (SAM) to the electrode caused electron transfer to occur via electron tunnelling as opposed to direct charge transfer over the double layer. This mechanism of charge transfer requires the existence of a larger potential drop over the SAM on the gold layer than over the double layer, causing an increase in the charge transfer resistance over the monolayer. The addition of SAM molecules over the surface of the electrode also acts to alter the electrochemical cell‘s capacitance as the impermeable SAM layer possesses dielectric properties which act to absorb electric field energy more effectively than the surrounding solution.

4.4.2 The impedance behaviour of activated MPA layer

During activation, SAM is converted into an intermediate product to facilitate the immobilisation of Avidin. In this study the intermediate product is N-succinimidyl 3-mercaptopropionate. This causes a thickening of the modified layer and a larger potential drop to be experienced over the activated MPA layer, resulting in a wider semicircular plot in Figure 4.2, indicating a higher charge transfer resistance.

4.4.3 The impedance behaviour of the Avidin layer

Avidin is a significantly larger, non-conductive, organic molecule than NHS-ester and can be seen to reduce the charge transfer current to the electrode surface, thereby increasing the charge transfer resistance. This resulted in a slightly wider complex impedance profile. This is the subject of further discussion in Chapter 8.

4.4.4 The impedance behaviour of the Biotin layer

A very large difference in impedance profile can be seen between the Avidin profile and the Biotin profile in Figure 4.2. The vitamin d-Biotin is very small when compared to the Avidin macromolecule and is expected to account for an insignificant amount of biolayer thickness. The large impedance increase observed between the traces can be directly attributed to the decrease in porosity of the layer brought about by the strong bonding of the biotin to the Avidin. This places a significant restriction on redox ion mass transfer, causing a significant reduction in charge transfer current and an increase in charge transfer resistance.

4.5 Summary

A biotin layer was successfully bound to a gold electrode surface using a multilayer consisting of an Avidin monolayer and an MPA monolayer activated with EDC-NHS. This layer was constructed by immobilising MPA on the gold surface, activating the MPA with EDC and NHS to create an NHS-ester intermediate monolayer, immobilising an Avidin monolayer on the modified gold surface and, finally, immobilising a biotin monolayer on the surface.

EIS was used to assess layer coverage and results were presented as a Nyquist (complex impedance) plot after each monolayer was adsorbed to the surface. The impedance profiles showed systematic changes as monolayers were adsorbed to the

surface. These changes indicated that impedance is dependent on fractional coverage and confirmed that impedance was a viable measurement to assess surface coverage for all processes under consideration. In each case the greatest difference in impedance profile was observed to be at a frequency of 0.1 Hz therefore this frequency was adopted for all quantitative measurements.

Chapter 5:- Preparation of the gold electrode surface

5.1 Introduction

Preparation of the gold substrate used to support the sensor is very important to the construction of a successful sensor. It is very important to ensure that a flat surface is produced free of contaminants and defects. This should ensure that the sensor has low background currents in addition to rapid electron transfer rates that are desirable for this type of application (Creager et al,1992, Yang et al, 1995, Hoogvliet et al, 2000), Ding et al, 2007) .

In addition it is necessary when carrying out sequential electrochemical measurements of the type proposed for this study, to develop a cleaning strategy that produces consistently flat clean surfaces every time. The same electrodes will be used for all studies and it is essential that the electrodes can be cleaned to remove the monolayer and repolished to give a consistent finish.

A number of methods have been employed to facilitate the maintenance and cleaning of working electrodes (Ding et al, 2007; Hoogvliet et. al, 2000; Yang et. al, 1995; Creager, 1992; Landolt, 1987; Angerstein-Kozlowska, 1986; Oesch, 1983). These are often referred to as polishing techniques and can be grouped as either being electrochemical based: which involve eroding the surface by passing a DC current through an electrolyte to remove metal ions from the electrode surface; or mechanical based, which involves physical abrasion of the surface.

Mechanical polishing can lead to an uneven surface geometry in the form of scratches. This is undesirable as it can give rise to non-uniformities in SAM and protein crystal formation and also affect the means by which the redox active species transfers to the electrode, thereby potentially impacting on biosensor sensitivity (Pravda et al, 2001, Schrieber, 2000).

The surface defects produced by mechanical polishing can be reduced through electropolishing. Electropolishing effectively produces a good surface finish on a metal electrode by making it anodic in an appropriate solution (Ding et al, 2007; Landolt, 1987; Angerstein-Kozlowska, 1986; Oesch, 1983). However if the sample is treated for too long A double layer, may form over the electrode surface which will impede the formation of the subsequent monolayers. Therefore if electropolishing is to be attempted an understanding of the process is required.

This chapter critically evaluates the quality of the surfaces produced through mechanical polishing electrochemical polishing and chemical cleaning and tries to suggest the optimal conditions for producing a clean flat surface appropriate for monolayer growth.

5.2 Cleaning methods

A number of cleaning methods can be employed to remove surface contamination from an electrode prior to coating with a monolayer. The main two groups are mechanical polishing and electrochemical polishing. However, mechanical polishing can be supplemented with electropolishing and both can be supplemented with chemical cleaning and ultrasonication.

5.2.1 Mechanical polishing

Mechanical polishing covers grinding, polishing and buffing, which encompass all processes required for improving the surface conditions of a product for decorative or functional purposes. The three methods are used sequentially where grinding is the most aggressive technique but rapidly removes material from the surface. The purpose of polishing is to improve the surface finish from the grinding step, so that it is smoother but not mirror-like and uses abrasives firmly attached to a flexible backing, such as a wheel, belt or orbital motion tool. Thus, the mechanical polishing abrading operation removes or smoothes grinding lines, scratches, pits, mould marks, parting lines, tool marks, stretcher strains, and surface defects. The process causes some plastic working of the surface as metal is removed. Unfortunately, a mechanically polished surface has also been found to yield scratches, strains and embedded abrasives, although these are not as significant as those resulting from grinding. Buffing generates extremely fine surfaces which are typically smooth,

highly reflective and mirror-like. Buffing uses abrasives or abrasive compounds that adhere loosely to a flexible backing, such as a cloth wheel, and slowly abrade the surface material to eliminate the embedded abrasives, scratches and metal debris resulting from prior polishing stages. However, it must also be noted that this method has also been found to leave microscopic scratches.

5.2.2 Electropolishing

Electrochemical polishing is referred to as electropolishing, where a two electrode configuration is employed. The anode consists of the electrode or substance to be polished and the cathode is an electrode that usually consists of an inert metal to minimize cathode erosion. The circuit is completed by a suitable electrolyte. In this process, the electrodes are immersed in a corrosive electrolyte, causing a thin stagnant film of electrolyte to form across the working electrode (known as the "anode film") and a potential difference is applied across the electrodes. The potential applied across the working electrode causes the electrode to become positively charged and a large potential drop is experienced between the anode and the negatively charged ions in solution. Thus, when a sufficient potential is applied to the working electrode, the ionic forces of attraction between the negatively charged species in solution and a positively charged ion on the anode is sufficient to break the intermolecular bonds between adjacent metal ions and the positively charged metal ion is absorbed by the electrolyte.

The anode film is critical to the electropolishing process and can give rise to features having different erosion rates. This film has been found to possess excellent dielectric properties, is usually assumed to have a nominal thickness, forms across the low lying features of the anode and decreases in density with increased distance along the normal to the electrode surface. Thus, charge density across the anode is unevenly distributed, with features protruding above the film having the highest positive charge density and low lying features having the lowest density. As a result, peaks which protrude above the film are eroded quickly, medium sized peaks on the surface are eroded at a slower rate and low lying features are eroded at the slowest rate (see Figure 5.1).

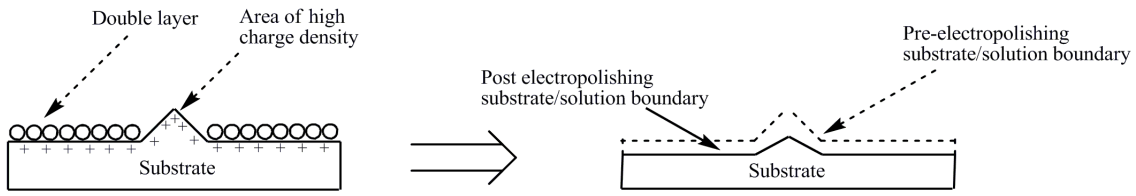

Figure 5.1: Demonstrating erosion rates in electropolishing: the low charge density and protective double layer slow the rate of erosion of low lying features; protruding features are afforded little double layer protection and have a high charge density resulting in a fast rate of erosion.

Rates of electropolishing are controlled by the applied electrical potential (Jones, 2004). These potentials can vary greatly in the literature and are dependent on a number of factors including the type of electrolyte used, the metal being polished and other physical parameters, such as temperature and degree of agitation (Jones, 2004). In spite of the fact that it is often required to employ different potentials to polish different metals with different electrolytes and in different conditions, they all display a similar anodic polarisation curve (See Figure 5.2) that comprises of four distinct regions which are commensurate with the type of surface finish achieved (Delayen et. al. 2001).

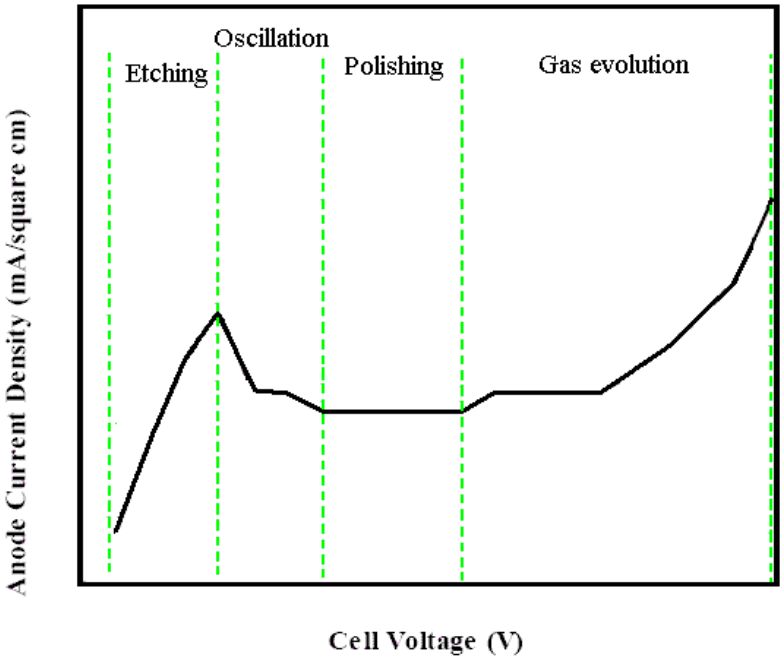

Figure 5.2: A typical Anodic current/ Cell voltage profile, showing physical effects occurring at the electrode interface over given potentials.

5.2.2.1 Etching

In this region, current density increases proportionally with cell potential difference. Delayen et. al (2001) found that metal surfaces in the etching region appear to be rough and suggested that this roughness was due to the enhanced etching near grain boundaries (as charge density is highest in these areas).

5.2.2.2 Oscillation

In the ―Oscillation," region the electrodes current density periodically oscillates and is very temperature dependant (Delayen et. al, 2001). In this instance, the mechanism for material removal from the surface of the electrode goes from being largely etching-based at lower potentials to polishing-based at higher potentials.

5.2.2.3 Polishing

In the polishing region, very smooth surfaces with no observable grain boundaries are seen under the optical microscope. However, surfaces obtained here are less shiny than the surfaces of samples polished in the oscillation region. It was also found that at ―polishing" potentials, a thick electrolyte layer becomes visible over time (Alqaradawi, 2003, Palmieri and Rampazzo, 2007). This could account for the reduction in shininess of the polished metal surfaces in the polishing region.

5.2.2.4 Gas Evolution

Finally, in the gas evolution region, the electrolyte layer disappears and pitting occurs in the electrode surface (Alqaradawi, 2003, Delayen et. al., 2001). Typically, the size of the pits increases with the increasing voltage and is due to the generation of gas at the anode surface causing erosion.

5.2.3 Extant surface cleaning strategies

It is clear from the preceding section that electro polishing could be used to produce a highly polished surface on its own. Indeed electropolishing of metals is an established stand alone technique and is commonly used as a means of producing highly polished gold surfaces in the metal finishing industries. The metal finishing industry therefore has a number of established processes that could be adopted for polishing of electrodes intended for biosensor use.

The metal finishing industry has optimized a number of key factors in there process to produce highly polished surfaces. One of the more important is the choice of electrolyte and a number of standard electrolytes have been used successfully. These include: Sulfuric acid, potassium cyanide and thiourea solutions with sulfuric acid (Jones, 2004). A second key factor is the choice of applied voltage which in many cases is in the range of between 6 V and 12 V (Jones, 2004, Savitskii and Prince, 1989) which promotes the rapid erosion of the raised areas of the surfaces allowing the gold to be effectively polished over a period ranging from 30 s to 5 min.

However, in metal finishing, the processes are solely focused on obtaining a good metal finish and are not concerned with preserving the electrochemical properties of the gold electrode. When trying to produce an electrode suitable for monolayer growth and analysis of said layer by impedance spectroscopy things are more complicated and the electrolytic properties must be considered in conjunction with the surface finish. Multistep procedures and different parameters will be required to produce gold electrodes suitable for biosensor manufacture.

The need to produce an optimized procedure to clean and polish the surface whilst maintaining the electrolytic properties is obvious and two studies have been carried out to investigate the cleaning of electrodes specifically coated with MPA.

In the first Carvalhal et. al. (2004) investigated different mechanical, electrochemical polishing and cleaning regimes to obtain an optimum electrochemical signal for gold electrodes which had been modified with MPA prior to cleaning. This study employed three different cleaning techniques:

1) A mechanical polish consisting of a 0.5um polish followed by a 0.3um polish (performed using alumina slurry)

2) Immersion in a piranha solution to chemically clean the surface

3) An electrochemical polish involved performing 25 cyclic voltammetry sweeps between a potential of +0.1V to +1.2V (vs SCE) in a three electrode

configuration with the gold electrode as the working electrode and a platinum counter electrode in a 0.5M H_2SO_4 electrolyte solution.

and various combinations of the preceding three steps. Ultrasonication followed each cleaning step and the cleaning effectiveness was quantified by measuring the reproducibility and efficiency of MPA removal from gold via cyclic voltammetry (CV).

This study revealed that a combination of sequential cleaning using mechanical cleaning, chemical cleaning and electropolishing, applied to the modified gold surface respectively, yielded the best results. Electropolishing alone failed to provide significant electrode cleaning and the use of mechanical cleaning alone (as recommended by the Bioanalytical Systems Inc, BASi, electrode care manual (Bioanalytical systems Inc., 2001) was the least effective method.

The second study was performed by Ding et. al. (2007) who removed the piranha chemical cleaning step and replaced it with ultrasonication steps, consisting of ultrasonication in a water bath and then in an ethanol bath. This removed the bulk of organic contaminants before the electropolishing step. It was thought that the final electropolishing stage effectively removed all remaining organic matter as well as residual ethanol, as aggressive acids were employed during this stage.

Three solutions were employed for electropolishing including: 1 M perchloric acid ($HClO_4$), 1 M sulfuric acid (H_2SO_4) and 50mM 2-(N-Morpholino) ethanesulfonic acid (MES). The electropolishing potential range employed in this study was 0 to +1.5 V at a sweep rate of 500 mV s^{-1} over 30 cycles. It is interesting to note that the voltage applied has been reduced from the 6 -12 volts common in metal polishing to 0 to +1.5 V. The reduced voltage is seen as an attempt to minimize double layer formation which is known to impede adsorption of monolayers (Ding et al, 2007). Cleaning effectiveness in this instance was quantified by measuring a cyclic voltammogram produced by a three electrode configuration in a solution of 2-(*N*-morpholino)ethanesulfonic acid buffer (MES) and potassium ferrocyanide $\{K_3Fe(CN)_6\}$.

The study revealed that the perchloric acid was the most efficient solution and that the sulfuric acid was the least effective. This is thought to be a result of the respective acid conjugate bases provided a weak force of attraction to the gold surface in the case of the perchloric acid and a strong force of attraction in the case of the sulfuric acid.

Perchloric acid clearly provides a good electrolyte for electropolishing purposes, however, this chemical presents a severe explosion risk, particularly when combined with organic compounds such as acetic acid, methanol and ethanol (Sciencelab.com, Inc, 2005). The preceding ultrasonication step involves ethanol as the process solvent and transfer over of the ethanol between stages could give rise to an explosive mixture. The conventional way of avoiding explosions is to work at sub-zero temperatures but this introduces additional complications to the process. Therefore in the interests of safety it is perhaps better to accept the weaker performance of the sulfuric acid and to make this the preferred electrolyte.

The two studies reported so far (Carvalhal et. al, 2004, S.J. Ding et. al, 2007) have addressed the best cleaning methods for gold surfaces and attempted to maintain surface properties by adapting the conditions and materials used to minimise effects detrimental to the electrodes electrical properties. However no in-depth, quantitative assessment of the resulting surface properties was made and new experimental data is required to address this deficiency.

5.3 Experimental work

This experimental programme studied, the resulting surface properties of gold electrodes after they have been cleaned using a sequential cleaning procedure. EIS, cyclic voltammetry and optical microscopy were used to analyse the changes in the electrode surface properties and double layer thickness as a result of each stage of the cleaning process. The results yielded from the analysis of each cleaning process provided a quantitative insight into the degree of contaminant removal after each process was completed.

5.3.1 The sequential cleaning process

After a number of initial trials and with reference to the previous studies a 3 stage sequential cleaning process was arrived at that seemed to give the best compromise for safely producing a clean surface with the best electrochemical properties.

5.3.1.1 Mechanical cleaning

The electrode was polished sequentially, using three polishing wheels employing particulates of 1 μm, 6 μm and 300 μm. The 1 μm universal polisher (Metaserve) revolved at a speed of 300 rpm, the 6 μm wheel was mounted on a DP-20 polisher (Struers) and the 300 μm wheel was mounted on a Knuth Rotor (Struers). Both the Struers polishers rotated at a speed of 250 rpm. Electrodes were polished until no more non-uniformities were evident and the best surface finish was obtained at each step, which was determined using the optical microscope.

The electrode was then polished using 0.05 μm alumina slurry on a polishing pad by moving the electrode surface over the pad in a figure of eight motion until minimal scratching was observed via the optical microscope. Abrasive particulates entrained in the surface were removed via ultrasonication in purified water for 10 min.

5.3.1.2 Chemical cleaning with Piranha Solution

After mechanical cleaning, the electrode was ultrasonicated in piranha solution (75% v/v sulfuric acid, 25% v/v hydrogen peroxide) for 40 min, at 40^{o}C. Unlike the conventional method of cleaning, which relied on ultrasonicating electrodes in water prior to piranha solution immersion, this method aids organic matter removal by using ultrasonication in the piranha solution immersion step as well.

5.3.1.3 Electropolishing

The electropolishing stage was carried out using 1M sulfuric acid in purified water by performing 90 sweeps between a potential of 0V and 1.5V at a scan rate of 0.5V/s. The electropolishing procedure was performed using an Autolab potentiostat/galvanostat (Eco Chemie B.V.) in conjunction with General Purpose Electrochemical Software, GPES, in a two electrode configuration with a platinum wire counter electrode (BASi).

5.3.2 Measurements

5.3.2.1 Optical measurements

Initial surface analysis was carried out using a Versamet-2 microscope (Union) at x5 optical zoom with a ET USB 2750 camera (eMPIA technology) and Scope photo software (Scopetek).

The working electrode was inspected after each mechanical polishing step. Prior to inspection the electrode was rinsed with water and then with ethanol to remove any loose surface debris from the cleaning process. A further examination was made at the end of the mechanical cleaning process after the sample had been ultrasonicated in piranha solution. A similar procedure was adopted for the electropolishing step where inspection was carried out after every 30 voltage sweeps. Sample photos were taken at each inspection point to provide a permanent record of the observations

5.3.2.2 Cyclic Voltammetry Measurements

Cyclic Voltammetry measurements were made on the electropolishing stages only. Both working electrodes were rinsed in purified water prior to Cyclic Voltammetry measurements. To conduct Cyclic Voltammetry measurements, an Autolab potentiostat/galvanostat (Eco Chemie B.V.) was used in conjunction with General Purpose Electrochemical Software, GPES (Eco Chemie B.V.). A three electrode configuration was employed with a platinum wire counter electrode and Ag/AgCl reference electrode. All electrodes, including the gold working electrode (MF-2014) were purchased from BASi instruments Inc.

Measurements were taken after the electropolished working electrode had been cleaned over: 0, 30, 60 and 90 sweeps. Cyclic Voltammogram measurements were also obtained for the working electrode that had been cleaned in piranha solution after it had been ultrasonicated over a period of 40 min.

Measurements were conducted in 0.1M PBS buffer (pH = 7.3) with 0.1M KCl electrolyte concentration and 0.05 M concentration of redox indicator [$K_3Fe(CN)_6$, Fisher Scientific]. 3 CV sweeps were performed between a potential of -0.5V and 0.5V at a scan rate of 0.01 V/s.

5.3.2.3 Electrochemical Impedance Spectroscopy Measurements

Prior to EIS, all electrodes were rinsed with purified water. Each measurement was performed using a conventional three electrode system with an Autolab potentiostat/galvanostat (Eco Chemie B.V.) in conjunction with Frequency Response Analyser (FRA). The Ag/AgCl reference electrode, platinum wire counter electrode and gold working electrode (MF-2014) were all purchased from BASi instruments Inc and all electrochemical measurements were performed in PBS.

Measurements were taken after the electropolished working electrode had been cleaned over: 0, 30, 60 and 90 sweeps. EIS measurements were also obtained for a working electrode that had been cleaned in piranha solution after it had been ultrasonicated over periods of 0 min, 15 min, 30 min, 45 min and 60 min. To minimise the effect of piranha solution degradation, fresh piranha solution was used after each EIS measurement.

For EIS, a 0.1 mV amplitude sine wave was applied to the working electrode in the tested frequency range of 0.1 Hz to 1 MHz, except in the case of piranha cleaning tests where the range tested was 10 Hz to 1 MHz. The working electrode was polarized at a potential of +0.25 V/Ag(AgCl) during measurements, which was shown via CV to be the oxidation potential of the redox indicator. EIS measurements were performed after the working electrode had been cleaned and after it had been immersed in MPA solution.

5.4 Results

5.4.1 Results of mechanical cleaning process

There are two primary aims of mechanical cleaning, which include:

1. The removal of the double layer formed over the surface during measurement, which becomes significant if a multitude of measurements are undertaken without mechanical cleaning. Significant double layer formation affects measurement reproducibility and chemical properties of the working electrode.
2. The removal of deep scratches from the surface of the working electrode. Charge density will gather around the corners of these scratches, also acting to make the gold surface less uniform and rougher. If this roughness is of a scale

larger than the diffusion layer thickness, mass transfer of redox ions to the gold surface, during EIS and CV measurement, can be adversely affected serving to reduce the reproducibility of electrochemical measurements.

More specifically, scratches causing a roughness which is of a scale larger than the diffusion layer thickness, distorts concentration contours sufficiently across all laminae in the boundary layer to result in a change in redox ion mass transfer vector, see Figure 5.3C. This contributes to an increase in the electrode surface area available for electron transfer and a higher charge transfer current than that of a smooth surface electrode (Bard and Faulkner, 2001).

Ideally, the surface of the electrode should be atomically flat, which gives rise to the diffusion profile in Figure 5.3 A. However, small microscratches (which constitute a smooth surface) have been found to alter the concentration contours in the diffusion layer close to the electrode surface. This distortion in the concentration contour lines becomes less evident as the distance along the surface normal increases (see Figure 5.3B) until the diffusion layer/bulk solution boundary is reached. As the diffusion contours have not been significantly altered in the boundary layer, mass transfer vector of redox ions through the boundary layer to a smooth electrode surface is the same as that of an ideal case. Hence, the redox ion mass transfer vectors are thought to be predominantly ideallic after mechanical polishing, even though the abrasive particles used to mechanically polish the electrode introduce microscratches during the polishing process. Entrained abrasive particulates are commonly removed via ultrasonication in water after the mechanical polishing process is complete.

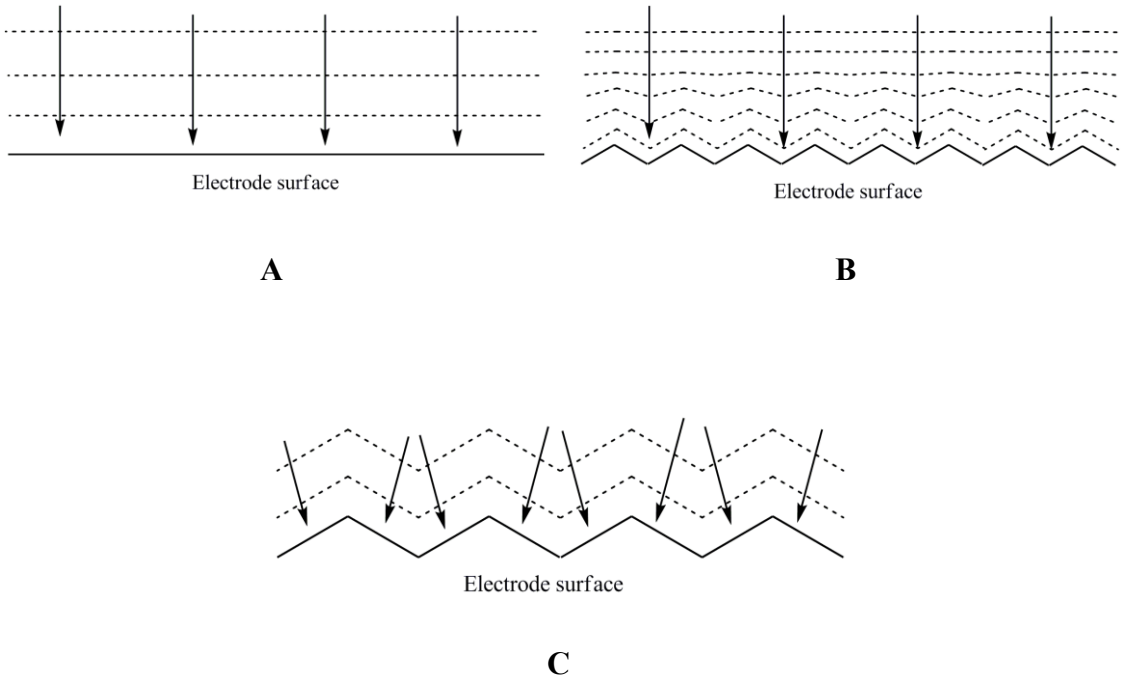

Figure 5.3: Showing redox ion diffusion vectors (arrows), electrode solution boundaries (solid line) and lines of equal concentration (dashed lines)

5.4.2 Cleaning using piranha solution

The next stage of the process is to chemically clean the electrode in Piranha solution. This serves two purposes:

1) The surface will be contaminated with organic contaminants, introduced during the mechanical polishing stages; most of these will be removed on ultrasonication in piranha solution.

2) If the gold electrodes are left after mechanical cleaning because gold is naturally hydrophilic, it is common for a hydrophobic organic film to form over the surface of a cleaned gold electrode impairing its electrical properties this will be removed by the piranha solution.

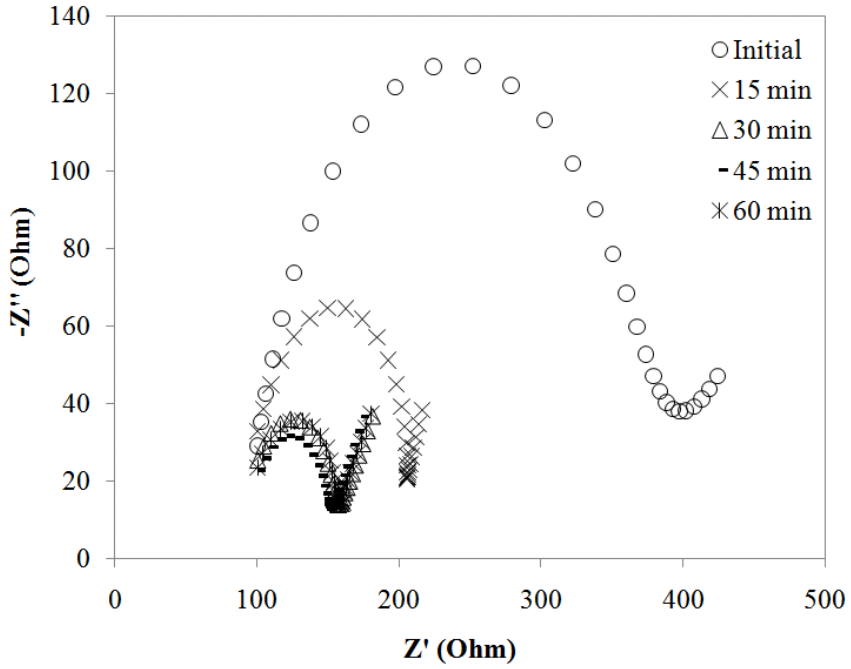

Figure 5.4: Shows the evolution of a cleaned working electrode surface as a function of piranha solution immersion time in an ultrasonic bath. Measurements were taken after the post mechanical polishing purified water ultrasonication step (initial) and after 15 minute intervals of piranha solution ultrasonication, up to an overall immersion time of 60 min.

The high impedance -Z" values of the initial dataset shows that there is an insulating dielectric layer of organic contamination present across the surface of electrode (Figure 5.4). This layer is known to restrict the mass transfer of redox ions to and from the working electrode surface when it is immersed in electrochemical solution. The presence of non-conductive material on the surface contributes to imaginary impedance and the restriction the layer provides to the mass transfer of redox ions serves to increase charge transfer resistance.

Figure 5.4 also shows data for the real and imaginary impedance for samples ultrasonicated in piranha solution for increasing periods (15 minute increments) of time. The 15 minute sample shows a significant amount of the organic, dielectric layer is removed from the surface, which is reflected in the decrease in impedance values. The piranha solution accomplishes this in two stages:

1) Initially the hydrogen and oxygen atoms in the organic layer are removed via a hydration reaction with concentrated sulfuric acid. This reaction is relatively fast (Barber, 2006).

2) The next stage is much slower. It involves the removal of residual carbon from the electrode surface, where concentrated sulfuric acid dehydrates hydrogen peroxide to form hydronium ions, bisulfate ions, and transiently, atomic oxygen. The extremely unstable atomic oxygen then reacts with the residual carbon on the surface of the electrode, rendering it soluble, and allows the removal of the organic layer remnants.

The first stage process is hampered by a competing reaction where the hydrogen peroxide decomposes into water and oxygen, which not only serves to deplete the hydrogen peroxide used in carbon removal, but also acts to dilute the concentration of the sulfuric acid used in both stages of organic contaminant layer removal. The water evolved from this side reaction coupled with the water that evolves as a product of piranha cleaning, acts to further dilute and reduce the cleaning effect of piranha solution, as a function of reaction time. As a result, fresh piranha solution must be prepared for each cleaning procedure (Barber, 2006).

As immersion time increases, the consumption of the organic layer during piranha cleaning limits the piranha rate of reaction. After a piranha solution immersion time of 30 min, the impedance values do not change significantly and therefore it may be concluded that changes in the amount of contamination on the surface due to the cleaning reaction are very small and cannot be accurately measured using EIS spectra. Thus, 40 min was assumed to be the optimum piranha cleaning period.

5.4.3 Cleaning using electropolishing

The impedance measurements indicate that the ultrasonication in piranha solution is successful at removing debris and organic contaminants from the surface however a problem was found to exist with several electrodes that were contaminated with an unknown substance. This contaminant was found not to be significantly affected via mechanical polishing or the subsequent piranha cleaning, showing that the contaminant was both hard and inorganic. The contaminant layer, can be seen clearly in the microscope image of Figure 5.6 (A), where the dark patches represent the insulating, dielectric layer. The dielectric layer remained present on the surface in spite of mechanical polishing (see Figure 5.6 (C)).

EIS spectra obtained from this contaminated electrode, are shown in Figure 5.5. The very high impedance values, indicate that a significant dielectric layer has been formed.

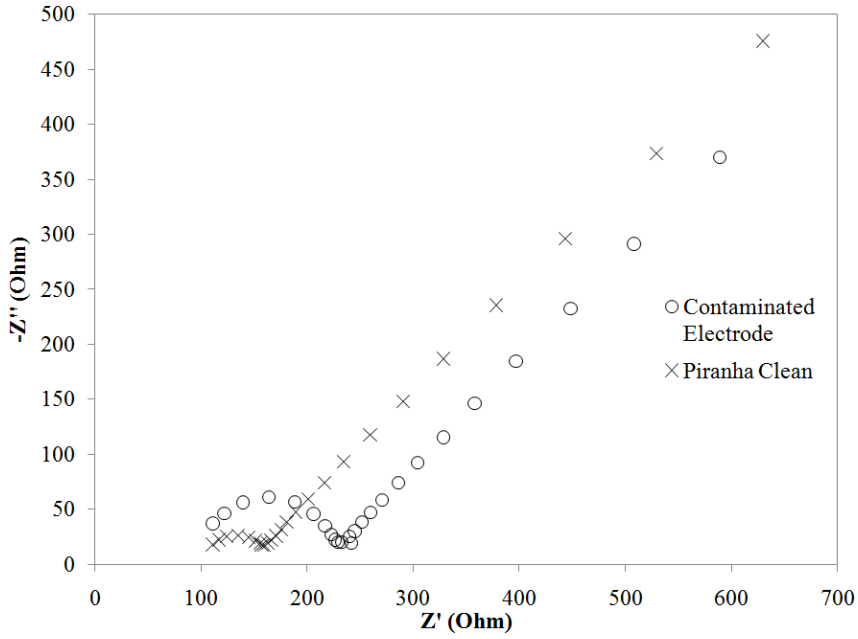

Figure 5.5, where: "piranha clean" corresponds to a typical Nyquist plot yielded from an electrode that has undergone piranha cleaning. "Contaminated electrode" corresponds to the post piranha clean EIS for the electrode which was tarnished.

Figure 5.5 shows the improvements made to the measured impedance following electropolishing. Electropolishing removes the outermost layer of Au electrode molecules that the contaminant has bound to, thereby removing the contaminant. Figure 5.6 (D) supports this argument as it demonstrates that electropolishing has reduced sample discoloration (which is indicative of contamination on the sample surface).

The electropolishing seems to have increased the cleanliness of the surface beyond that normally achievable for the piranha clean alone where the insoluble contaminant is not present. This is indicated by the impedance plots in Figure 5.7 where the impedance values have reduced. This is not surprising as the electropolishing will strip off a complete monolayer of gold from the electrode surface removing any remaining organic contaminants with it.

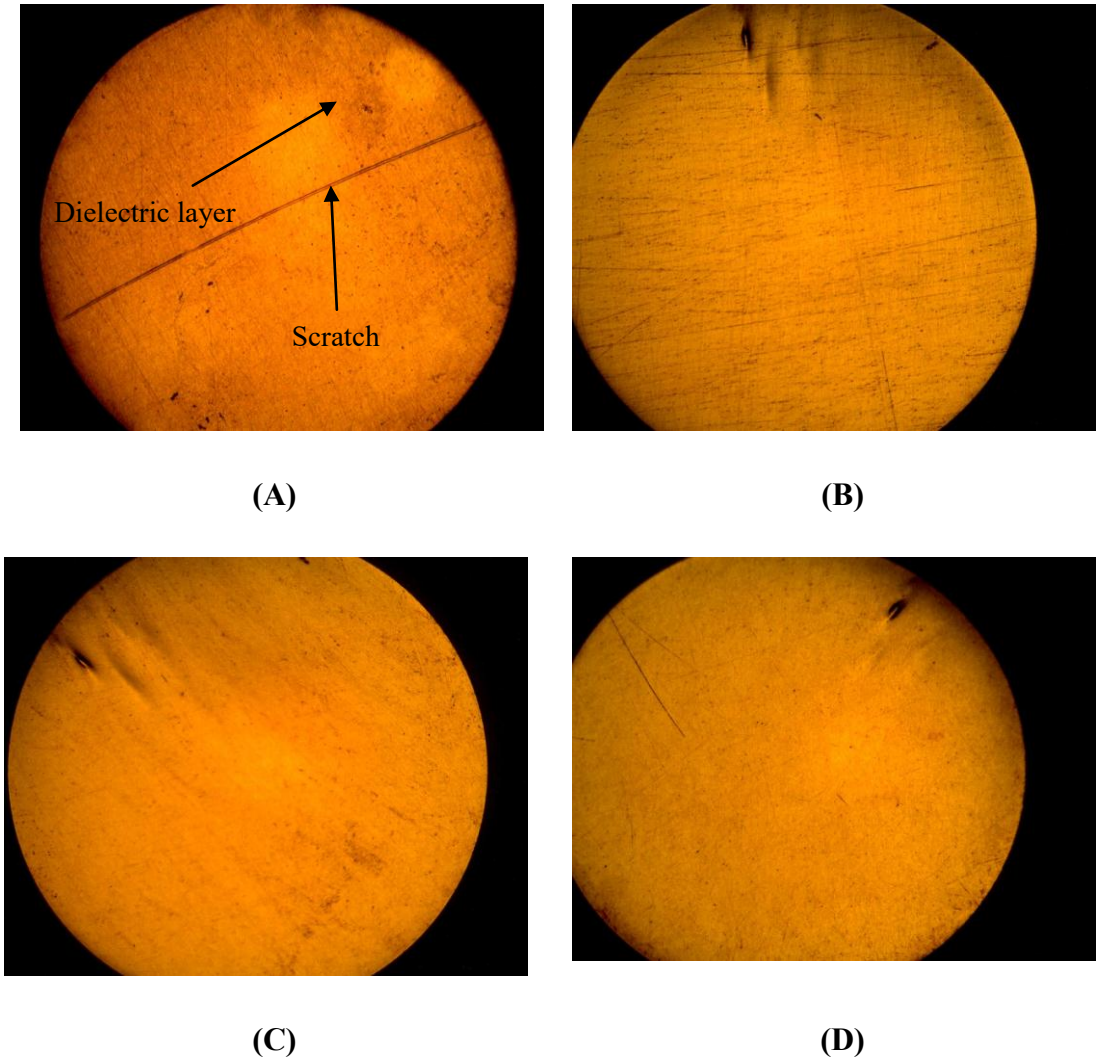

Figure 5.6: Optical microscope images of the contaminated electrode (A), after polishing using 30 µm, 6 µm and 1µm (B), after 0.05µm alumina slurry polish (C) and after 30 electropolishing sweeps (D).

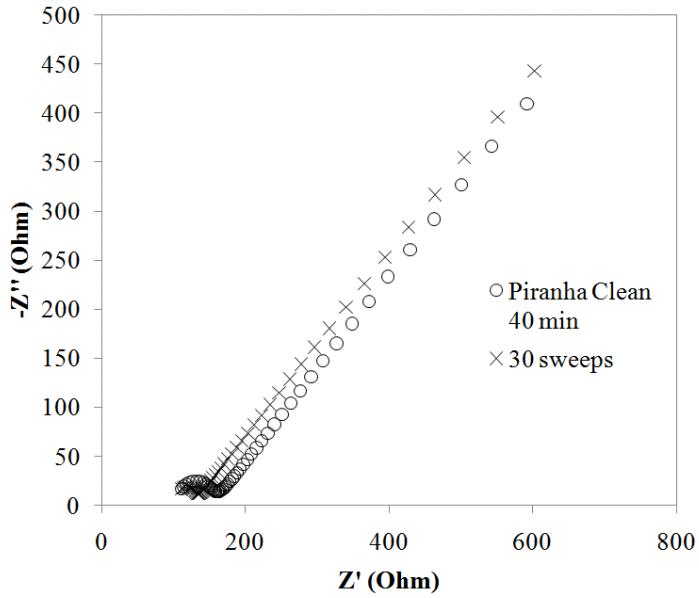

Figure 5.7: A typical piranha cleaning EIS spectra (piranha clean 40min) and the EIS spectra obtained from the electropolished electrode after 30 sweeps (30 sweeps), which had been previously contaminated with the unknown dielectric substance.

5.4.3.1 Electropolishing sweep optimisation

As demonstrated above the electropolishing cleaning stage is very good at removing contaminants from the surface of the electrode left behind by the preceding cleaning operations. However, microscratches resulting from mechanical polishing cause uneven charge distribution across the surface of the substrate during electropolishing and can change the surface topography of the working electrode. This is undesirable and it is necessary to optimise the number of electropolishing sweeps so that the working electrode surface is clean and so that scratches aren‘t widened to an extent where they affect redox ion mass transfer vector.

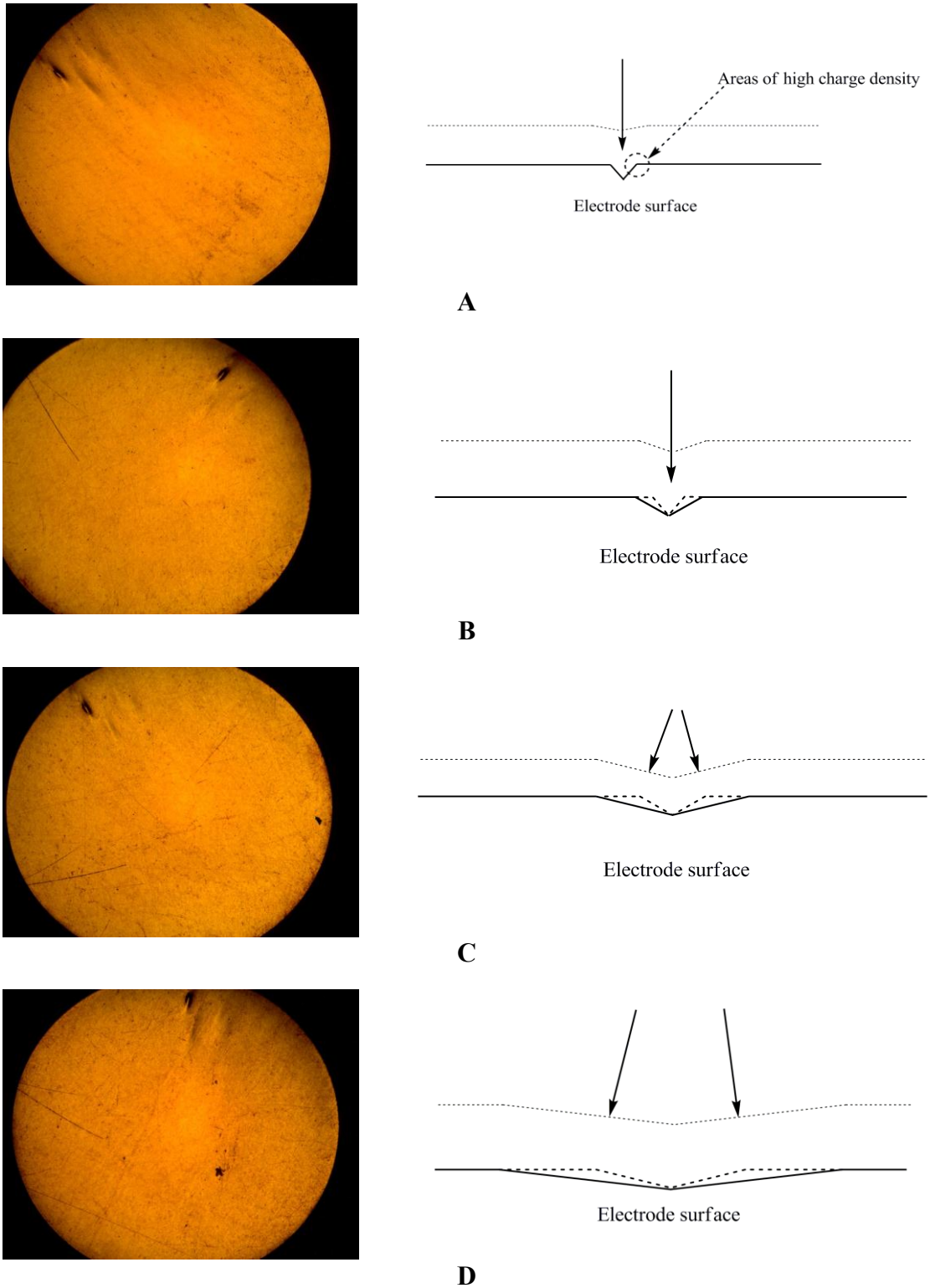

Figure 5.8: Photographs of a polished electrode after: Alumina polishing (A), 30 electropolishing sweeps (B), 60 electropolishing sweeps (C) and 90 electropolishing sweeps (D); accompanied with diagrams showing where scratches have been corroded (solid lines illustrate electrode/solution boundaries and dashed lines illustrate former electrode/solution boundaries) and how redox ion mass transfer was affected during electrochemical measurements (dotted lines join points of equal concentration and arrows indicate redox ion diffusion vectors).

The effect of increased number of electropolishing sweeps on redox ion mass transfer vector is shown in Figure 5.8. After a smooth, mirror like finish had been obtained on the electrode surface using 0.05 μm alumina slurry mechanical polishing, small microscratches present on the surface were not sufficient to shift the redox ion mass transfer vectors from ideality (see Figure 5.8A). Over the course of 30 electropolishing sweeps, areas of high charge density built up around the corners of small microscratches resulting in a fast rate of corrosion in these areas. This served to widen the scratches and cause them to become visible via optical microscope (See Figure 5.8B). Although over a period of 30 sweeps, this was found to have an insignificant effect on redox ion mass transfer.

After 60 sweeps had been undertaken, more scratches have been sufficiently widened to become evident on the optical microscope image. Moreover, scratches that were initially evident are sufficiently wide enough to have an effect on redox ion mass transfer vector. This is shown in Figure 5.9 by a shift in the measured oxidation potential between the CV measured after 30 sweeps and after 60 sweeps. Similarly, a shift in impedance can also be noticed in Figure 5.10, between the EIS spectra obtained after 30 sweeps and 60 sweeps. This shift was caused by a large double layer forming across the electrode‘s increased surface area (brought about as a result of scratch widening). As more double layer molecules are available to contribute to imaginary impedance after 60 sweeps, a larger semicircle is observed in the Nyquist plot in Figure 5.10.

After 90 sweeps, erosion caused by electropolishing eliminates scratches and are replaced by a slight unevenness in the electrode surface (Figure 5.8 D). This causes redox ion mass transfer vectors to almost return to ideality, resulting in a shift in oxidation potential to the value observed for 30 sweeps (Figure 5.9) and a decrease in EIS spectra semicircle size from the ~~“6~~0 sweeps” dataset to the ~~“9~~0 sweeps” dataset (Figure 5.10). It can be seen that the semicircle is smaller for the ~~“3~~0 sweeps dataset” than for the ~~“9~~0 sweeps” dataset, indicating that the double layer is thicker after 90 sweeps than after 30 sweeps.

Other scratches that were not apparent after 30 and 60 sweeps become apparent after 90 sweeps (see Figure 5.8). These scratches were initially very narrow and deep after mechanical polishing and took a large number of electropolishing sweeps to undergo scratch widening. In instances such as this, some of the redox ion mass transfer vectors deviate from ideality, although this effect appears to be negligible for the ~~"~~90 sweeps" dataset in this investigation (see Figure 5.9 and Figure 5.10).

Upon comparing the electropolished electrode surface yielded by 90 sweeps to the other intervals that were tested, it can be seen that scratching on the surface after 30 sweeps affects redox ion mass transfer the least and the double layer is also smallest after 30 sweeps. Hence, it can be concluded from this investigation that 30 sweeps is the optimal number of electropolishing sweeps to be used in the preparation of gold electrodes for electrochemical biosensor construction.

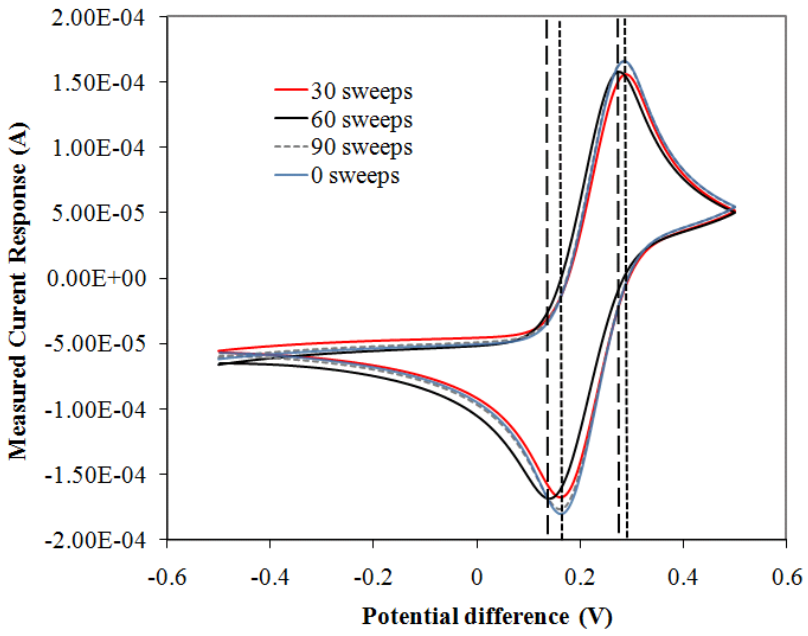

Figure 5.9: Cyclic Voltammogram showing the shift in redox potential peak as a result of scratch widening during electropolishing. The dashed and dotted lines represent the potentials at which the redox potential occurs after 60 sweeps and after 30 and 90 sweeps respectively

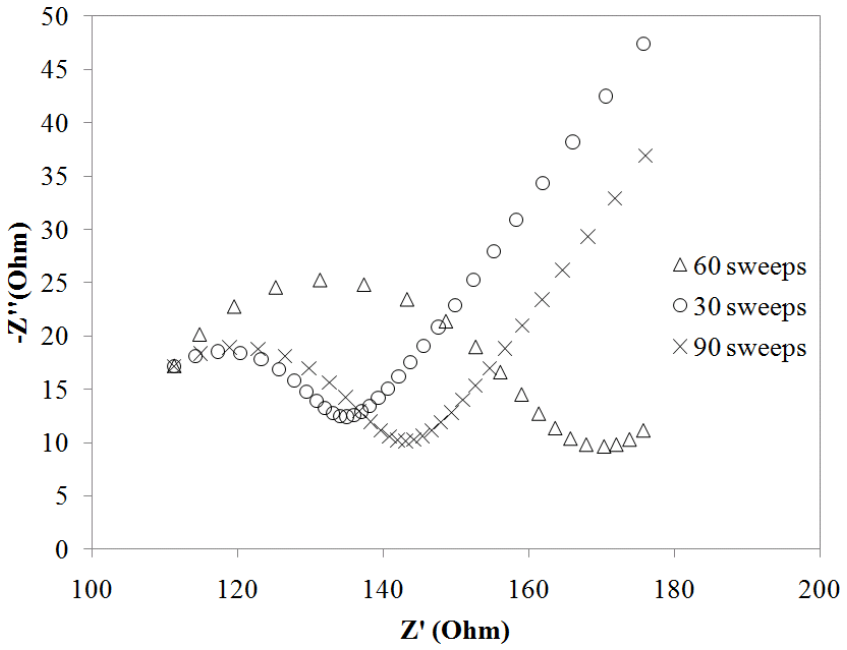

Figure 5.10: Nyquist plot showing complex impedance profiles brought about by the widening of microscratches and the build up of a double layer on the electrode surface as a result of electropolishing sweeps.

5.5 Summary

The effects of electropolishing on electrode surface properties and double layer thickness were studied and compared to conventional cleaning methods using EIS, cyclic voltammetry and optical microscopy. Changes in resistance and capacitance over the electrode surface allowed the recognition of scratches, double layer and contamination when used in conjunction with optical imaging. The traditional method of cleaning using Piranha solution was revealed to be effective at removing organic contamination from the surface of the electrode. However, in the rare occasions where inorganic contaminants are present, piranha solution was found to be an unsuitable cleaning technique.

Cleaning via electropolishing was found to be the most thorough cleaning method and was demonstrated to be effective on all types of contamination encountered within a period of 30 sweeps. Upon performing additional electropolishing sweeps, double layer thickness increased and previously insignificant microscratches widened and disrupted the electrode‘s redox ion diffusion field.

Therefore, to avoid the detrimental side effects of electropolishing, it is the finding of this investigation that the optimum working electrode pre-treatment ordinarily

involves mechanical polishing followed by ultrasonication in purified water for 10 min and subsequently ultrasonication in piranha solution for 40 min. However, mechanical polishing followed by ultrasonication in purified water for 10 min and subsequently electropolishing should be employed to remove contamination when inorganic contaminants are present on the surface. In this instance, electropolishing is undertaken in 1M sulphuric acid and over the period of 30 sweeps, where each sweep occurs between potentials of 0 V and 1.5V and occurs at a rate of 0.5V/s.

Chapter 6: Optimisation of formation of Mercaptocarboxylic Acid Monolayers on Au(111) substrates

6.1 Introduction

The first stage in producing a layer constructed biosensor with optimum performance would involve coating the gold substrate with a modified thioalkane-based self assembled monolayer (SAM). Mercaptocarboxylic acid monolayers are often the SAM of choice for use with Au(111) substrates (Luppa et al, 2001). An explanation for this is that Au films are relatively easy to prepare, the substrate relatively easy to clean, and the short hydrocarbon chain SAMs are simple molecules that exhibit all the properties and degrees of freedom necessary for complete monolayer formation. Mercaptocarboxylic acid SAMS also result in fewer intermolecular interactions than its intermediate and long chain counterparts that act to reduce gauche defects and ultimately resulted in a more ordered monolayer (Schreiber, 2000; Porter et. al, 1987; Alves et. al, 1992; Kang and Rowntree, 1996).

The structure and growth of the monolayer on an Au(111) substrate is dictated by a number of factors including: substrate structural defects, temperature during monolayer formation, immobilization technique, solvent used, electrode pretreatment, chain length, monolayer density and headgroup structure (Chen and Li, 2006; Schreiber, 2000; Gyepi-Garbrah and Šilerová, 2001). This study will focus on the key factors by optimising the temperature and immersion times of the substrate in the MPA solution.

6.1.1 Formation of MPA layers: Himmelhaus model

Intrinsic to the process of optimization of the layer formation is an understanding of how the layer is formed. Current knowledge on the formation of MPA monolayers indicates that the process is complex. Previous studies of the formation of the MPA layer using SFG (sum frequency generation) show that the detection signal approximates the Langmuir adsorption isotherm model for the first few minutes of SAM solution immersion, but at longer immersion times, systematic deviations from the Langmuir isotherm are reported (Peterlinz et. al, 1997; Bain et al, 1989; Xu et al, 1998). Himmelhaus et. al. (2000) conducted an in-depth investigation into this behaviour using SFG and was able to break down the mechanism into three distinct stages of monolayer formation.

6.1.1.1 The first stage of MPA layer formation.

Himmelhaus et al (2000) first stage of layer formation consisted of the chemisorption of the thiol headgroup on to the substrate with the molecules lying flat and parallel to the plane of the substrate. Camillone et al (1996) established that this stage happens very rapidly, in the order of seconds or minutes. Further they observed that the alkanethiol hydrocarbon chains in this state were ordered as shown in Figure 6.1. Some of the sulfur groups were spaced at a distance of 31.7 $\mathring{A}$, approximately twice the length of the decanethiol SAM molecule immobilized (L), other sulfur groups were spaced at 2.2 $\mathring{A}$, the length of a disulphide bond indicating a degree of dimerization had occurred. This hypothesis was supported by two studies of alkanethiols on Au surfaces via XSW (X-ray Standing Wave) data (Fenter et al, 1998; Fenter et al, 1999).

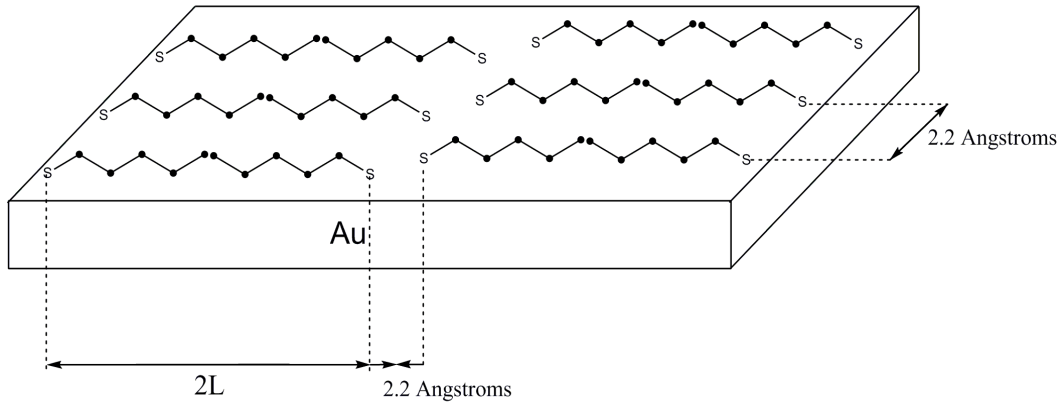

Figure 6.1: Diagrammatic representation of a low coverage alkanethiol molecular arrangement on an Au(111) surface.

6.1.1.2 The second stage of MPA layer formation.

Himmelhaus et al (2000) second stage of layer formation corresponds to re-orientation of hydrocarbon chains to an angle of 30^{o} perpendicular to the substrate surface and occurs over a much longer immersion period. The hydrocarbon chain re-orientation is brought about by interactions between adjacent SAM molecules on the substrate (Camillone et al, 1996; Poirier, 1999; Dubois et al, 1993, Gerlach et al, 1997).

Moreover, the tilt angle of alkanethiols varies between 0^o and approximately 60^o to the substrate as a function of SAM density on the Au surface (Chidsey et al, 1989; Strong and Whitesides, 1998; Chidsey and Loiacono, 1990). The re-orientation of hydrocarbon chains causes the structure of the SAM monolayer on the Au surface to change progressively from a low coverage phase to a transitional structural phase and, finally, to the saturated phase structure.

6.1.1.3 Third stage of MPA layer formation: Saturated phase.

Himmelhaus et al. (2000) third stage was shown to occur over the longest period of immersion time and involved the ordering of the SAM terminal functional groups. The reported structure of the saturated phase of an alkanethiol SAM on an Au(111) surface can be seen in Figure 6.2 and has been described as having the hexagonal notation: $(\sqrt{3} \times \sqrt{3}) R30^o$ (Chidsey et al, 1989; Strong and Whitesides, 1998; Chidsey and Loiacono, 1990). Each sulfur group that has been chemisorbed onto the Au substrate is spaced at 5 $\mathring{A}$ from adjacent sulfur groups and molecular interactions between adjacent hydrocarbon chains give rise to a 30^o hydrocarbon chain tilt angle from the normal (Nuzzo et. al, 1990a; Nuzzo et. al, 1990b) (see Figure 6.2).

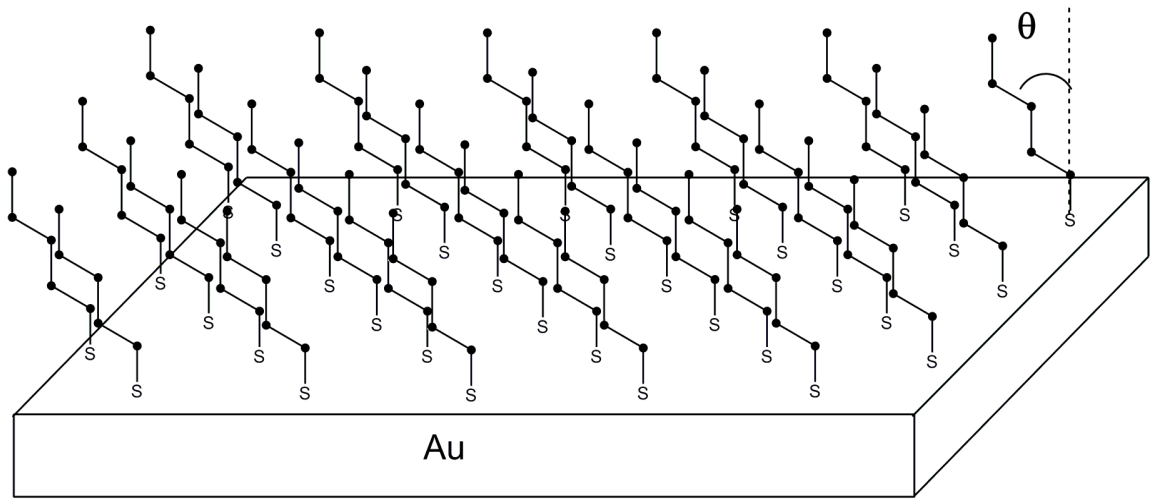

Figure 6.2:. A diagrammatic representation of a saturated monolayer structure on a Au(111) substrate, with chemisorbed sulphur groups (S) and hydrocarbon chains (solid lines) at a tilt angle of θ^{o} from the normal (dotted line).

6.1.2 Exceptions to the Himmelhaus Models

Exceptions exist to the mechanism for SAM formation proposed by Himmelhaus et al (2000). Some instances have been reported where saturated alkanethiol layers have differed in structure to the conventional ($\sqrt{3}$ x $\sqrt{3}$) R30^{o} structure (Pockels, 1891; Fenter et al, 1994; Als-Nielsen et al, 1991). It was suggested by Schrieber (2000) that a possible reason was that sulfur group interactions played a more dominant role in SAM molecule positioning in very short hydrocarbon chain alkanethiols than in larger hydrocarbon chain alkanethiols.

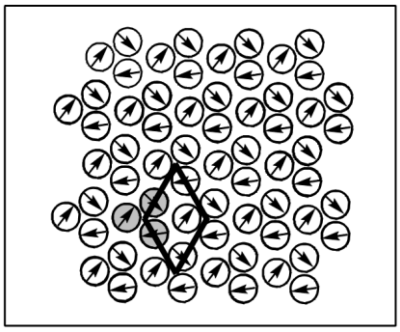

Figure 6.3:. A diagrammatic representation of the structure of a mercaptopropionic acid monolayer. MPA molecules are shown as circles, with an MPA structure highlighted in grey; substrate molecules are shown in white and the black rhombus shows the inter-structural spacing.

6.1.2.1 Carboxyl terminated thioalkanes.

In a more recent study, the structure of 3-mercaptopropionic acid (HS-$(CH_2)_2$-COOH) on a Au(111) surface was studied (Sawaguchi et al, 2001). This short chain thioalkane exhibited an ordered monolayer with disordering only occurring near etched areas of the substrate. The structure of the short chain mercaptoalkane carboxylic acid was found to exhibit a different structure to that of the conventional ($\sqrt{3}$ x $\sqrt{3}$) R30 ^{o} structure, as a result of the strong intermolecular hydrogen bonds brought about by the SAM molecule COOH terminal group (Nuzzo et al, 1990a), see Figure 6.3. In this instance, triangular structures, each consisting of 3 adjacent SAM molecules, are arranged in a rhombus shape, with the centre of each triangle at a distance of 1 nm between adjacent structures. Each individual SAM molecule on the surface of the Au(111) monolayer is spaced at a distance of 4.53 $\mathring{A}$ within a triangle.

6.2 Current models for the SAM formation mechanism

The Langmuir adsorption isotherm, (see Chapter 3.2), is conventionally used to model most instances of molecular adsorption and has been found to provide an adequate approximation to SAM first stage growth (Dannenberger et al, 1999). In this instance, growth rate is proportional to the number of available binding sites on the Au surface, where Θ is the fraction of the Au surface covered, R is the rate constant and t is immobilization time. This model, however, fails to take into account molecular interactions, which have a significant effect on the rate of formation and the geometry of the monolayer. This encompasses electrostatic interactions of adjacent molecules, in addition to the effects of immobilized SAM molecules and immobilized SAM molecule orientations on aqueous SAM molecule diffusion from the bulk solution to the Au(111) surface.

In an attempt to overcome this problem, a modified Kisliuk model (as discussed in Chapter 3.2) was introduced to take into account the interactions of the increasing number of SAM molecules present on the Au surface during the period of monolayer formation. This was accomplished through the use of ~~"s~~ticking coefficients (k_E)" which vary depending on: hydrocarbon chain length; functional groups that may be present on the SAM's constituent molecules; SAM molecule solution concentration, and experimental conditions that can influence monolayer growth (examples of these

include: the type of solvent used, immobilization temperature and the degree of solution contamination) (Dannenberger et al, 1999; Kreuzer, 1995).

Although the Kisliuk and Langmuir adsorption isotherms both give an effective approximation to substrate coverage with SAM as a function of immersion time, neither isotherm models second and third stage growth. This is critical as, in many instances, functional group orientation affects the monolayer properties as well as the rate and reproducibility of subsequent reactions involving the immobilized SAM layer. Thus, there is a need to develop a model which is capable of predicting SAM growth and degree of ordering as a function of immersion time. The next stage in developing said model is to produce an experimental study that will give more information about what effects the different mechanisms of second and third stage growth have on the physical properties of the monolayer and how temperatures affect the relative rates of the processes. The experimental study also provides the data benchmark against which any proposed models can be evaluated.

6.3 Experimental work

A series of two independent sets of measurements were carried out. The principle measurements were made using Electrochemical Impedance Spectroscopy (EIS). This method was selected because it is particularly suited to the analysis of the bulk changes in the interfacial properties of modified electrodes upon monolayer formation occurring at the modified electrode surface. This is due to the ability of EIS to provide detailed information on capacitance and resistance changes occurring at the electrode surface, as well as the kinetics and mechanisms of electron transfer processes.

A second set of measurements were made using Infrared Reflection Adsorption Spectroscopy (IRRAS) at 20 ˚C to verify the EIS measurements. IRRAS was chosen because it shows some advantages over conventional IR spectroscopy. For instance, it can be used for samples that are not transparent over an appreciable wavelength range in the IR region. In IRRAS the IR beam is reflected from the front face of a highly reflective sample. Using this method typical spectra produce outputs such as transmittance versus wavelength and absorbance versus wavelength or wavenumbers. The data in this research is represented as absorbance versus wavenumber.

6.3.1 Chemicals and solutions.

MPA (Sigma) at a concentration of 0.05 M was used in ethanol (Fisher Scientific). 0.1 M phosphate buffer solution (PBS, pH = 7.4) was prepared, which contained 0.1 M KCl (BDH) as supporting electrolyte and 0.05 M $K_3Fe(CN)_6$ (Fisher Scientific) as redox mediator. Deionised water (DI) (15 MΩ) was used, unless otherwise stated.

6.3.2 Cleaning.

The EIS SAMs were prepared on a set of three gold working electrodes. The working electrodes were polished using 0.05 μm alumina powder, followed by ultrasonic cleaning for 10 minutes in DI water. The working electrodes were then ultrasonicated in piranha solution before being rinsed in DI water and subsequently in ethanol, to remove inorganic and organic contaminants from the electrodes prior to MPA immobilization.

To ensure effective electrode cleaning, 5 cyclic voltammogram sweeps were performed between a potential of -0.5 V and 0.5 V. Overlapping scans inferred that non-atomically bound matter was no longer transferring into the bulk PBS solution from the electrode, thus the working electrode was assumed to be clean.

The IRRAS studies were performed on borosilicate glass slides coated with Au(111) . The glass slides were cleaned by immersion in piranha solution, 75 % v/v H_2SO_4 (Fluka) and 25 % v/v H_2O_2 (Fisher Scientific), before being rinsed firstly in DI water and then subsequently in ethanol, to remove inorganic and organic contaminants from the slides prior to MPA immobilization.

All glassware was sequentially rinsed with aqua regia, 25 % v/v HNO_3 (Fisher Scientific) and 75 % v/v HCl (Fisher Scientific), concentrated NaOH (Fluka) solution and DI water to remove sources of organic and ionic contamination.

6.3.3 SAM growth procedure.

Working electrodes and Au coated glass slides were rinsed in ethanol after the initial measurements, prior to immersion in the MPA solution to avoid MPA solution contamination with PBS

The gold coated glass slides and electrodes were then immersed in MPA solution held at the desired temperature. Temperature control of the samples was maintained either in refrigerator for low temperature measurements or in a water bath. Several working electrodes were initially immersed in each MPA solution and each electrode/glass slide was sequentially removed for measurement after a certain immersion period.

Upon removal from the MPA solution, electrodes were immediately ultrasonicated for 2 min 30 s in ethanol, to remove non-chemisorbed MPA molecules prior to EIS measurement. A different procedure was required for the glass slides prior to IRRAS measurement. The Au coated glass slides were soaked in ethanol over a 12 hr period before being rinsed with water, and then dried, to remove non-chemisorbed MPA molecules.

6.3.4 Electrochemical measurements.

The data in this research is presented as absorbance versus wave number. Each immersion period test was performed in triplicate using a conventional three electrode system with an Autolab potentiostat/galvanostat (Eco Chemie B.V.) in conjunction with Frequency Response Analyser (FRA) software and General Purpose Electrochemical System (GPES) software (Eco Chemie B.V.), for EIS and Cyclic Voltammetry (CV) measurements respectively. The Ag/AgCl reference electrode, platinum wire counter electrode and Au working electrode (MF-2014) were all purchased from BASi instruments Inc and all CV and EIS measurements were performed in PBS.

For EIS, a 0.1 mV amplitude sine wave was applied to the working electrode in the tested frequency range of 0.1 Hz to 1 MHz. An AC frequency of 0.1 Hz was used to obtain the data. This frequency was selected because the mass transfer effects of redox ions are more apparent at this frequency causing a greater number of monolayer properties to influence the impedance data. The working electrode was polarized at a

potential of +0.25 V/Ag(AgCl) during measurements, which was shown via CV to be the oxidation potential of the redox indicator. EIS measurements were performed after the working electrode had been cleaned and again after it had been immersed in MPA solution.

6.3.5 Spectroscopic measurements.

Infrared reflection absorption spectroscopy (IRRAS) spectra were performed using a Varian 7000 FT-IR spectrometer equipped with a step scan interferometer and a liquid nitrogen cooled narrow band detector. The spectra were collected in a vacuum at a resolution of 2 cm^{-1} from 600-6000 cm^{-1}. A reference Au slide was used as background.

6.4 Results and Discussion

6.4.1 EIS measurements

Figure 6.4 shows the data obtained from the EIS measurement for five different temperatures. All five temperatures show two clear ramps followed by plateaux in the record that correspond to two distinct phases of monolayer growth. For the data sets collected for temperatures between 20 ^{o}C and 40 ^{o}C, the first ramp and plateau corresponds to the formation of a monolayer structure (lying down) over an immersion time of between 5 s (0.00139 hrs) and 5 min (0.0833 hrs) and the formation of a second structure (standing up) over 5 hrs to 12 hrs. This is illustrated in Figure 6.4 by the two plateaux occurring on each temperature trace. As expected, the rate of formation of the first structure increases from 20 ^{o}C to 40 ^{o}C. However, the hydrophobicity and structure of the first fully formed monolayers differ greatly between formation temperatures, which are reflected in the impedance magnitude of the first structure plateaux (Huang, 2007).

The data sets are divided by the Gyepi-Garbrah Critical temperature (T_c) (Gyepi-Garbrah and Šilerová, 2001) into two sets. This temperature was defined as being the point at which a SAM structure undergoes a two dimensional phase transition, resulting in a loss of order in the monolayer. For a MPA monolayer, T_c is shown to lie in the range of 20 ^{o}C to 25 ^{o}C in Figure 6.4. Two data sets were measured below T_c at 4 ^{o}C and 20 ^{o}C. Three experiments at 25 ^{o}C, 30 ^{o}C and 40 ^{o}C were carried out

above this temperature and the formation of the monolayer structures was observed to be different.

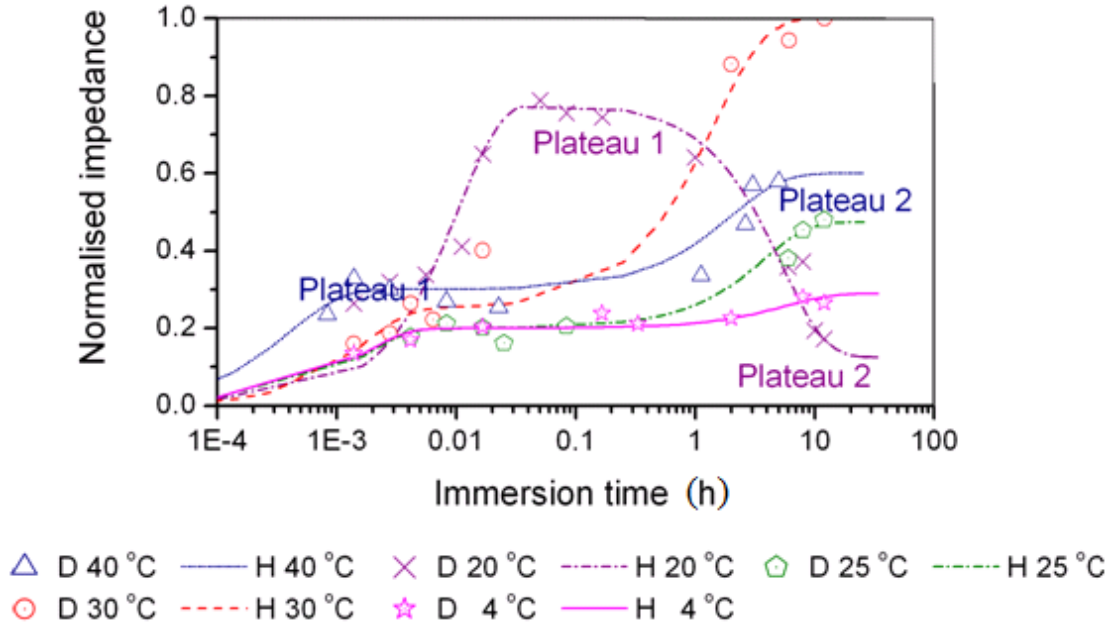

Figure 6.4: A normalized impedance plot comparing the predicted values of the proposed adsorption isotherm models (H 40 °C, H 30 °C, H 25 °C, H 20 °C and H 4 °C), to the normalised experimental impedance data, obtained at 0.1 Hz, (D 40 °C, D 30 °C, D 25 °C, D 20 °C and D 4 °C).

6.4.1.1 Immersion data collected at 4 °C.

During adsorption of the first structure at 4 °C, the rate of adsorption of MPA was higher than that of the rate of adsorption of MPA at 20 °C. This was due to the decreased solubility of the MPA in ethanol. In accordance with the principles of the Kisliuk adsorption isotherm, as applied to SAMs (Dannenberger et al, 1999), this considerably weakened the force that ethanol molecules exerted on the MPA molecules in the precursor state, which act to drive the molecules back into solution. Thus, MPA molecules are more readily adsorbed to the surface of the substrate than at a temperature of 20 °C.

It can also be seen from Figure 6.4 that the first plateau at 4 °C occurs at a much lower impedance than the 20 °C data set. This implies that the monolayer structure is different between the two cases. Moreover, it can be deduced that a porous disordered monolayer is initially formed and that the gradual ramp preceding the formation of the 2nd plateau corresponds to the reduction in monolayer pinhole defects

until the monolayer becomes saturated and the second plateau is attained. In this respect, the 4 ^{o}C data set is unique as no phase transitions occur in the monolayer over the immersion times investigated.

6.4.1.2 Immersion data collected at 20 ˚C.

Over the first 5 minutes, at 20 ^{o}C, MPA molecules form an ordered fully formed lying down structure (shown in Figure 6.1). The structure forms as MPA molecules adsorbed onto the surface of the electrode as insulating ~~"~~islands" that grow with immersion time (Schreiber, 2000; Barrena et. al, 1999). This can be represented by the Gibbs free energy equation, shown in equation (6.1), where ΔG_{ads1} is the Gibbs free energy of MPA adsorption (dictated mainly by the S-Au interaction); ΔH_{ads1} is the enthalpy evolved from adsorption; T is absolute temperature; ΔS_{ads1} is the entropy introduced as a result of MPA molecule adsorption.

$$\Delta G_{ads1} = \Delta H_{ads1} - T\Delta S_{ads1} \quad (6.1)$$

The electrically insulating islands grow as a function of immersion time until the substrate surface is covered and the monolayer enters a transitional state structure, whereby hydrocarbon chains of MPA immobilized on the substrate are displaced by thiol groups of other MPA molecules being adsorbed onto the substrate (Schreiber, 2000). This is shown in Figure 6.4 by the shift in impedance levels between plateaux 1 and 2 and can be represented in the energy balance shown in Equation 6.2. ΔG_{ads2} is the Gibbs free energy of MPA adsorption over the transitional structural formation stage and $\Delta G_{R\text{-}Au}$ is the Gibbs free energy evolved from the MPA chain-Au Van Der Waals interactions.

$$\Delta G_{ads2} = \Delta G_{ads1} - \Delta G_{R\text{-}Au} \quad (6.2)$$

Upon comparing equation (6.1) and equation (6.2), it can be seen that $\Delta G_{ads2} < \Delta G_{ads1}$ thus the rate of adsorption in the transitional structure phase is slower than in the case of initial adsorption (See Figure 6.4). Structure 1 (the lying down structure) has high impedance due to the hydrophobic layer formed by the exposure of the carbon chains to the MPA-Electrochemical solution boundary. Structure 2 (standing up structure) corresponds to an increase in the number of oxygen and hydrogen atoms being orientated toward the solution-monolayer boundary, which in turn has low impedance and is an indication of increased monolayer disorder. Also, during MPA molecule adsorption in the transition phase, the densely packed (standing up) MPA structure (See Figure 6.4) gradually forms (Sawaguchi et al, 2001).

In this instance, sulfur molecules are spaced at a constant distance of 4.53 $\mathring{A}$ from each other as a result of a force equilibrium of strong attractive and repulsive intermolecular forces established between adjacent MPA molecules. This standing up structure does not allow any further MPA molecules to be adsorbed onto the substrate from the solution to form an even more densely packed structure therefore the second plateau, of low impedance, is formed. Thus, it can be deduced that the rate of formation of the standing up structure in the transitional phase is proportional to the amount of MPA in the lying down structure, present on the substrate.

6.4.1.3 Immersion data collected above the Gyepi-Garbrah critical temperature: Temperature effects on the formation of the first adsorbed structure at 20°C and above Tc.

The initial impedance gradients leading to plateau 1 (See Figure 6.4), increase with temperature. This suggests that the rate of formation of the first adsorbed structure increases with temperature above T_c.

For the temperature increase from 20 ^{o}C to 25 ^{o}C, the impedance level of plateau 1 is observed to drop significantly. Gyepi-Garbrah and Šilerová (2001) suggested that this may be result of an increase in disorder of the first monolayer with a structure exhibiting decreased impedance. The hypothesis, commensurate with Gyepi-Garbrah suggestion, is that structure 2 (standing up structure) forms at the same time as the normal growth of structure 1 across the surface. The first plateau in the impedance

trace (See Figure 6.4) is the result of a pseudo-steady state situation where a balance is struck between the formation rates of the two structures; high impedance structure 1 and low impedance structure 2. The relative impedances cancel each other out to give constant impedance. When the surface is covered fully no more structure 1 can form, the balance is broken, and the impedance starts to rise as structure 1 is replaced with structure 2.

Disorder continues to increase with increased temperature from 25 ^{o}C to 40 ^{o}C because the relative rates of formation change between the two structures favouring structure 2 formation at higher temperatures. If the impedance is only a function of the structure of the monolayer one would expect the impedance to fall. However as the rate of formation of structure 2 increases then more imperfections/faults in the structure 2 occur (Gyepi-Garbrah and Šilerová, 2001). These imperfections act to increase the hydrophobicity of the layer and cause the impedance to rise.

6.4.1.4 Immersion data collected above the Gyepi-Garbrah critical temperature: Temperature effects on the formation of the second adsorbed structure at 20^{o}C and above T_c.

Figure 6.5 shows a plot of final impedance value versus temperature of the data measured above T_c. The impedance exhibits a steady rise, which is caused by the increase in imperfections in the structure 2 monolayer for the temperatures 20 to 30 ^{o}C. The trace then shows a drop in impedance for the 40 ^{o}C result. Gyepi-Garbrah and Šilerová (2001) observed an increase in monolayer porosity as immersion temperature increases above T_c that would give a drop in impedance. It is clear that the imperfections due to increased porosity now dominate the impedance of the monolayer and explain the drop in impedance observed.

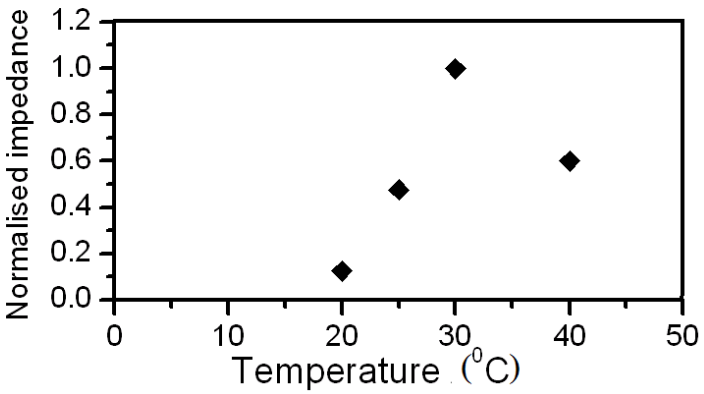

Figure 6.5: Showing how final monolayer normalized impedance measured at 0.1Hz varies with immersion temperature as a result of monolayer structural differences.

6.4.2 Equivalent circuit analysis.

The next step of the analysis of the impedance data was to apply the equivalent circuit analysis (See Chapter 2) to describe the surface properties of each identified MPA structure formed on the substrate surface. The equivalent circuit used for this system is shown in Figure 6.6.

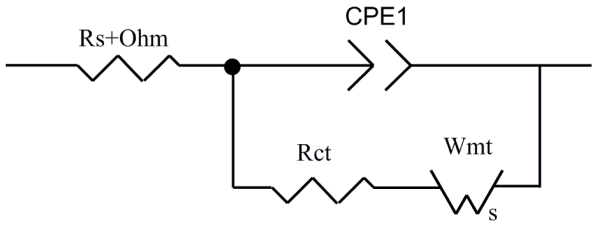

Figure 6.6: Equivalent circuit modelling the behaviour of MPA-coated gold working electrode.

The value Rs+Ohm (is the uncompensated resistance of the electrochemical solution and all physical circuit connections. It was determined by fitting the equivalent circuit to the equivalent circuit complex impedance plot for the cleaned gold electrode).

A single equivalent circuit element, CPE1, (See Figure 6.6) was used to model the capacitance of the circuit arising as a result of two contributions. The first capacitance contribution is due to the permanently adsorbed MPA. The second contribution arises due to a temporary layer (double layer) formed by solution molecules and charged ions in the electrochemical solution. This layer of charged ions disperses when the applied potential difference is removed.

It is difficult to discern between the capacitance contributed to the system by immobilised MPA, and the capacitance of the double layer on the surface of the substrate experimentally and therefore it is most useful to combine these effects in the model.

The equivalent circuit element Rct, (Figure 6.6), is the sum of two forms of charge transfer resistance. These arise from the bare gold working electrode (including potential difference across the double layer and the standard potential of the redox indicator ions), and the charge transfer resistance contributed to the system by the MPA layer.

The remaining term shown in Figure 6.6, Wmt, is the Warburg impedance element which accounts for the mass transfer effects of ions on the detection signal. These are most predominant at low frequency, where the charge transfer current is largely dependent on the rate at which new ions can replace other ions that have been oxidised or reduced at the electrode surface during measurement.

Table 6.1 gives the equivalent circuit values for each element of the circuit obtain by fitting the equivalent circuit model to the data in Figure 6.7 for the two data sets at 4 and 20 °C one point on each plateau for each data set was used as being representative of the structure on the surface at that point in time. The table also presents the parameters when fitted to the impedance spectra for the clean working electrode as a base line reference

Table 6.1: Showing equivalent circuit element values used to model EIS spectra.

Immersion time	Rs+Ohm	CPE1-T	CPE1-P	Rct	Wmt-R	Wmt-T	Wmt-P
Cleaned working electrode surface	98.8	1.081×10^{-6}	1	57.84	3105	48.28	0.483
1st plateau (4 °C)	98.8	1.239×10^{-6}	0.8929	242.7	3.527×10^{6}	2.333×10^{8}	0.449
2nd plateau (4 °C)	98.8	8.657×10^{-7}	0.9225	252.5	5.580×10^{6}	2.120×10^{9}	0.421
1st plateau (20 °C)	98.8	1.403×10^{-6}	0.8951	412.9	1.013×10^{6}	4.277×10^{7}	0.423
2nd plateau (20 °C)	98.8	9.839×10^{-7}	0.9988	154.3	106610	207450	0.440

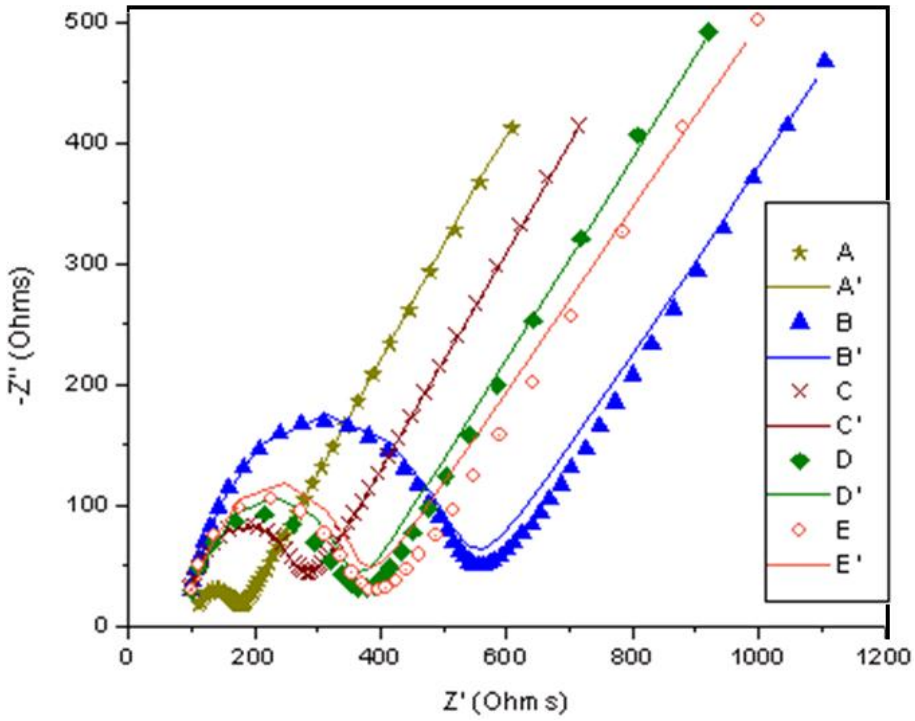

Figure 6.7: Nyquist impedance plots of a cleaned gold electrode (A) with its equivalent circuit fit (A‘) and MPA modified electrodes corresponding to: the 1st plateau formed at 20 °C (B), the 2nd plateau formed at 20 °C (C), the 1st plateau formed at 4 °C (D), the 2nd plateau formed at 4 °C (E) and corresponding equivalent circuit fits (B‘, C‘, D‘ and E‘ respectively).

6.4.2.1 Results of the analysis for the EIS data collected at 20 °C

High values of Wmt-R and Wmt-T were obtained for the data point examined on the 1st plateau at 20 °C. These high values correspond to a high Warburg impedance which is indicative of low mass transfer in the electrochemical solution that corresponds to low diffusion rates for the redox indicators. In the case of short chain thioalkane SAMs, electron transfer across an MPA layer to an electrode is electron tunnelling based (Bard and Faulkner, 2001), thus redox ions do not pass through the MPA layer. It is thought that the diffusion coefficient of the redox species to the electrode surface is altered as a result of the hydrophobic effects, brought about by the presence of the MPA monolayer (Huang et al, 2007).

At 20 °C, after the immersion time in which the 1st plateau can be measured, hydrophobic structure one (which has a large charge transfer resistance and high CPE

admittance) and a small amount of hydrophilic structure two (which has a low CPE admittance, indicating dense monolayer formation, and a small charge transfer resistance) are thought to be present on the electrode surface. As more MPA adsorbs itself to the surface, the entire monolayer surface is saturated with structure 2, with carboxylic acid groups orientated toward the solution boundary. This gives rise to smaller charge transfer resistance and admittance, indicating hydrophilic behaviour. As a result of this behaviour, the redox ion diffusion coefficient increases, which in turn causes Wmt-R and Wmt-T to decrease.

6.4.2.2 Results of the analysis for the EIS data collected at 4 ^{o}C

Unlike its 20 ^{o}C counterpart, it is believed that at 4 ^{o}C a disordered monolayer forms after the immersion time yielding plateau 1. This is reflected in the Rct and CPE1-T measurements for the two layers, where plateau 1 at 20 ^{o}C and 4 ^{o}C yield significantly different Rct and CPE1-T values. Moreover, the disorder exhibited by the monolayer at 4 ^{o}C rendered it hydrophobic (resulting in high Wmt-R and Wmt-T values). Plateau 1 at 4 ^{o}C was also revealed to be porous, which is reflected in the CPE1-T value for the plateau 1 being much greater than that of the plateau 2 dataset (Table 6.1). After plateau 1 is observed, the density of the monolayer increases with time, resulting in a decrease in porosity (causing the CPE1-T value to decrease) until the monolayer is saturated with MPA. At this point, no further MPA adsorption occurred and plateau 2 was observed. The disorder of the monolayer occurring in the 2nd plateau at 4 ^{o}C also causes the Rct value to be only slightly greater than that of plateau 1. In contrast, the change in Rct between the 2 plateaux at 20 ^{o}C is very high due to the reorientation of the monolayer molecules.

6.4.2.3 EIS data collected from the cleaned electrode

As expected, the spectra obtained from a cleaned gold working electrode revealed that the electrode surface was the most hydrophilic of all the EIS datasets shown in Figure 6.7. This gave rise to low Wmt-R and Wmt-T values, indicating high diffusion coefficients of redox active species to the surface of the working electrodes. Moreover, the double layer was revealed to be homogeneous and thin, as the CPE1-P value indicated ideal capacitive behaviour and, of all the datasets shown in Figure 6.7, the cleaned working electrode Rct value was lowest. Mass transfer of redox ions was also revealed to be the most ideal at the cleaned working electrode surface, as the Wmt-P was closest to 0.5.

6.4.3 IRRAS study at 20 ˚C: Verification of changes in monolayer absorbance as a function of immersion time.

To verify the EIS results obtained in the model case, at 20 ^{o}C, an IRRAS study was conducted, which was used to quantify the amount of MPA present on the surface of a Au coated glass slide with immersion time.

To enable the identification of MPA, the assignment of the observed vibrational mode (obtained via IRRAS) was determined by spectral comparison with Fourier Transform Infra Red (FTIR) spectra. A special sample containing a large amount of MPA was prepared by doping the surface of an Au-plated glass slide with 0.05 M solution of MPA in ethanol. The ethanol was allowed to evaporate leaving a large amount of MPA deposited on the surface. The amount of MPA on this sample was quantified using an Attenuated Total Reflectance (ATR) element to measure the FTIR spectrum.

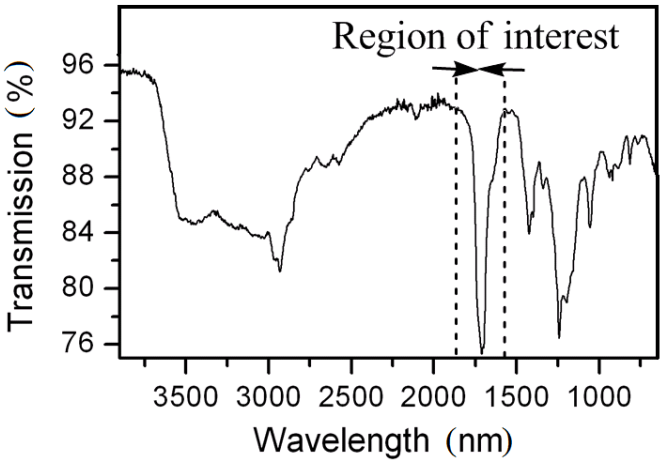

Figure 6.8:. ATR-FTIR spectra of MPA deposited on an Au substrate.

IRRAS was then used to analyze deposition of MPA on to the Au surfaces of the immersed samples used to monitor the self assembly process for the monolayer at 20 ^{o}C. The IRRAS spectrum exhibited a weak but apparent mode (1717-1750 (acids) C=O (H-bonded)) that revealed the composition of MPA monolayer on the Au surface as shown in Figure 6.9. The spectra response is much weaker than the doped sample because much less MPA is present on the surface for the immersion sample. The results indicate that a complete monolayer had formed after an immersion time of 15 min. However, due to low signal strength, it was difficult to determine the formation of standing up structure between an immersion time of 15 min and 16 hrs.

The IRRAS data (shown in Figure 6.9) and the EIS measurements (shown in Figure 6.4 at 20 ^{o}C) differ in that the immersion time required to achieve saturation of the electrode surface is much faster, occurring after an immersion time of 5 min with EIS. This can be attributed to a greater degree of contamination of the IRRAS substrate surface than with the EIS working electrode after cleaning. A gentler cleaning regime was employed to clean the IRRAS substrates to avoid damaging them. As a result, IRRAS substrate MPA immobilization kinetics were hampered as collisions with the Au surface not only had to have enough energy to bind with the substrate surface, but also displace the remaining surface contaminants.

The IRRAS C=O peak exhibits a shift in wavenumber in comparison to the C=O peak yielded from the FTIR, thereby demonstrating that the MPA forms ordered structures when incubated in ethanol solution at 20 ^{o}C and that MPA molecules are merely

deposited in random orientations when MPA-ethanol solutions are simply doped onto the Au surface and left to evaporate.

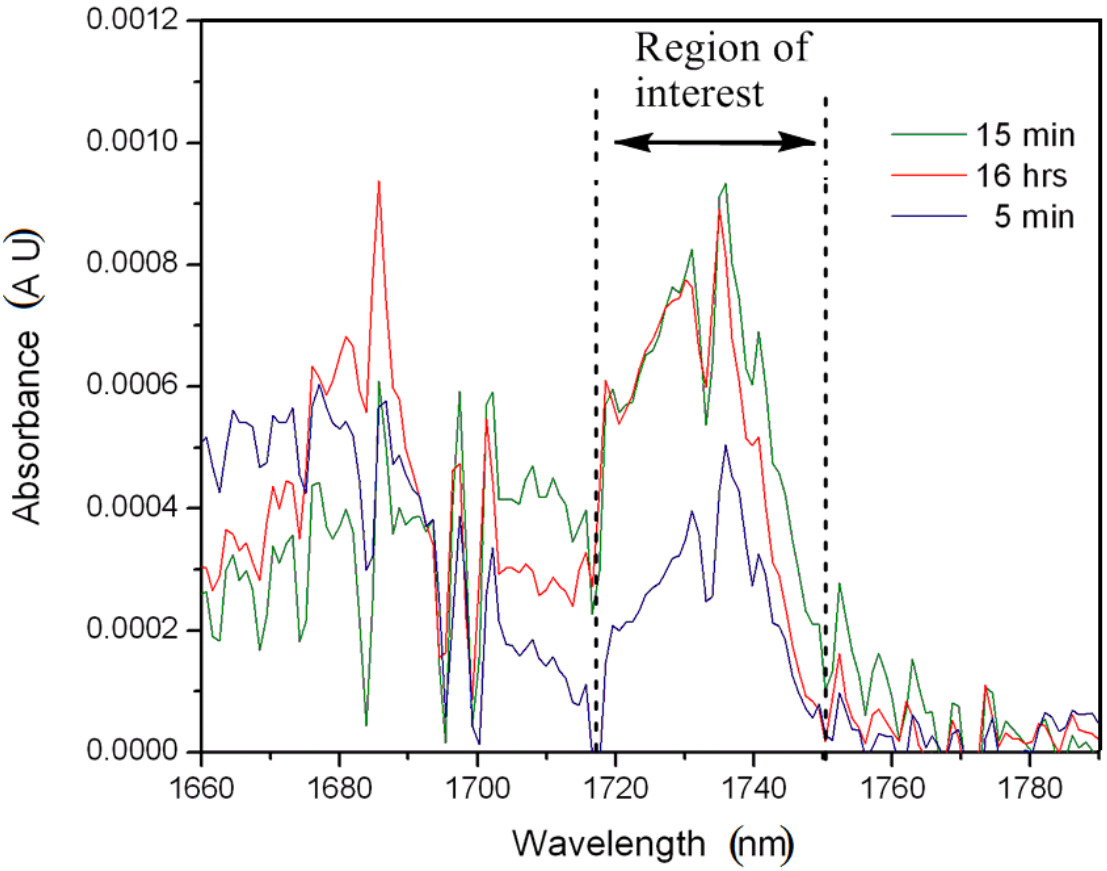

Figure 6.9:. IRRAS spectra of MPA monolayers immobilized at 5 min, 15 min and 16 hrs. The spectrum shows a weak but apparent mode (1717-1750 (acids) C=O (H-bonded)), [see region of interest] that revealed the composition of MPA monolayer.

6.5 Modelling the results.

6.5.1 Development of a new model.

The experimental data suggest that the mechanism for layer formation involves the formation of two distinct structures on the surface and that these structures are formed sequentially. Kisliuk and/or Langmuir models can be used to model initial growth of the first structure on the substrate because the adsorption rate is dictated by the availability of binding sites. The number of possible binding sites for MPA occupying the first structure is solely a function of the number of MPA molecules bound to the Au surface.

Modelling the formation of the second structure is more complicated as formation of the first structure on the substrate surface is a prerequisite to the formation of the second structure. The complexity increases for temperatures above T_C where the second structure starts to form in small patches of structure one (See Figure 6.10) deposited on the surface before a complete monolayer of the first structure is established. The number of possible binding sites for the second structure is dependent on two factors: Factor 1 is the availability of binding sites, which initially increase with immersion time, as area of MPA occupying the first structure on the substrate surface also increases with immersion time as the monolayer grows. Factor 2, as structure 2 forms structure 1 is consumed and eventually the rate of formation of structure 2 exceeds structure 1 and the number of available binding sites for structure 2 formation decrease, as indicated in Figure 6.10.

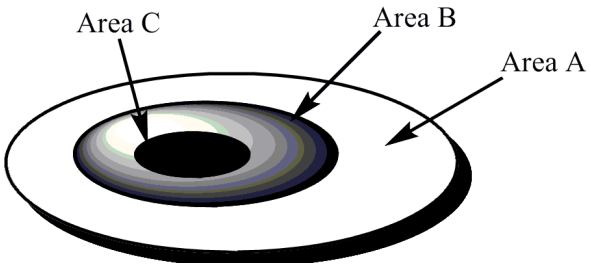

Figure 6.10: Area A: bare Au working electrode substrate surface available for binding to MPA to form the first Au-MPA structure; Area B: the area occupied by the first MPA-Au structure which is available for binding to more MPA in solution, causing the formation of the second structure; Area C: the coverage of second structure, on which no further adsorption or reordering takes place.

6.5.2 Results of fitting the model to the measured data.

The model has been fitted to the experimental data to obtain the PTCS-Kisliuk parameters for each temperature set using the least squares objective function defined in equation (3.46).

The objective function was minimized using the Newton method contained within Microsoft Solver routine and the fitted parameter set as R_1‘, R_2‘, k_{E1} and k_{E2}. The fitted parameters and the goodness of fit to the experimental data are shown in Table 6.2 for each temperature data set.

Table 6.2: The proposed model constant values used to model the experimental EIS data at different immersion temperatures and the fit that the model function provided to this data.

Adsorption temperature (C)	φ_1	k_{E1}	R_1’	φ_2	k_{E2}	R_2’	**Chi squared test (χ^2)**	
							χ^2	**Nº of data points**
40	0.30	0	2500	0.60	0	0.5	0.04674	10
30	0.25	0.60	2000	1.00	0	0.7	0.09681	9
25	0.20	0.60	2000	0.48	0.5	0.7	0.01496	9
20	0.79	0.64	362.2	0.13	0.7	0.8	0.5944	14
4	0.20	0.45	1500	0.29	0.3	0.3	0.01209	9

Rate of adsorption of the first structure shows a positive correlation with temperature, which is in accordance to the principles of the Kisliuk model and is revealed by the trend in the variable R‘$_1$ between temperatures of 20 ^{o}C and 40 ^{o}C. Increased dissociation with increased temperature influences the formation of the second structure, between immersion temperatures of 20 ^{o}C and 40 ^{o}C. This causes the rate constant determining R‘$_2$ to decrease (Dannenberger et al, 1999) with increased temperature. Moreover, it can be seen that the presence of the first structure of MPA

significantly reduces rate of binding in each case, which is shown in the constant R'_2 being significantly smaller than R'_1 (See Table 6.2).

For 25 °C to 40 °C the values of both k_{E1} and k_{E2} decrease with increased temperature. This is as expected, the MPA molecules possess increased enthalpy at high temperatures reducing the significance of molecular interactions which cause $\Theta_{1(t)}$ and $\Theta_{2(t)}$ to deviate from the Kisliuk adsorption model. Indeed the zero values returned for the 40 °C suggest that above this temperature adsorption follows Langmuir adsorption model behaviour.

For the 4 °C data, values of R'_1, R'_2, k_{E1} and k_{E2} do not follow the trends observed for the model curves seen to occur between 20 °C and 40 °C. The adsorption kinetics are different to those observed from 20 °C to 40 °C because decreased solubility of MPA starts to affect the adsorption.

The fitted isotherm models calculated by application of equation (6.8) are displayed with the normalized experimental impedance data in Figure 6.4. The error between the normalized experimental data and the values predicted by the proposed model at 4 °C are shown in Table 6.3. It can be seen from Table 6.2 that a good fit is obtained using the model over all adsorption temperatures investigated, as every temperature dataset provided a χ^2 value significantly less than the number of data points obtained at a particular temperature. The majority of the data is scattered randomly about the model curves and can be attributed to microscopic surface irregularities, brought about during cleaning of the surface. In the typical distribution of error shown in Table 6.3, there is no trend between the amount of error observed and immersion period.

Data provided by Himmelhaus et. al. (2000) showed that vibration mode intensity data yielded by docosanethiol growth on gold displays a similar shaped curve to the adsorption curve displayed for MPA on Au at 20 °C, shown in Figure 6.4. Therefore, it is reasonable to conclude that the modelling equation may also be applicable to other SAM systems. However, it must be noted that, as the nature of the molecular interactions are different, the equation constants will be a function of the molecular interactions specific to the SAM system under consideration.

Table 6.3. Error between the values predicted by the proposed model and the experimental data at a temperature of 4°C

Immersion period (h)	Normalized Impedance		Error (%)
	Predicted by proposed model	Experimental data	
0	0	0	0
0.001389	0.119346	0.135058	11.63344
0.004167	0.190869	0.170344	12.04897
0.016667	0.200242	0.203731	1.712618
0.166667	0.202400	0.237921	14.92957
0.333333	0.204755	0.210885	2.907165
2	0.225783	0.226506	0.318769
8	0.269349	0.279999	3.800433
12	0.280808	0.264786	6.050958
		Average	5.933547

6.6 Summary

The stages of MPA self assembled monolayer growth on a Au working electrode have been characterized and quantified using Electrochemical Impedance Spectroscopy (EIS) at temperatures ranging from 4 ^{o}C to 40 ^{o}C. Infra-red reflection absorption spectroscopy (IRRAS) was used to confirm EIS data at an immersion temperature of 20 ^{o}C.

Changes in the resistance and capacitance of the monolayer over immersion time allowed the recognition of two distinct structures in monolayer self assembly. Initially, MPA occupying the lying down configuration was formed and evolved into a structure consisting of MPA in the standing up configuration. Both structures displayed an increase in disorder with increased immersion temperature above 20 ^{o}C. Also, a disordered structure at an immersion temperature of 4 ^{o}C was displayed as a result of decreased solubility of MPA in ethanol. This allowed the elucidation of a new monolayer model, which was applied to model normalized impedance data and allowed the deduction of the optimum immersion time for formation of complete MPA lying down structure and standing up structure.

The model was found to provide a good fit to all experimental data and it is thought that the new model is suitable for the purposes of modelling the different phases of monolayer growth, as measured via EIS. This allowed the optimum SAM immersion time to be deduced, which was 12 hrs, at the optimum formation temperature of 22 ^{o}C.

It is also expected that this model could simulate many systems which form two sequential structures that exhibit different properties. It is believed that the equation could become instrumental in the optimisation process of carboxylic acid activation with EDC and NHS. Firstly, O-acylisourea intermediate forms as a result of a reaction between EDC and a carboxylic group before an NHS-ester is formed from O-acylisourea and NHS in a nucleophilic substitution reaction.

Chapter 7: Activation of the MPA monolayer using EDC and NHS

7.1 Introduction

The next stage to be considered is activation of the MPA monolayer. Activation is required to increase the reactivity of the MPA monolayer. An intermediate is added to the carboxylic acid layer to catalyse the attachment of organic molecules to the carboxylic surface by reducing the activation energy required. The most common method of activation, uses 1-Ethyl-3-(3-dimethylaminopropyl)-carbodiimide (EDC) and N-hydroxysuccinimide (NHS), (Harmanson, 2008). The activation kinetics of the EDC/NHS have been studied extensively at the molecular level, but little attention has been paid bulk activation kinetics where carboxyl groups are activated over a large planar surface. This study will aim to address this deficiency and propose mathematical models to facilitate the optimization of said process.

7.2 Background

Many studies have been conducted to the investigate activation chemistry of carboxylic acid groups. The most notable of these investigations are spectroscopy based and are featured in a report by Sam et al (2010) and Harmanson (2008).

These studies revealed the forward reaction chemistry and any undesirable by-product reactions. In turn they have led to the sequential theory for the mechanism of the activation process described below

7.2.1 Mechanism for Carboxylic Acid Activation using EDC/NHS

An example of the reactions constituting carboxylic activation can be seen in Figure 7.1.

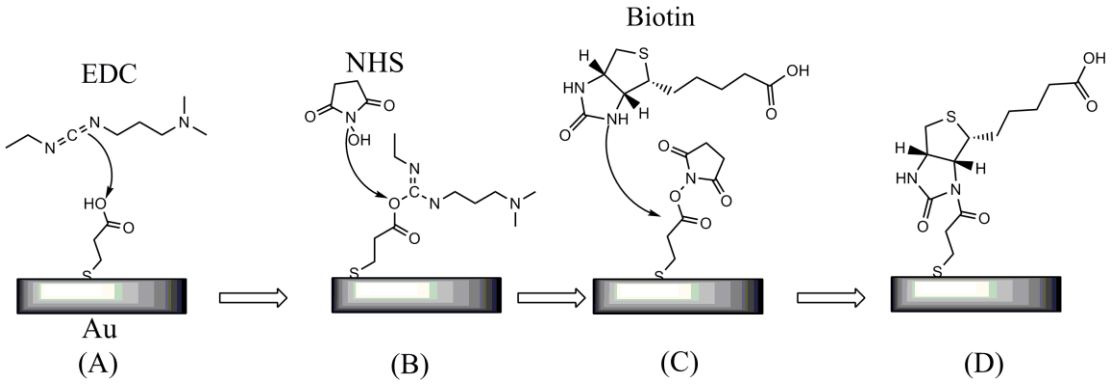

Figure 7.1: Activation reaction stages showing sequential formation of O-acylisourea from EDC and an MPA carboxyl group (A), NHS-ester formation from O-acylisourea and NHS (B), a ligand (for example: biotin) binding to the activated carboxyl group (C) and the final carboxyl-ligand structure (D).

The full mechanism for attaching the organic molecule of interest can be described as a series of steps beginning with EDC ($C_8H_{17}N_3$) and the carboxylic acid group (RCOOH), (see equation (7.1)). The EDC is chemisorbed to the surface to activate the carboxylic acid group. It forms an active *O*-acylisourea (OA) intermediate that can be coupled to an amino group (see Figure 7.1A) (Damink et al, 1996). The activation is undertaken in the presence of water where the *O*-acylisourea is prone to exothermic hydrolysis (Janolino and Swaisgood, 1982) with water to form an isourea derivative and can desorb back into solution (equation (7.2)). In the case of EDC, this derivative is 1-Ethyl-3-(3-dimethylaminopropyl)-isourea ($C_8H_{19}N_3O$).

The instability of the O-acylisourea-carboxylic acid structure necessitates a second step (see Figure 7.1B) where NHS-ester (NHSE) is formed from NHS ($C_4H_5NO_3$). (See equation (7.3)). NHS-ester formation involves a substitution reaction where the EDC is displaced back in to the bulk solution by NHS to form the NHS-ester (in this case N-succinimidyl 3-mercaptopropionate) (Li et al, 1996, Collinson et al, 1992, Staros et al, 1986, Chow et al, 2005, Caruso et al, 1997, Frey and Corn, 1996). The NHS-ester could hydrolyse (Chamberlin et al, 2002) exothermically but this reaction

would take place at a much slower rate than that for O-acylisourea (see equation 7.4). When a complete NHS-ester layer has formed, the EDC/NHS solution is removed.

The final stage is the actual attachment of the desired organic molecule (see Figure 7.1D, where the molecule bound by its amino group is biotin). This process involves a second substitution reaction where amino groups on the molecules (biotin) form covalent links to the activated carboxylic acid group and displace the NHS in to the solution.

The reactions of interest can be summarized as follows:

$$C_8H_{17}N_3 + RCOOH \rightarrow OA \qquad (7.1)$$

$$OA + H_2O \rightarrow C_8H_{19}N_3O + RCOOH \qquad (7.2)$$

$$C_4H_5NO_3 + OA \rightarrow NHSE + H_2O \qquad (7.3)$$

$$NHSE + H_2O \rightarrow RCOOH + C_4H_5NO_3 \qquad (7.4)$$

These four reactions are competing and it is desirable to optimize conditions to favour the production of a complete NHS-ester layer as quickly as possible. The hydrolysis reactions are known to depend on temperature, pH and buffer composition (Jang and Keng, 2008, Wissink et al, 2001). Hence, EDC and NHS coupling reagents are commonly mixed into a single solution and buffered to within a pH range of 4.5 to 7.5 (Sehgal and Vijay, 1994). These conditions promote reaction between NHS and *O*-acylisourea intermediate to form NHS-ester as quickly as possible after the intermediate structure is formed. A low concentration of *O*-acylisourea is maintained on the surface to minimize hydrolysis of the EDC.

7.2.2 Limitations of the spectroscopic studies

Though very useful the spectroscopic studies carried out to date only give a very small snapshot of what is happening on the surface during activation, and it is believed to be impractical to image the entire surface via spectroscopy, Sam et al (2010). When considering the processes as a whole it would also be useful to look at bulk properties of the surface where macro effects on the scale of 0.1 mm^2 or above could give further insight in to the physical processes involved in layer formation.

7.3 Experimental work

The experimental work carried out was designed to answer two questions:

1) Are macroscopic changes in structure of the surface characteristics observed during the EDC-NHS activation process and what do these changes tell us about the structure of the surface?

2) How are the structures of the observed EDC-NHS layers changed by immersion time and temperature?

7.3.1 Investigation of structures present on the surface of the substrate during EDC/NHS activation

Three types of experiment were carried out to determine what structures were present on the surface during activation measurements. A quick simple test using contact angle measurements was used to give the first indication of different structures. FTIR spectra and topological reflectance profiles were used to try to size the observed effects and identify the structures present. Fluorescence spectroscopy was used to look at the complete surface after tagging with fluorescent markers to identify different structures and their distribution.

These experiments share a common method of preparation of the activated layer and will be treated together. The experiments were carried out on glass slides individually coated with gold. The slides were individually cleaned, then coated with MPA before being treated with EDC-NHS to produce the desired activated layers.

7.3.1.1 Experimental procedures for preparation of MPA layers on glass slides

The glass slides were prepared and coated with MPA following the procedures set out in Chapter 6 Sections (6.3.2 and 6,3,3). The slides were coated in MPA solution at 22 ^{o}C for 12 h. These conditions were chosen as the optimum conditions for forming the most homogeneous layer of MPA as proven in Chapter 6. Once coated the MPA modified slides were then rinsed in ethanol to remove non-chemisorbed MPA molecules.

7.3.1.2 EDC/NHS activation procedure

The MPA coated slides were thoroughly rinsed in DI water before being immersed in a solution consisting of EDC (Fluka) and NHS (Sigma) with relative concentrations of 0.5mg/ml and 5mg/ml in 0.1M PBS solution (pH=7.4). The activated slides were then rinsed in DI water to remove NHS and EDC molecules which were not covalently bound to the surface. Contact angle measurement analysis was then performed on the slides. Contact angle measurements were made using a DSA 100, drop shape apparatus (Krüss GmbH.) with a TIC camera (25 fps with high performance frame grabber, Krüss GmbH). The contact angle was used to characterize the relative hydrophilicity or hydrophobicity of the activated surface at room temperature (22 °C).

Additional processing was required to prepare the slides by labelling the activated layer for the FTIR profiling and fluorescent measurements.

7.3.1.3 Bovine Serum Albumin (BSA) labelling for FTIR measurements

FTIR profiling requires a sufficient difference in layer depth between the structure on the surface of the substrate and the substrate surface. The monolayers of *O*-acylisourea intermediate and NHS-ester do not show sufficient layer thickness difference from the original MPA monolayer for the instrument to detect the separate structures. Therefore the activated layer was labelled with Bovine serum albumin (BSA) to provide sufficient contrast in layer depth to allow detection by the FTIR microscope. The BSA also served to stabilise the activated area by preventing hydrolysis of the activated sites during the lengthy profiling process.

The slide was immersed in BSA solution for 0.5 hrs to saturate all activated carboxylic acid sites. The slide was then rinsed in DI water and immersed in PBS solution for 1 hr to desorb non-covalently bound BSA prior to FTIR profiling.

FTIR spectra and topological reflectance profiles were measured using a Nicolet Continuum XL FT-IR microscope (Nicolet). The spectrum for BSA powder was obtained using a Nicolet 5700 FTIR (Nicolet). These measurements were used to confirm that the islands that formed across the surface during activation consisted of either O-acylisourea or NHS-ester, as these molecules alone were labelled with BSA during the BSA labelling stage.

7.3.1.4 BSA labelled FITC for fluorescence measurements

To make florescence measurements of the surface coverage of the different structures at different times it was necessary to attached fluorescent molecules to the areas covered by EDC/NHS molecules. This labelling allows the areas of the substrate that were activated with EDC and NHS to fluoresce when excited by monochromatic light Therefore activated slides were immersed in BSA labelled FITC for 3 hrs to saturate all activated carboxylic acid sites. The slides were then rinsed in DI water and immersed in PBS solution for 1 hr to desorb non-covalently bound BSA prior to fluorescence microscope measurement. Images of fluorescing BSA labelled FITC on the substrate were recorded using an Eclipse TE2000-U microscope (Nikon), whilst the substrate was being excited by light with a wavelength of 494 nm.

7.3.2 Detailed investigation of activated surface for variations in temperature and time of immersion

To address the second aim of this chapter i.e. ―How are the structures of the observed EDC-NHS layers changed by immersion time and temperature?" It was necessary to carry out a more sophisticated analysis of the growth rates and quantify the amounts of different structures on the substrate at a given time. It was decided to use impedance spectroscopy as a quick means of determining the bulk properties of the surface at any time t. Three structures are expected to be present on the surface at any time t: the first will be the original mono layer of MPA; the second will be a areas of *O*-acylisourea created by EDC attaching to the carboxylic groups of the MPA; the final structure will be NHS–ester where molecules of NHS have displaced the EDC from the surface. The impedance is known to depend on the type of structure on the

surface hence the change in impedance can be used to infer the relative change in the quantity of a particular structure on the surface.

7.3.2.1 Electrochemical Impedance Spectroscopy (EIS) and Cyclic Voltammetry (CV) measurements

Each measurement was performed in triplicate using a conventional three electrode system with an Autolab potentiostat/galvanostat in conjunction with Frequency Response Analyser (FRA) for EIS measurements and General Purpose Electrochemical System (GPES) software (Eco Chemie B.V.) for CV measurements. The Ag/AgCl reference electrode, platinum wire counter electrode and Au working electrode (MF-2014) were all purchased from BASi instruments Inc and all electrochemical measurements were performed in PBS buffer solution.

The working electrodes were prepared in accordance with the procedures set out in Chapter 6 to produce a MPA coated electrode. The MPA layer itself was produced by immersing the cleaned electrodes in MPA solution at 21 ^{o}C for 12 h. These conditions were used because they have been shown to be the optimal conditions to produce the most homogenous layer of MPA on electrodes (see Chapter 5). The working electrodes were subsequently ultrasonicated for 2 min 30 s in ethanol, to remove non-chemisorbed MPA molecules prior to EIS measurement. The EDC/NHS activation was carried out by first rinsing in DI water before immersing the electrodes in EDC/NHS solution for different periods of time and different temperatures. Activated working electrodes were then rinsed in PBS to remove NHS and EDC molecules which were not covalently bound to the surface prior to EIS measurements.

The EIS, measurements themselves were carried out by applying a 0.1 mV amplitude sine wave to the working electrode in the tested frequency range of 0.1 Hz to 1 MHz. The working electrode was polarized at a potential of +0.25V/Ag(AgCl) during measurements, which was shown via CV to be the oxidation potential of the redox indicator. EIS measurements were performed after the working electrode had been cleaned, after it had been immersed in MPA solution and after EDC/NHS solution immersion. Stable complex impedance plots indicated that an undetectable amount of hydrolysis occurred during EIS measurements.

7.4 Results and Discussion

7.4.1 Contact angle measurements

MPA, O-acylisourea and NHS-ester all have a different hydrophobicity and will therefore exhibit different characteristic contact angles. Measuring the contact angle of a water droplet with the substrates is therefore a crude, simple test to see if a substantial area of given substance at a given time is present (>0.1mm^2) on the surface. However if successful it should give proof that different structures are forming on the surface in significant quantities and a guide to the relative times of formation of the different structures.

Figure 7.2, displays a sequence of distilled water droplets on the surface of the sample (approximately 2 mm in diameter) at 22 ^{o}C after different immersion times of 0 hrs, 0.167 hrs, 0.667 hrs and 2.5 hrs. The contact angles were then measured and recorded in Table 7.1

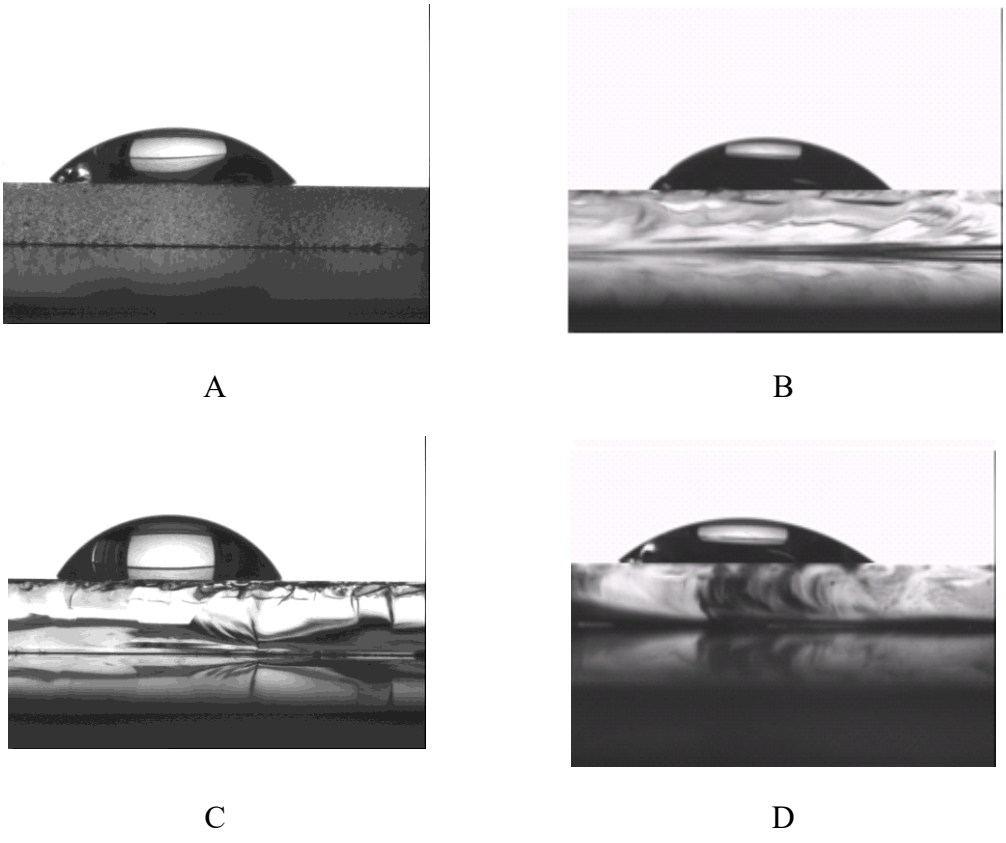

Figure 7.2: The contact angle that double distilled water forms with an MPA surface modified with EDC and NHS at an EDC/NHS solution immersion time of: A, 0 hrs; B, 0.167 hrs; C, 0.667 hrs and D, 2.5 hrs

The sequence of measurements shows the formation of two distinct structures over the sample surface. Figure 7.2A shows a droplet of water on a layer of MPA not treated in EDC/NHS. The measured contact angle is 53° and consistent with the known low hydrophobicity of the MPA layer (Zhou and Walker, 2006).

Table 7.1: Measured contact angle of a double distilled water drop on an EDC/NHS modified MPA surface.

Immersion time (hours)	Contact angle (degrees)
0	53
0.167 (10 min)	Left: 59 Right: 53
0.667 (40 min)	62
2.5	39

Figure 7.2B is perhaps the most interesting of the results. The contact angle on the left hand side is 59° and is much greater than that on the right hand side of 53°. By serendipity it appears the droplet had formed across the island boundary of two separate substantial monolayers. The 53° angle seems to correspond with that measured for a layer of MPA in Figure 6.2A, the 59 ° is within the margin of error for the measurement made for O-acylisourea in Figure 6.2C of 62°. The presence of a large area of O-acylisourea and one of MPA implies that adsorption/reaction of the EDC with the surface is influenced by the presence of EDC molecules already on the surface. This is commensurate with other adsorption studies conducted into similar sized molecules in the field of self assembled monolayers (Dannenberger et al, 1999), (Henderson et al, 2009).

Figure 7.2C shows the droplet on the surface after 40 minutes of immersion in EDC/NHS solution. The contact angle has increased to 62^{o}. This rise is commensurate with the increase in hydrophobicity due to the formation of a large amount of O-acylisourea in a continuous layer on the substrate surface.

Figure 7.2D shows the droplet on the surface after 2.5 hours of immersion in EDC/NHS solution. The contact angle has dropped to 39° and indicates the presence of a large area of a third structure on the surface this is most probably NHS-ester, the most hydrophilic layer of the three monolayers formed.

7.4.2 FTIR microscope profiling.

The contact angle measurements are crude and difficult to repeat therefore to verify the contact angle measurement findings, an FTIR microscope was used to profile another surface modified with MPA, this time activated for 30 min.

Figure 7.3 represents the FTIR analysis of BSA powder. Peaks occurring around the 1500-1800 cm^{-1} region correspond to the BSA primary and secondary amine groups. These peaks were found to effectively distinguish BSA from the other components on the surface. Hence, the IR reflectance topological profile for a wavenumber of 1644 cm^{-1} was chosen for analysis.

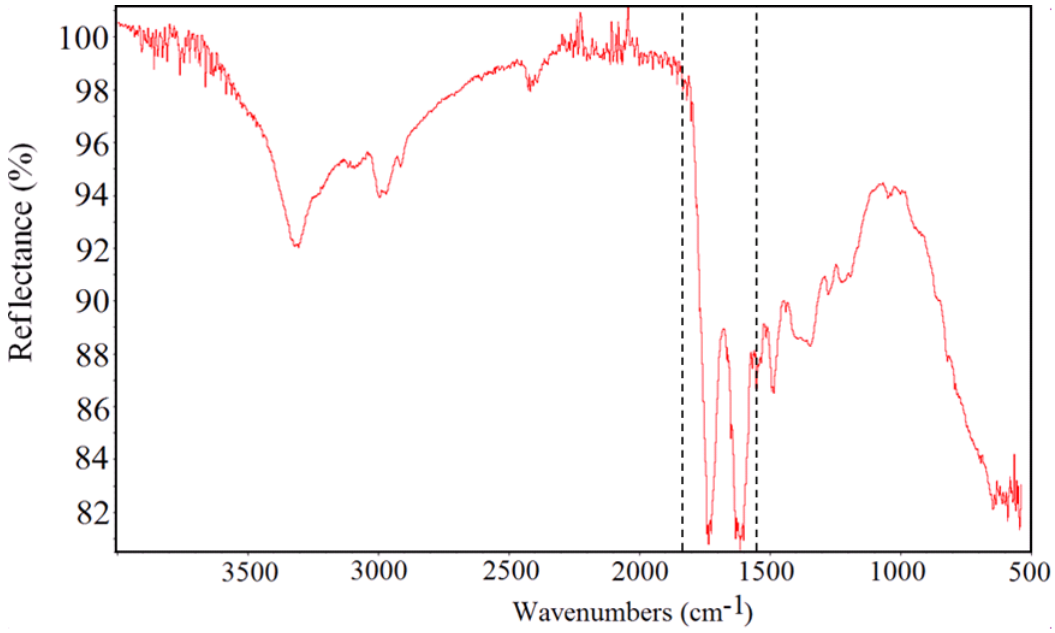

Figure 7.3: The FTIR reflectance profile of BSA powder showing peaks occurring in the range of 1500-1800 cm^{-1}, corresponding to the BSA primary and secondary amine groups.

Figure 7.4 is the resultant IR profile for this sample. It clearly shows the edge of an activated island that is at least 500 μm long that has been tagged with BSA. This

clearly demonstrates the existence of large islands of activated molecules (O-acylisourea or NHS-ester) across the surface of the substrate and confirms the contact angle measurement findings.

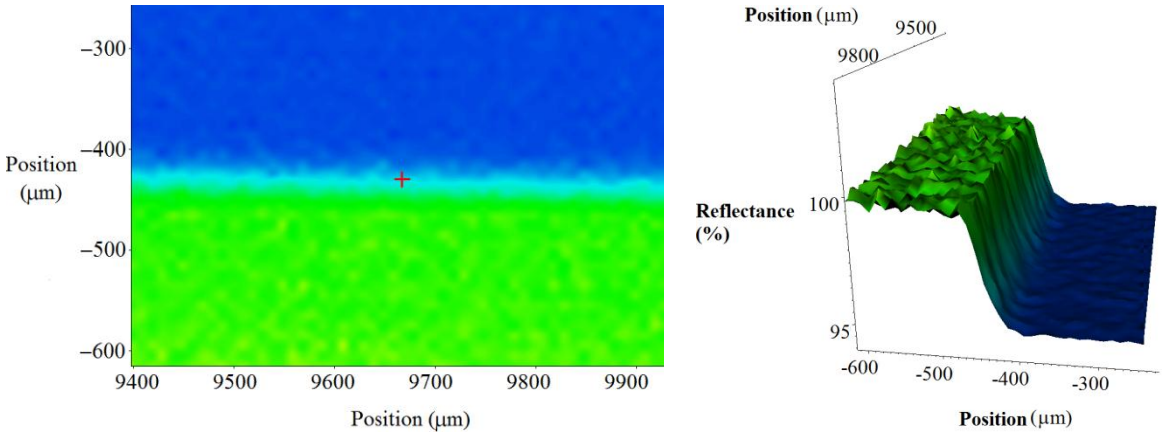

A B

Figure 7.4: IR profile of the surface the green layer indicates presence of the island boundary where blue indicates the surface of the activated layer covered in BSA and green the area of unactivated MPA. The 100 micron scale interval indicates the bounday must be long and thus the island of activated surface covers a substantial continuous area.

7.4.3 Fluorescent measurements

Three fluorescence measurements were carried out at 0 hrs, 30 minutes and 2.5 hrs immersion times in EDC/NHS solution. The zero hour sample resulted in a wholly black side indicating that the fluorescence markers do not tag areas of inactivated surface.

The results of the 30 minute sample are presented as three images of different parts of the treated surface in Figure 7.5.

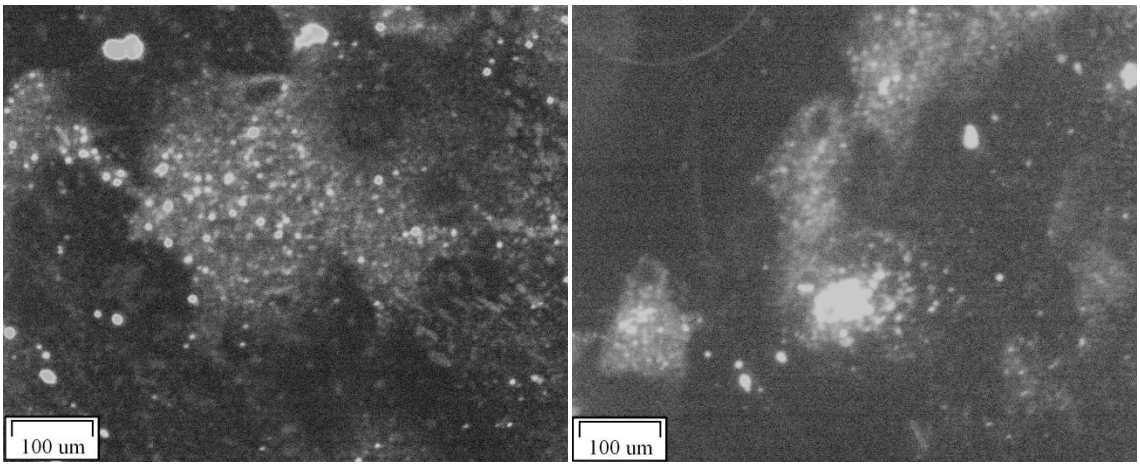

A B

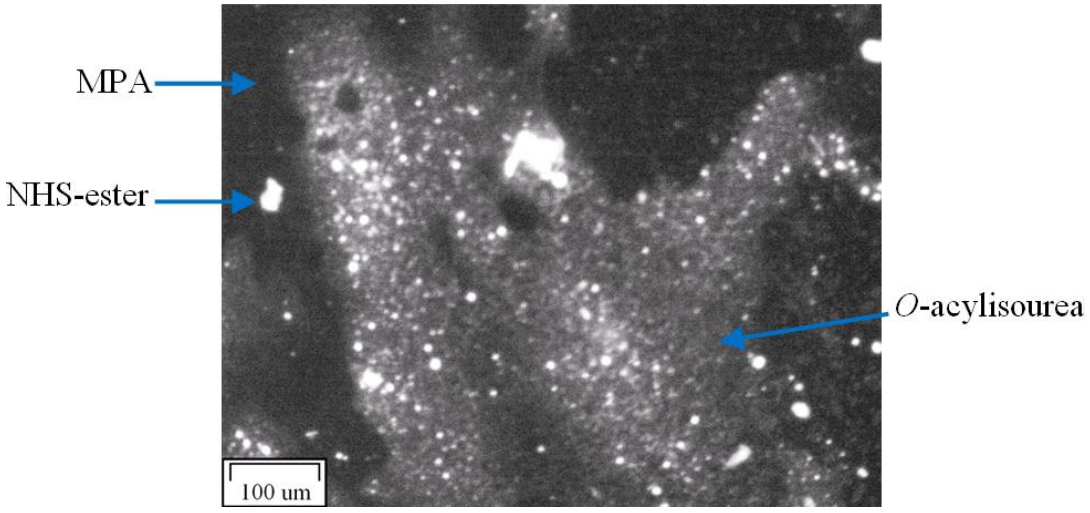

C

Figure 7.5: Shows fluorescent images for a slide immersed in EDC/NHS solution for 30 minutes. Each image represents a different area of the same substrate. Dark areas are known to show the location of unactivated MPA. The light grey areas are thought to show location of O-acylisourea and the intense white areas are thought to show the location of NHS-ester.

Figure 7.5 shows a series of activated islands on a single substrate labelled with BSA labelled FITC. The unactivated MPA are shown as the dark areas of the substrate, which did not fluoresce as the unactivated groups were incapable of covalently binding with the BSA-FITC flourophore.

The light grey islands outline the position of O-acylisourea prior to labelling and it is thought that the white areas correspond to the position of NHS-ester prior to labelling.

The contrast in colours between these two different types of activated site indicates that BSA-FITC is more concentrated over molecules activated with NHS-ester than with molecules activated with O-acylisourea. It is interesting to note that the bright white spots are surrounded by the lighter grey areas confirming that NHS only grows on substantial areas of O-acylisourea. This confirms that the two layers grow sequentially.

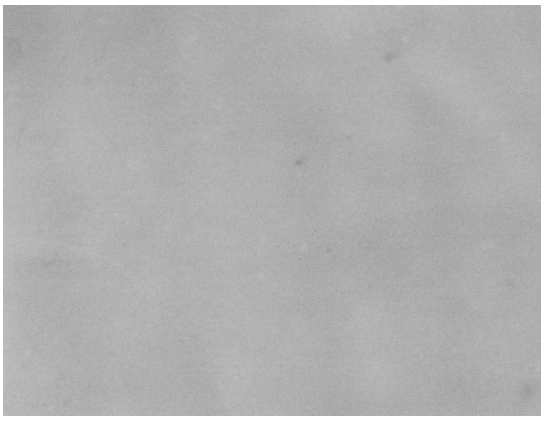

Figure 7.6: Fluorescent images for a slide immersed in EDC/NHS solution for 2.5hours. The slide is completely grey. This indicates the surface is completely activated by NHS-ester. Note, the slide appears to be grey instead of white because the image intensity has been reduced to allow a viable image to be produced.

The final image in the sequence was made for an immersion time in EDC-NHS solution of 2.5 hours (See Figure 7.6). The sensitivity of the instrument was reduced to compensate for the high concentration of fluorescent molecules on the surface hence the surface appears grey instead of brilliant white. The even coloration of the slide indicates an even distribution of BSA-FITC across the surface which in turn indicates that on the macro scale the surface was evenly activated by NHS-ester.

These results taken as a whole seem to support the idea of different structures forming on the surface at different times and that species adsorbed on the surface influence the development of the surface through island growth.

7.4.4 Impedance measurements produced by EIS

Each activated sample was analyzed by EIS to produce a Nyquist impedance plot. The level of impedance is known to depend on the type of structure on the surface. Areas covered with MPA, O-acylisourea and/or NHS-ester monolayers formed under different conditions can thus display different impedance values. To eliminate the

effect of the MPA the results were normalized against the zero immersion time sample, coated in MPA alone. An example of these results is given as a plot of normalized impedance versus immersion time for the isotherm at 22 °C in Figure 7.7.

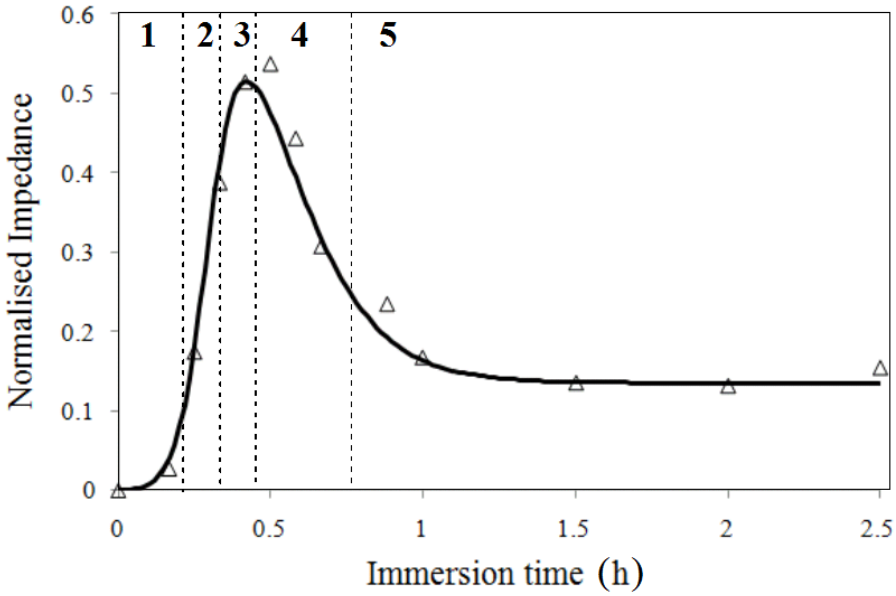

Figure 7.7: The normalized impedance –time plot for the 22 °C. Five different stages of layer growth (denoted by 1, 2, 3, 4 and 5 in bold) are suggested by the isotherm.

The impedance profile (Figure 7.7) displays an ordered trend, indicating that an insignificant amount of desorption of hydrolysed O-acylisourea molecules occurred during the actual EIS measurements. It can also be seen that there are five distinct stages of layer growth.

7.4.4.1 Stage 1

In stage 1 there is a slow increase in the normalized impedance, indicating that almost all layer formation is that of O-acylisourea and occurs through random adsorption of EDC molecules. This adsorption occurs at locations that are sufficiently remote from each other, that the molecular interactions between EDC and O-acylisourea on the surface do not affect the rate of new O-acylisourea layer formation. Such behaviour has also been observed in adsorption studies carried with similar sized SAM molecules (Dannenberger et al, 1999).

The term used to describe this process is –island seeding" (Dannenberger et al, 1999). As further O-acylisourea adsorption takes place the rate of impedance rise increases.

This is indicative of interactions between O-acylisourea present on the substrate and EDC molecules in solution. This interaction promotes O-acylisourea molecules to form adjacent to other O-acylisourea molecules already present on the surface and is commensurate with island formation kinetics reported for similar sized molecules (Dannenberger et al, 1999, Henderson et al, 2009). NHS-ester formation over this stage is minimal as there is very little O-acylisourea available on the modified substrate surface

7.4.4.2 Stage 2

The effect of adsorption through O-acylisourea island growth becomes dominant in this stage of layer formation (See Figure 7.7). During adsorption via island growth, the additional EDC–O-acylisourea interactions promote rapid adsorption to the surface around the island fringes. As adsorption occurs, the size of the island increases as does island fringe itself. The size of the island fringe is the rate limiting factor in adsorption via island growth and an exponential rise in adsorption should be expected.

However, NHS-ester formation on the surface during this stage is also more significant than in stage 1 because there is an increasing amount of O-acylisourea available for the substitution reaction to occur. As NHS-ester molecules displace EDC back in to solution they act to reduce impedance measured. An equilibrium condition arises between growth of the O-acylisourea islands and NHS-ester formation. This equilibrium is indicated by the near linear increase in impedance observed in this stage. The exact nature of the early stages of NHS-ester growth cannot be deduced from the data in Figure 7.7 as the impedance contribution from the more rapid O-acylisourea growth dominates.

7.4.4.3 Stage 3

During stage 3 the depletion of MPA sites restricts the rate of O-acylisourea formation. At the same time, the rate of NHS-ester growth increases as more O-acylisourea becomes available. The net result is a decrease in the rate of change of the impedance which eventually leads to the impedance maxima, where the impedance rise due to the formation of O-acylisourea is matched by the fall in impedance due to the formation of NHS ester. At the point of saturation O-acylisourea, it is expected that there is a large NHS-ester presence on the substrate

surface. It should be noted that the peak impedance value in stage 3 (Figure 7.7) does not reflect the impedance value obtained from a layer comprising entirely of O-acylisourea.

7.4.4.4 Stage 4

In Stage 4, the impedance is observed to fall. This is indicative of a shift in the equilibrium between formation of NHS-ester and O-acylisourea. NHS-ester formation becomes the dominant mechanism. The rate of decrease of the impedance is initially slow but speeds up as the immersion time increases. This is indicative of the autocatalytic effect accompanying adsorption via NHS-ester island growth. The average rate of decrease of impedance over stage 4 is observed to be less than the average rate of impedance increase over stage 2. In stage 2, O-acylisourea formation is the dominant process which leads to the deduction that NHS-ester formation is a slower process than O-acylisourea formation and consistent with the extant literature (Glaser et al, 1999, Sam et al, 2010).

7.4.4.5 Stage 5

During stage 5 formation, impedance settles at a constant value indicative of NHS-ester saturation.

7.4.5 Temperature effects on the activation process

The impedance profile at 22°C is considered to represent the ‗ideal' profile because it demonstrates an O-acylisourea peak at plateau 1 and has a stable final impedance, which corresponds to a high yield of NHS-ester being present in the final structure. Most of the other isotherms (see Figures 7.8 and 7.9) display profiles generally similar in shape to that described in Figure 7.7 and indicate the sequential formation of O-acylisourea followed by NHS-ester layers.

The shapes of the EIS adsorption profiles do show some deviations which appear be temperature dependant, indicating that temperature has an effect on the rates of formation of the O-acylisourea and NHS-ester structures. These deviations can be attributed to the stoichiometric reactions described in equations (7.5), (7.6), (7.7) and (7.8), where MPA is $C_3H_6O_2S$, the O-acylisourea intermediate is $C_{11}H_{23}N_3O_2S$, the isourea derivative is $C_8H_{19}N_3O$ and the NHS-ester (N-succinimidyl 3-mercaptopropionate) is $C_7H_9NO_4S$.

The exception is the 4°C isotherm this does not indicate the desired early peak of the other data sets and seems to suggest that two competing structures are not formed and that some of the reactions are suppressed at low temperatures.

$$C_8H_{17}N_3 + C_3H_6O_2S \rightarrow C_{11}H_{23}N_3O_2S \quad (7.5)$$

$$C_{11}H_{23}N_3O_2S + H_2O \rightarrow C_8H_{19}N_3O + C_3H_6O_2S \quad (7.6)$$

$$C_4H_5NO_3 + C_{11}H_{23}N_3O_2S \rightarrow C_7H_9NO_4S + C_8H_{19}N_3O \quad (7.7)$$

$$C_7H_9NO_4S + H_2O \rightarrow C_3H_6O_2S + C_4H_5NO_3 \quad (7.8)$$

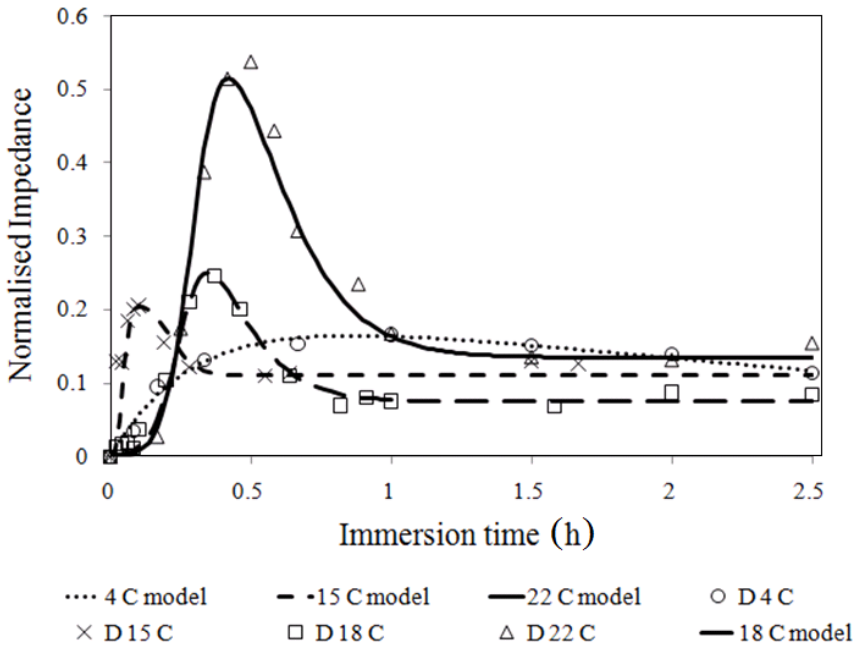

Figure 7.8: Normalised raw EIS data at temperatures less than the Gyepi-Garbrah critical temperature (Tc) (Gyepi-Garbrah and Šilerová, 2001) of the MPA monolayer, discrete points show the actual experimental data. The lines show the calculated impedance from the fitted Henderson-Kisliuk model.

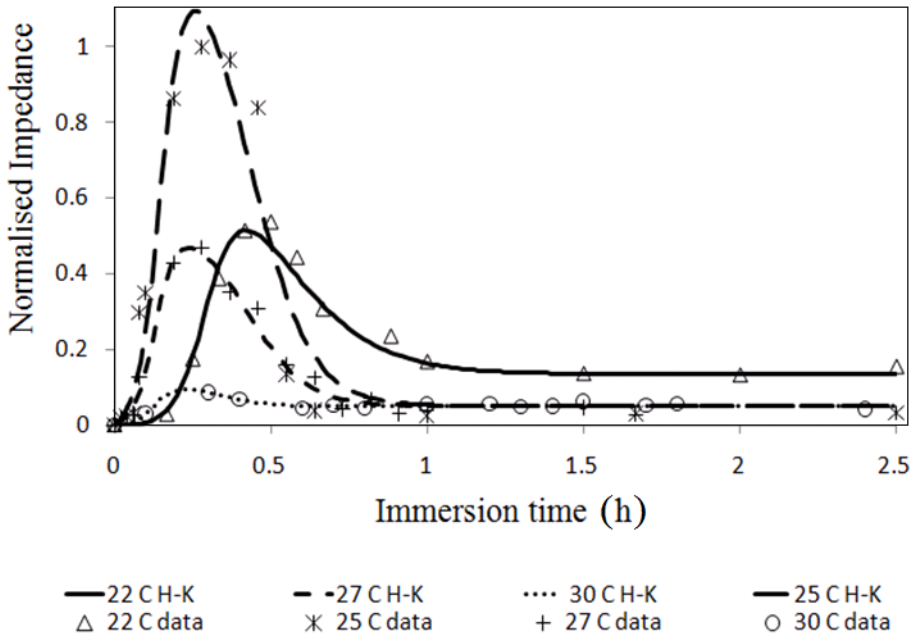

Figure 7.9: Raw EIS data at temperatures at temperatures greater than the Gyepi-Garbrah critical temperature (Tc) (Gyepi-Garbrah and Šilerová, 2001) of the MPA monolayer. The isotherm at 22 °C is also included for comparison. The discrete points show the actual experimental data. The lines show the calculated impedance from the fitted Henderson-Kisliuk model.

7.5 Modelling the activation process through the impedance isotherms

7.5.1 Background

The experimental data suggests that the EDC/NHS activation process takes place in two stages, is influenced by the presence of adsorbed species on the surface and that two different structures form sequentially on the surface of the substrate. This is supported by the work of Gooding and Hibbert, (1999), It is also surmised that the activation takes place as the result of a number of competing reactions. This cannot be modelled by classic adsorption isotherms (e.g. Langmuir, Random Sequential Adsorption model and Kisliuk) alone. Therefore, a model is needed that can overcome the limitations of the existing models.

One way forward has been used previously in chapter 6 to model the adsorption of MPA onto gold (See section 6.5). In summary the PTCS model was developed by combining an adsorption model such as Langmuir or Kisliuk with a mass balance to account for the relative amounts of different structures on the surface at any time (t) For this process a combination of PTCS with Kisliuk (See equation (7.9), PTCS–Kisliuk model) could be used to account for the different structures on the surface and

through the Kisliuk constants the influence of the adsorbed species on the adsorption rate.

$$z_t = \frac{1-e^{-R_1'(1+k_{E1})t}}{1+k_{E1}e^{-R_1'(1+k_{E1})t}} \cdot \left[\varphi_1 \cdot \left(1 - \frac{1-e^{-R_2'(1+k_{E2})t}}{1+k_{E2}e^{-R_2'(1+k_{E2})t}} \right) + \varphi_2 \cdot \frac{1-e^{-R_2'(1+k_{E2})t}}{1+k_{E2}e^{-R_2'(1+k_{E2})t}} \right] \qquad (7.9)$$

The PTCS–Kisliuk equates the measured normalized impedance response (z_t) to a number of fitted variables where: R_n‘ are the relative rate constants, k_{En} are the relative sticking coefficients and φ_n, the signal weighting constants, Subscript n is equal to 1 or 2 (indicating a variable relating to one of two structures formed).

This model is nevertheless limited because it accounts for the influence of the adsorbed species on the process through the use of crude sticking factors. The sticking factors have little theoretical basis and are not solely dependent on the concentration of adsorbed species on the surface. Therefore, it is difficult to draw any conclusions about the relative rate of island growth versus random adsorption mechanisms for activation or the effects of competing processes from the fitted results.

To overcome these limitations and limitations of other extant adsorption models, the PTCS model was combined with the new adsorption model PIF described in chapter 3 to give the PTCS-PIF adsorption isotherm. The PTCS-PIF adsorption isotherm is stated in equation (7.10)) and was created specifically to model the activation process in this chapter. Both the PTCS-Kisliuk and the PTCS-PIF models were fitted to the measured experimental data as the PTCS-Kisliuk gives a benchmark of the best current available model against which the new PTCS-PIF model can be rated.

$$z_t = \frac{k_{R1}-k_{R1}e^{-(k_{R1}+k_{I1})t}}{k_{R1}+k_{I1}e^{-(k_{R1}+k_{I1})t}} \left(\quad {}_1\left(1 - \frac{k_{R2}-k_{R2}e^{-(k_{R2}+k_{I2})t}}{k_{R2}+k_{I2}e^{-(k_{R2}+k_{I2})t}} \right) + \quad {}_2\left(\frac{k_{R2}-k_{R2}e^{-(k_{R2}+k_{I2})t}}{k_{R2}+k_{I2}e^{-(k_{R2}+k_{I2})t}} \right) \right) \qquad (7.10)$$

7.5.2. Results of fitting the PTCS-Kisliuk model to the isotherms

The objective function for the PTCS-Kisliuk model as defined in equation (3.46), was fitted to the experimental data, minimized using the Newton method contained within Microsoft Solver routine and the fitted parameters set as R_1‘, R_2‘, k_{E1} and k_{E2}. The

fitted parameters and the goodness of fit to the experimental data are shown in Table A2.1 for each temperature data set.

The fitted parameters are shown below in Figure 7.10 as functions of temperature and the numerical values along with the statistical analysis of the results are recorded in Appendix 2 for the 27 ^{o}C isotherm. It can be seen that the model provides a good fit to the data obtained for each isotherm measured.

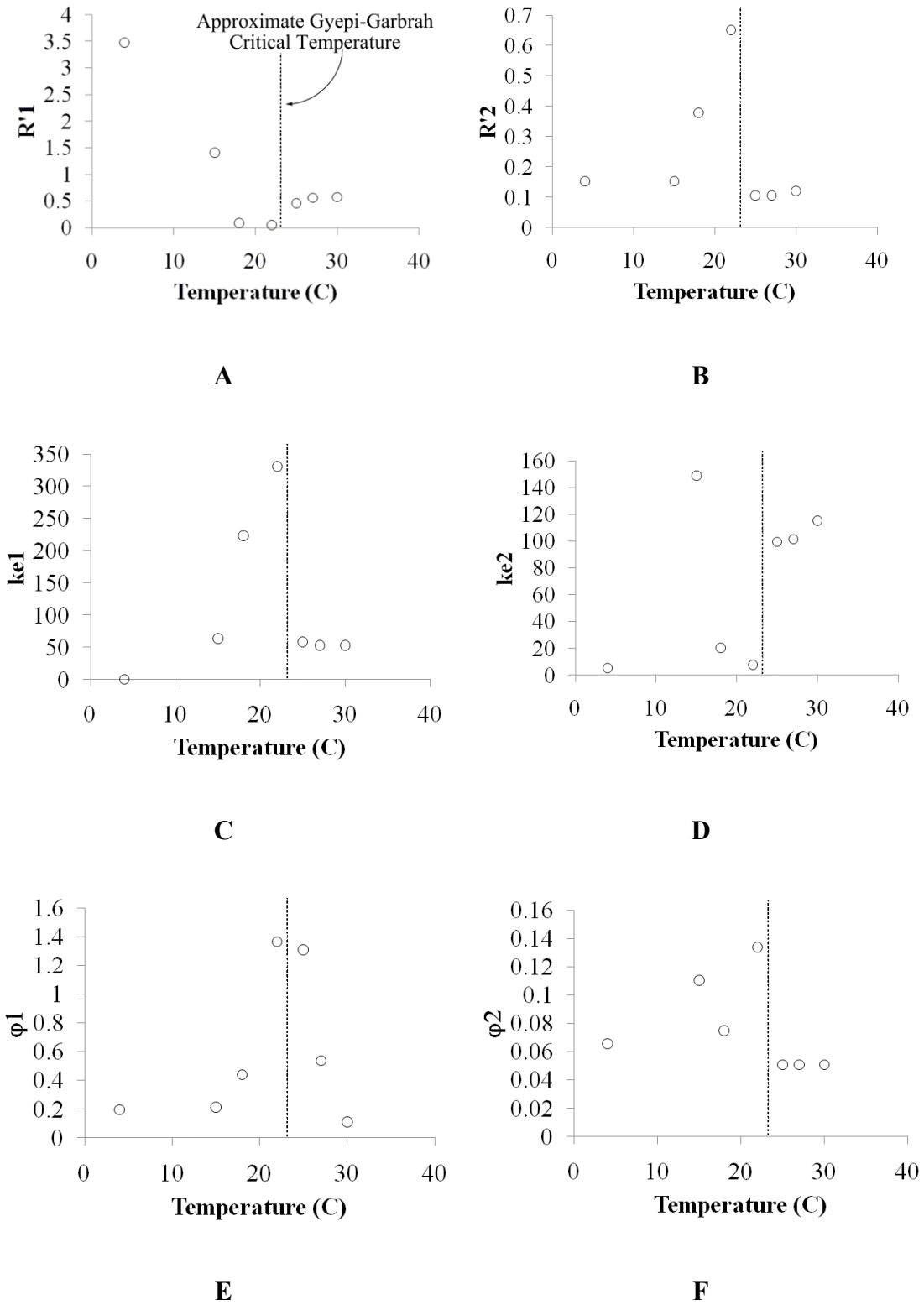

Figure 7.10: Graphs showing the trends exhibited by the fitted constants of the PTCS-Kisliuk model as a function of temperature. The approximate Gyepi-Garbrah Critical Temperature of the MPA is shown to illustrate how constants respond to transition at this temperature.

7.5.3 Results of fitting the PTCS-PIF model to the isotherms

The PTCS-PIF model was also fitted to the experimental data using the least squares method as defined by the objective function given as equation (3.47).

The fitted isotherm model is shown in Figure A2.1 and Figure A2.2. Fitted parameters are shown below in Figure 7.11 as functions of temperature and recorded with the statistical analysis of the goodness of fit for the 27 ^{o}C isotherm, in Appendix 2.

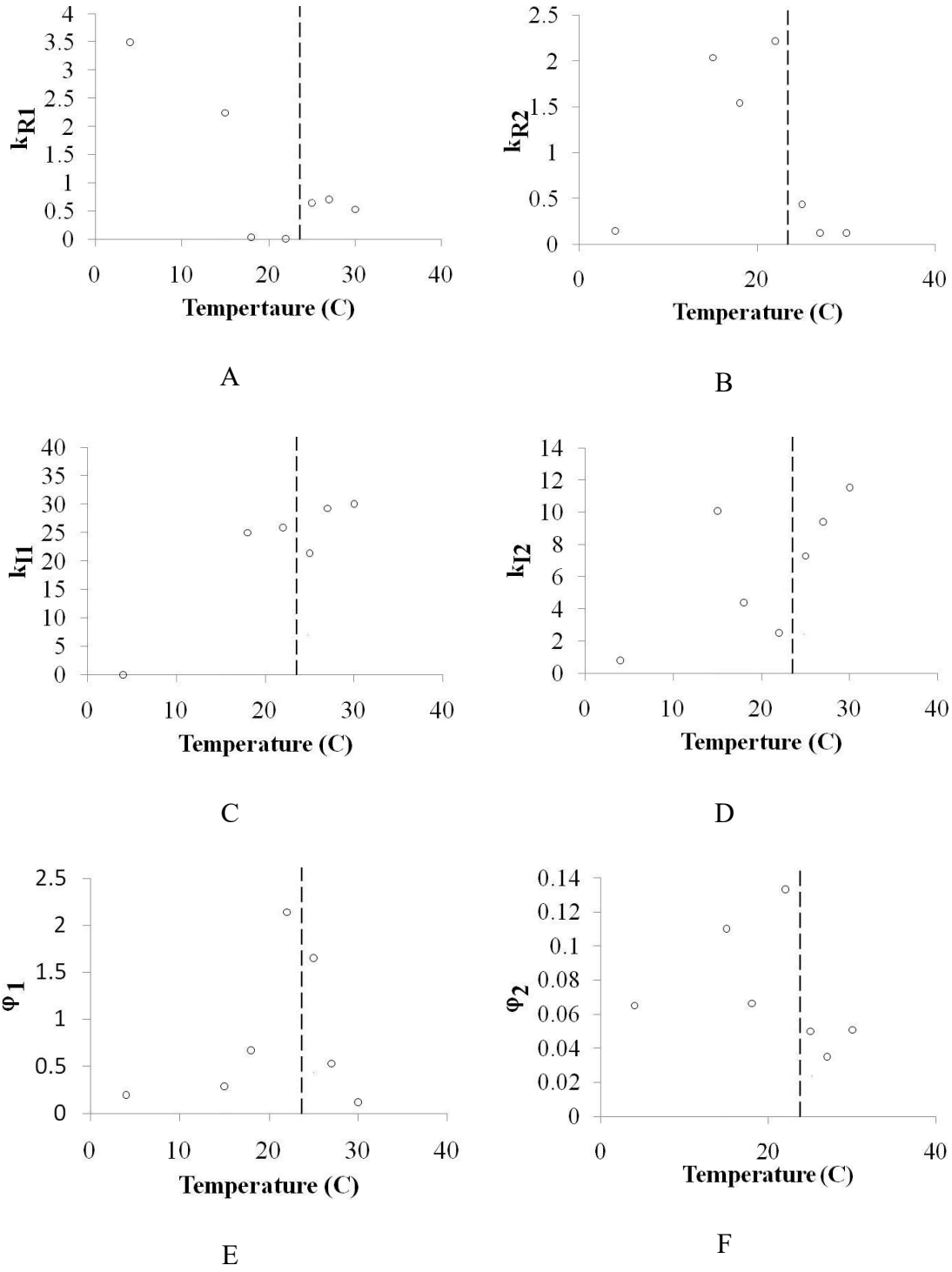

Figure 7.11: Graphs showing the trends exhibited by the fitted constants of the PTCS-PIF model as a function of temperature. The approximate Gyepi-Garbrah Critical Temperature of the MPA is shown to illustrate how constants respond to transition at this temperature.

7.5.4. Discussion of the fitted parameters for both adsorption models and the kinetic information that can be deduced from the fitted values

The results of the fitting exercise will be discussed as three subsets. The 4° C isotherm will be treated on its own because it displays a unique shape (See Figure 7.8). The second subset is formed by isotherms at or below the Gyepi-Garbrah temperature for the MPA layer. This is a natural break in the data where the properties of the underlying MPA are known to change and will influence the activation process. The final subset is formed by the isotherms measured above the Gyepi-Garbrah temperature.

7.5.4.1 Results for model fits of the 4° C isotherm.

The rate constant R_1 for the PTCS-Kisliuk model and the corresponding k_{R1} constant for the PTCS-PIF model are numerically large when compared with the fitted values at higher temperatures. This suggests that the dominant process at this temperature is the formation of O-acylisourea via random island seeding. This is consistent with extant kinetic knowledge, which states that O-acylisourea hydrolysis is low at low temperature (Hermanson, 2008). The random adsorption proceeds by the reaction given as equation (7.5) which is known to be exothermic (Chang and Douglas, 2007) and hence favoured at low temperatures. The competing hydrolysis reaction equation (7.6) is suppressed because the collision enthalpy of the species involved is insufficient for the hydrolysis reaction to occur. The recorded values of k_{E1} and k'_{I1} are both zero suggesting the absorbed species have no affect on the rate of formation of O-acylisourea and that adsorption is totally random for this process.

Similar comments can be made about the substitution mechanism for the replacement of O-acylisourea with NHS-ester. However the PTCS-Kisliuk model R_2‘ value for the 4 ^{o}C dataset is much smaller than the R_1‘ and similarly the k_{R2} value is much smaller than the k_{R1} value for the PTCS-PIF model (see Figure 7.10 and Figure 7.11). Taken together these results indicate that NHS-ester forms at a much slower rate than O-acylisourea. The much slower rate of formation is attributed to the amount of activation energy required for the formation of each species. The activation energy required for formation of NHS-ester equation (7.7) is known to be much greater than that required for the formation of O-acylisourea equation (7.5) and the reaction to form NHS-ester is therefore suppressed at low temperatures (Glaser et al, 1999).

From the PTCS-PIF model a value of 0.792 s^{-1} mol^{-1} is recorded for k_{I2} indicating that a small amount of the NHS-ester is formed by island growth.

It can be concluded that the low temperature has suppressed layer formation by island growth and some of the exothermic reactions resulting in a process governed solely by random absorption to the surface. This is consistent with the Langmuir behaviour displayed by the 4 ^{o}C isotherm shown in Figure 7.8.

7.5.4.2 Immersion data collected between 4 ^{o}C and the Gyepi-Garbrah Critical Temperature

The fitted values of R_1‘ and k_{R1} are observed to decrease as the temperature rises (see figure 7.10 and figure 7.11) and indicate that the net rate of random formation of O-acylisourea decreases with temperature. The rate of random formation is known to increase with temperature therefore it is implied that the hydrolysis reaction of O-acylisourea (equation (7.6)) becomes more significant as temperature increases. This is as expected as the activation energy of this reaction is more easily attained as higher temperatures.

The fitted values of k'_{I1} increase with temperature and categorically indicate that the rate O-acylisourea formation is increasingly controlled by the rate of island growth in stage 2. This conclusion is supported by the equivalent Kisliuk parameter though not conclusively. Similar effects are observed for k_{E1} values from the PTCS- Kisliuk fit but the k_{E1} values are observed to increase at a much faster rate. k_{E1} increases at a faster rate because it depends on both island growth and random adsorption. Therefore though an increase k_{E1} suggests that island growth may influence O-acylisourea formation, it is impossible to determine from the Kisliuk parameter how much of the growth is due to island growth.

As the temperature rises the fitted values of R_2‘and k_{R2} are observed to increase. These trends indicate that the formation of NHS-ester by random adsorption is favoured at higher temperatures. It should be noted that NHS-ester does not hydrolyse as readily as O-acylisourea (Huang et al, 2000) and although the rate of hydrolysis of

NHS-ester is also expected to increase with temperature it has little effect on the process up to 22°C.

The fitted values of k'_{I2} are observed to be significantly lower than k'_{I1}. This indicates that the autocatalytic effect of adsorbed NHS-ester on the adsorption of more NHS-ester is insufficient to overcome the activation energy barrier needed for the reaction to proceed. The NHS-ester process is therefore reliant on random adsorption and as a consequence is much slower that the formation of O-acylisourea process. Further the k'_{I2} are observed to rise to a peak at 15° C and then fall back to lower values. This implies that the island growth process for NHS-ester is complex over this temperature range and that a number of competing effects may be influencing the process.

The fitted values of φ_2 increases with temperature indicating the final yield of NHS-ester on the surface decreases with temperature up to the MPA Gyepi-Garbrah temperature

7.5.4.3 Immersion data collected above the MPA Gyepi-Garbrah critical temperature, at 25, 27 and 30 ^{o}C

The trends observed for the fitted parameters are observed to change markedly for these three data sets. This suggests that either the increase in temperature or the increase in the disorder in the adsorbed MPA monolayer or a combination of both are significantly affecting the activation process

The results obtained from the fitted PTCS-PIF model are particularly useful when trying to discern if the temperature is the main factor affecting the activation process. The fitted values of k_{R1} and k_{R2} are observed to be an order of magnitude smaller than the values for k_{I1} and k_{I2}. This indicates that the rates of formation of O-acylisourea and NHS-ester are dominated by island growth. Further the value of k_{I2} is seen to increase markedly above the Gyepi-Garbarh temperature. This suggests the activation energy barriers to formation of NHS-ester by island growth experienced at lower temperatures have been overcome. As a consequence the rate of formation of NHS-ester has increased to match that of O acylisourea. This is reflected in the values of φ_1 which reduce markedly indicating the peak concentrations of O-acylisourea are

smaller and that the O-acylisourea is being consumed much more quickly by the NHS-ester reaction. Given that the k_{I1} values remain approximately constant and the k_{I2} values are seen to increase markedly it seems that the increased disorder in the underlying monolayer is having little effect on the activation process.

The final values of φ_2 have decreased above the Gyepi-Garbrah temperature and settled at a near constant value. This implies that a more homogeneous activation layer is achieved at a higher temperature as a consequence of layer formation by island growth which produces a more uniform structure. Further increases in temperature are unlikely to improve the activation as island growth already dominates.

7.6 Summary

EDC/NHS activation has been studied via Contact Angle measurement, FTIR profiling and fluorescent microscopy at 22 ^{o}C. These techniques suggested that activation of the carboxylic layer occurred by more than one process and that the presence of macroscopic islands (>100 micron diameter) of activated surface indicated that the presence of adsorbed activation species on the surface influenced the adsorption processes.

The activation process was then studied in more detail using EIS to look at the bulk properties of the activated layer during activation and the influence of temperature. A systematic study of the activation process was carried out by measuring seven different isotherms from 4 ^{o}C to 30 ^{o}C. The measurements clearly confirmed that the activation process proceeded in two stages and that two structures could be present on the surface. They also suggested that the relative rates of growth of the structures could be controlled by manipulation of the temperature to optimize the activated layer.

Determination of the optimum conditions for activation required an understanding of the kinetics and mechanisms of the processes taking place. To acquire this knowledge a new mathematical model (PTCS-PIF) that accounts for the individual contributions

to activation by both random and island growth processes and the effects of surface coverage by two sequential structures was developed.

The experimental data was fitted with the PTCS-PIF adsorption model and PTCS-Kisliuk model to check that the new model was at least as good as the extant methods. Both models were shown to give similar fits easily within the uncertainty of the measured experimental data.

Changes in the dielectric properties of the monolayer undergoing activation and deductions from the models allowed the following deductions to be made:

1) At very low temperatures (less than 4 °C) adsorption of both EDC and NHS is mainly by random adsorption.
2) At temperatures between 4°C and the Gyepi-Garbrah temperature for the MPA (~24 °C) EDC adsorption is controlled by island growth and NHS is a much slower process controlled by random adsorption.
3) At temperatures above the Gyepi-Garbrah temperature for the MPA both adsorption processes are controlled by island growth.
4) A more uniform activation is achieved by island growth therefore the optimum conditions for activation are at or above the Gyepi-Garbrah temperature for the MPA formation.

Chapter 8:- Modelling and optimising the adsorption of Streptavidin on an activated MPA monolayer

8.1 Introduction

The next step in the biosensor‘s construction is to attach a monolayer consisting of a molecule that is capable of binding exclusively to biotin with a high affinity. This molecule is attached directly to the activated MPA layer and is a critical component in immobilising biotinylated antibody to the surface of a biosensor via the conjugate molecule‘s biotin head group.

Two molecules commonly used to bind with biotin are Avidin and Streptavidin protein macromolecules. In spite of the fact that the interactions between Avidin or Streptavidin and biotin are non-covalent, a very strong avidity exists between Avidin or Streptavidin and biotin, where the dissociation constant between the compounds is approximately 1 fM (Hytönen et al, 2005). Hence, biolayer durability is not compromised by employing the Avidin/Streptavidin and biotin method of coupling over direct coupling of the antibody to the modified mercaptocarboxylic acid. Indeed, the Streptavidin-biotin interaction will result in increased monolayer stability, sensitivity and allow the biosensors to be stored for months without loss of signal reproducibility (Diaz-Gonzalez et al, 2005).

A Streptavidin layer was therefore thought to be the best choice for the next stage of sensor construction. Avidin was ruled out for this stage because it facilitates the hydrolysis of the covalent bond linking Biotin to Biotinylated IgG, the next stage of the process.

Streptavidin growth rates for the formation of this monolayer are known to be dependent on experimental conditions such as pH, temperature, Streptavidin solution concentration, ionic strength and maybe most importantly immersion time. This process has been widely used to improve sensor sensitivity but each extant study uses an arbitrary immersion time based on practical experience (Cui et al, 2003, Ding et al, 2005, Sugawara et al, 2002). This implies that a systematic study of this process is required to look at the dependence of the layer growth rate on immersion time. This chapter addresses this deficiency and attempts to model the results. The developed

model allows the optimum immersion time to be fixed and provides a way forward for future modelling of like systems.

8.2 Experimental work

A series of two independent sets of measurements were carried out to investigate the dependence of the formation mechanism for the Streptavidin layer on time of immersion. All measurements were carried out at a constant temperature of 21 ˚C.

The principle measurements were made using Electrochemical Impedance Spectroscopy (EIS) and the back-up measurements were made using Atomic Force Microscopy (AFM).

8.2.1 AFM measurements

Qualitative assessment of the streptavidin layer was carried out using Atomic Force Microscopy (AFM). The studies were carried out on a pair of borosilicate glass slides coated with Au(111). The glass slides were cleaned by immersion in piranha solution, 75 % v/v H_2SO_4 (Fluka) and 25 % v/v H_2O_2 (Fisher Scientific), before being rinsed firstly in DI water and then subsequently in ethanol, to remove inorganic and organic contaminants from the slides prior to MPA immobilization. An activated MPA layer was attached to the glass slides in accordance with the procedures out lined in Chapters 6 and 7. One of the slides was subsequently immersed in Streptavidin solution for 2h to produce the Streptavidin layer. Streptavidin (Prozyme) was provided by Immunodiagnostic systems Ltd (IDS Ltd.) and diluted to a concentration of 1.5mg/ml in (PBS, pH=7.4) to provide the required coating solution. Both modified gold coated glass slides were then stored in PBS solution, whilst awaiting measurement, before they were rinsed in purified water (15MΩ) and dried using an air gun. The surfaces of both samples were then profiled using a Nano-R™AFM (Pacific nanotechnology, Santa Clara, CA) in close contact mode in air.

8.2.2 Electrochemical measurements

The quantitative measurements were made using Electrochemical Impedance Spectroscopy (EIS). The measurements were made using a conventional three electrode arrangement. Each of the three electrodes was prepared in accordance with the cleaning procedures described in Chapter 5 and coated with an activated MPA layer in accordance with the procedures specified in Chapters 6 and 7. Following the SAM activation procedure the working electrodes were thoroughly rinsed in DI water and immersed in Streptavidin solution for different time periods. After the set time period for a given electrode had elapsed it was removed from the coating solution and thoroughly rinsed to remove Streptavidin molecules not covalently bound to the surface.

Each immersion period test was performed in triplicate with an Autolab potentiostat/galvanostat in conjunction with Frequency Response Analyser (FRA) and General Purpose Electrochemical System (GPES) software (Eco Chemie B.V.), for EIS and Cyclic Voltammetry (CV) measurements respectively. The Ag/AgCl reference electrode, platinum wire counter electrode and gold working electrode (MF-2014) were all purchased from BASi instruments Inc and all electrochemical measurements were performed in PBS buffer solution.

For EIS, a 0.1mV amplitude sine wave was applied to the working electrode in the tested frequency range of 0.1Hz to 1MHz. The working electrode was polarized at a potential of +0.25V/Ag(AgCl) during measurements, which was shown via CV to be the oxidation potential of the redox indicator. EIS measurements were performed after the working electrode had been cleaned, after it had been immersed in EDC/NHS solution and after Streptavidin immersion.

8.3 Results

8.3.1 AFM characterisation of the Streptavidin monolayer.

Figure 8.1(A) shows the surface after immersion in Streptavidin for two hours. The surface is observed to consist of a series of small rounded peaks which are 5 nm in height. When compared with the untreated surface (shown in Figure 8.1(B)) the height of these peaks corresponds to the size of Streptavidin molecules determined in previous AFM studies (Neish et al, 2002) and is indicative that a Streptavidin monolayer was formed over the surface of the substrate.

Each of the rounded peaks has a diameter much greater than 5 nm suggesting that they consist of several Streptavidin molecules bound adjacent to each other on the gold substrate. The Streptavidin molecules constituting each rounded peak are densely packed hence the pores that allow the individual Streptavidin molecules to be distinguished within a peak, are too fine to be profiled with the close contact AFM probe. This seems to imply that Streptavidin adsorption is influenced by species already present on the surface and that these peaks are formed as a result of an island growth mechanism. The low lying features represent holes in the Streptavidin monolayer, where it was possible for the AFM profiling tip to penetrate through to the MPA layer. The holes represent gaps between the Streptavidin islands which are too small to permit further adsorption of Streptavidin to the activated MPA monolayer.

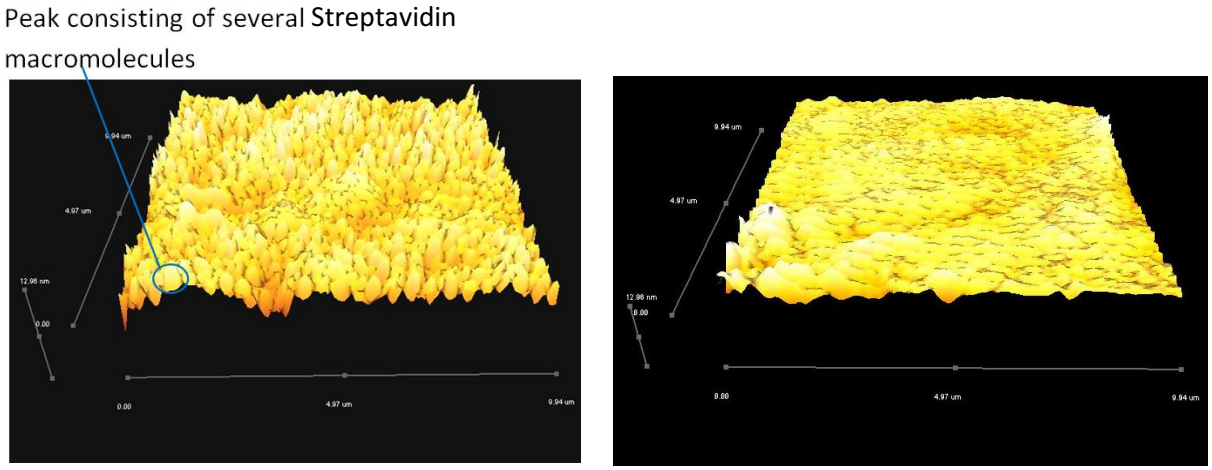

A B

Figure 8.1: Atomic force microscope (AFM) pictures of the streptavidin layer (a) An AFM image of a Streptavidin monolayer on a modified gold slide after an immersion time of 2h (b) An AFM image of an activated SAM on a gold coated glass slide substrate(for reference).

8.3.2 EIS characterisation of the Streptavidin layer

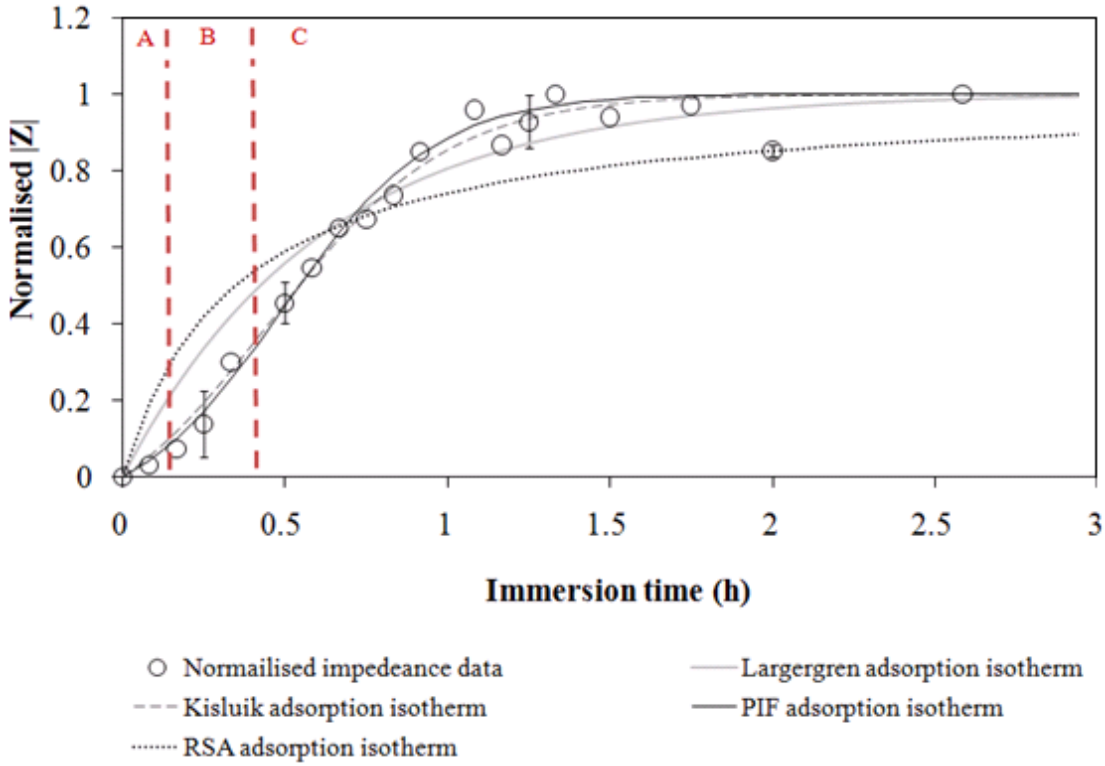

Figure 8.2: The fits exhibited by the PIF, Kisliuk, Langmuir and RSA adsorption models with normalised experimental total impedance data, at 0.1Hz, which were measured from working electrodes that had been immersed in streptavidin solution for various periods. The three stages of growth are also outlined where: A is the 1st stage of formation, where random adsorption is dominant; B is the 2nd stage of formation, where crystal growth is dominant, and C is the 3rd stage of formation which is controlled by the occupation of potential formation sites.

Figure 8.2 shows the normalized impedance data obtained from the EIS measurement for the isothermal measurements at 21˚C and the complex impedance profile of the cleaned gold working electrode prior to modification. The curves are the results of the fitted adsorption models.

The measured results produce a curve which can be divided in to three distinct sections shown as A, B and C in Figure 8.2. These three sections suggest that layer growth takes place in three different stages where different processes are involved.

In section A the substrate surface is initially free of Streptavidin and the only form of adsorption that exists is that of crystal seeding (random Streptavidin adsorption). This type of adsorption takes place at a location on the substrate that is remote from any other adsorbed streptavidin molecules. At such a location, the only interactions encouraging growth are those that are exerted on the streptavidin molecule by the solution and the substrate surface. These interactions are afforded the term ~~–F~~s" in Figure 8.3 and cause layer formation to occur slowly. This method of adsorption dominates for the first 5 minutes of immersion

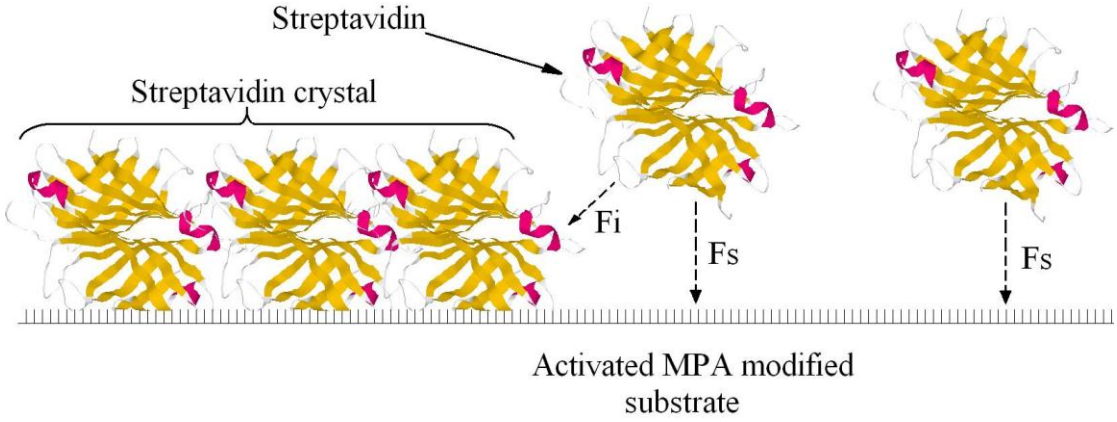

Figure 8.3: Kinetics of Streptavidin adsorption, using PIF model principles, where: Fs encompasses all forces encouraging random adsorption of Streptavidin to the substrate and Fi represents the additional interactions that only exist around Streptavidin crystals present on the substrate surface.

In section B Streptavidin starts to form around molecules of Streptavidin which have previously coalesced on the substrate surface, homogeneous crystals form and the crystal circumference increases encouraging further adsorption via crystal growth. This is represented by the increase in the rate of Streptavidin adsorption to the surface over the immersion period 0.083 hrs to 0.33 hrs (see Figure 8.2). This behaviour was first observed by Shimoni and Glusker (1995) for protein adsorption to a surface where complex amino acid interactions between protein molecules on the surface and molecules being adsorbed were recorded and referred to as ~~–e~~rystal growth." The ~~–e~~rystal growth" adsorption mechanism is thought to be analogous to the ~~–i~~sland formation mechanism," described in earlier chapters.

In Section C after an immersion period of 0.33 hrs, Streptavidin on the surface occupies most binding sites and the opportunities for further adsorption are controlled by the availability of sites. Therefore the rate of adsorption reduces in line with the availability of suitable sites. It is observed that the normalised impedance has reached a constant value after 2 hours which implies that the process is at steady state and no further changes occur in the monolayer. The optimum immersion time to produce a streptavidin monolayer is therefore deduced as being 2 hours.

8.3.2.1 Equivalent Circuit analysis of the surface properties

The equivalent circuit used to describe this process is shown in Figure 8.4 and the complex impedance plot for the equivalent circuit model is given in Figure 8.5 for the fitted constants given in Table 8.1.

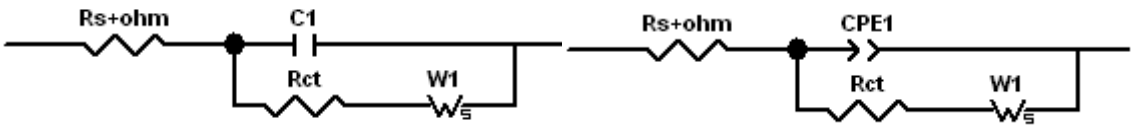

A B

Figure 8.4: (A) The equivalent circuit used to simulate the behaviour of the MPA baseline impedance signal and the signals yielded from a Streptavidin monolayer after an immersion time of 0.5 h and 2.6 h; (B) The equivalent circuit used to simulate the behaviour of the impedance signal yielded from a Streptavidin monolayer after an immersion 1.25 h

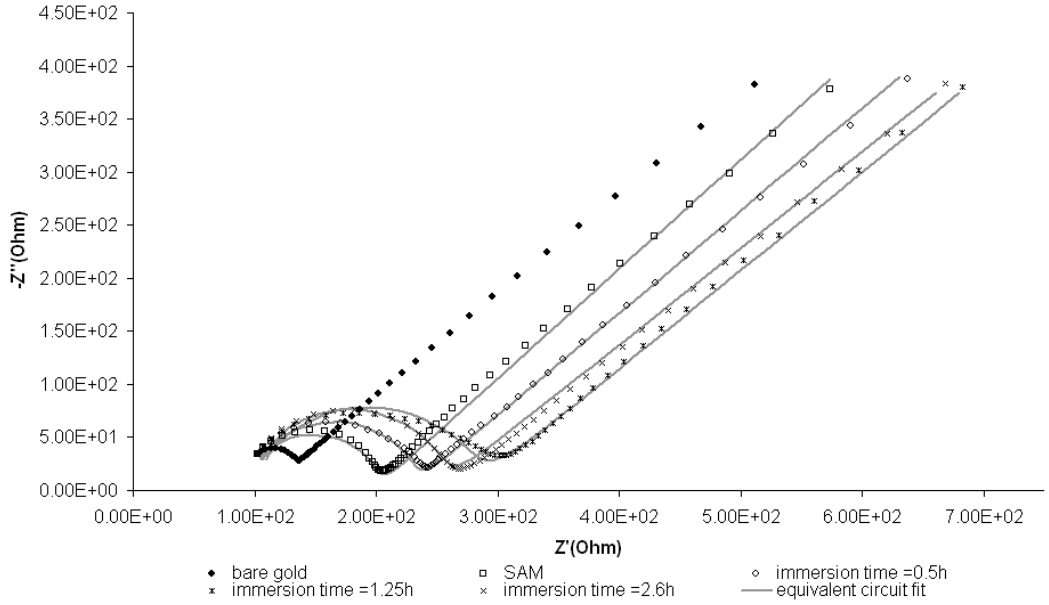

Figure 8.5: A complex impedance plot showing the variation in imaginary (Z‘‘) and real (Z‘) impedance brought about by the presence of streptavidin monolayers on a modified work electrode, as a function of immersion time in streptavidin solution.

It is possible to deduce a number of characteristic from the trends in the constants shown in Table 8.1 and from the impedance plot shown as Figure 8.5. The ohmic resistance and the uncompensated solution resistance are fixed properties of the cell hence Rs+Ohm are constant. C1 is seen to remain constant demonstrating that the Streptavidin layer cannot be likened to a capacitor.

Table 8.1: Equivalent circuit element values, used in Figure 8.4 to model complex impedance data, shown in Figure 8.5, for Streptavidin monolayers formed on activated working electrodes over various Streptavidin solution immersion periods. Constants were determined via ZView2 (Scribner Associates, Inc).

	Equivalent Circuit Element							
Immersion time	**Rs+ohm**	**C1**	**CPE1-T**	**CPE1-P**	**Rct**	**W1-R**	**W1-T**	**W1-P**
MPA baseline signal	100	5.25×10^{-7}	-	-	99.7	1.80×10^{5}	1.28×10^{5}	0.514
0.5 h	100	5.27×10^{-7}	-	-	127	1.87×10^{5}	2.31×10^{5}	0.489
1.25 h	100	-	1.38×10^{-7}	0.91	178	9604	638	0.477
2.6 h	100	5.25×10^{-7}	-	-	150	4.82×10^{5}	2.787×10^{6}	0.471

As the Streptavidin layer forms Rct, is observed to increase. This indicates that redox ion species pass through the Streptavidin layer and the Streptavidin layer provides resistance to mass transfer, thereby reducing charge transfer current and increasing charge transfer resistance. This is supported by the W1-P trend that shows a decrease as monolayer coverage increases demonstrating that the presence of Streptavidin causes total impedance to have a greater dependency on real impedance (Z‘), which is dictated by redox ion diffusion.

W1-R and W1-T, are seen to increase as the Streptavidin layer is formed. These constants depend on the diffusion coefficient of the medium present above the MPA interface and redox ion concentration at the MPA interface (equation (2.8) and (2.9)). They suggest that a build-up of redox ions is occurring along the MPA/Streptavidin boundary as the Streptavidin layer forms inhibiting the mass transfer of redox ions to/from the MPA Layer surface as the permeability of the Streptavidin layer decreases.

The EIS spectrum collected after an immersion time of 1.25 hrs was of greater impedance than the EIS spectrum collected after 2.6 hrs and could not be modelled accurately using the equivalent circuit shown in Figure 8.4a, necessitating the construction of a second equivalent circuit (Figure 8.4b) to overcome the non-ideal capacitive behaviour that was evident in the data. Hence, values of Rct, W1-R and W1-T differ considerably from the general trend whilst W1-P is in keeping with the general trend.

Such a change in monolayer dielectric behaviour is a clear indication of a different crystal structure, which is consistent with extant literature (Shimoni and Glusker, 1995). This unique structure is present just after the formation of a saturated layer when the crystals have merged but are orientated in different directions, resulting in the formation of an inhomogeneous layer.

On further immersion, the crystals realign to form a homogenous, saturated monolayer. This is clearly shown in the EIS spectrum collected for the 2.6 hrs immersion dataset, which can be modelled using the equivalent circuit shown in Figure 8.4a, and in the equivalent circuit component values, which display a trend consistent with those of the ―MPA baseline" dataset and the ―0.5 hrs" dataset (Table 8.1). This observation is also consistent with extant literature (Shimoni and Glusker, 1995).

8.4 Modelling of the Streptavidin layer formation process.

8.4.1 Introduction

The layer formation process for this stage is basically an adsorption process and a number of different existing models could be applied. The most popular mathematical model used to approximate the adsorption of biological macromolecules to a planar surface is that of the Random Sequential Adsorption, RSA, model (Feder, 1980). However, there are a number of other adsorption isotherm models which have the potential to provide a more successful approximation to experimental data. These have been outlined in Chapter 3.2 and include: Lagargren adsorption kinetics, Kisliuk adsorption and the PIF adsorption models.

The RSA and Lagargren models share a common limitation in that neither model accounts for the interactions that exist between adsorbed molecules and adsorbate molecules being adsorbed from the bulk. Such interactions are negligible in some adsorption systems however Shimoni and Glusker (1995) demonstrated that protein crystals initially form small rafts of crystalline protein, surrounded either by bare activated substrate areas or by other crystals, oriented in different directions. The small crystals were then found to grow or coalesce with each other and anneal to form large uniform and identically oriented crystals, which infers that interprotein molecular interactions are a significant factor when considering Streptavidin protein monolayer formation as a function of immersion time.

8.4.2 Modelling procedures

The RSA, Langmuir, Kisliuk and PIF adsorption models were all fitted to the normalised experimental impedance data to obtain the parameters for each model. This was done using the least squares method and the appropriate objective function for each model reported in Chapter 3.2. The objective functions were minimized using Newton's method contained within Microsoft Solver routine. The parameters that gave the best fit to the experimental data are summarised in Table 8.2.

Table 8.2: Proposed island formation, Kisliuk and Langmuir adsorption model constants employed to model the curves shown in Figure 8.2 with respective chi squared values (χ^2).

Kisliuk model			**Largergren model**		**RSA model**		**PIF model**		
R"	**k_E**	**χ^2**	**R**	**χ^2**	**B**	**χ^2**	**k_R**	**k"$_I$**	**χ^2**
0.5939	5.058	0.1001	1.632	0.4273	0.3493	0.8614	0.4568	3.844	0.0675

All models were demonstrated to provide a good approximation to the experimental data as every chi squared value returned was substantially less than 19 (the number of data points used). The statistical analysis revealed that the models could be ranked as follows PIF model, Kisliuk model, Largergren model and RSA model, where the PIF model gave the best fit. The much better fits obtained for the PIF and the Kisliuk

models confirms that adsorbed Streptavidin is influencing the adsorption process and is consistent with the evidence from the AFM study and the extant literature.

8.5 Summary

Streptavidin monolayer formation has been studied on an activated MPA monolayer and has been characterised and quantified using Electrochemical Impedance Spectroscopy (EIS) and Atomic Force Microscopy (AFM).

Three distinct stages of formation were identified, initially random adsorption is the dominant process, then crystal growth becomes evident where adsorption is influenced by adsorbed Streptavidin and finally the adsorption rate decreases as the modified surface approaches saturation.

Equivalent circuit analysis of EIS data for Streptavidin layer formation identified that the layer is permeable to redox ions and that it made little contribution to the capacitive properties of the biolayer.

The EIS measurements were modelled using the RSA, Largergren, Kisliuk and PIF isotherm models and the statistical analysis of the fitted models revealed that the PIF isotherm provided the best approximation to experimental data. The Largergren and RSA models have been shown to be unsuitable as they were unable to model the hydrogen bond interactions that are thought to be a major factor in Streptavidin monolayer formation.

The optimum immersion period has been identified as 2 hours to yield the best possible monolayer onto which b-IgG will be immobilised during the final stage of immunosensor manufacture.

Chapter 9: Biotinylated IgG (b-IgG) monolayer optimisation.

9.1 Introduction

The last stage of the biosensor manufacturing process is to make the detector compound selective by forcing it to respond to a given analyte in a solution. This can be done by the formation of a Biotinylated IgG (b-IgG) monolayer on the surface of the detector that binds only to the analyte of interest.

This study was conceived specifically to look at the relationship between biotinylated antibody immobilization times and layer formation, including macroscopic structural properties. It does not look at the temperature and concentration effects that may also affect immobilization rates and monolayer structure. The extant literature indicates that a wide variation of biotinylated antibody immobilization times have been used where the optimum time has been arrived at by experimentation (Ouerghi et al, 2002, Darain et al, 2003, Hays et al, 2006). There is therefore scope to produce a systematic experimental study and appropriate mathematical model to describe the immobilization process that can be expanded in the future to account for temperature and composition effects.

9.2 Experimental work

A prerequisite of attempting to model this process is a comprehensive systematic experimental study of the surface coverage of the IgG with time. No systematic study of these bulk properties for this process exists therefore it was decided to perform a systematic experimental study of the immobilisation rate of the biotinylated layer with immersion time at a fixed temperature and analyte concentration. The principle study used impedance measurements and a back-up study using Atomic Force Microscope (AFM) measurements was used to qualitatively confirm the impedance results.

The EIS impedance measurements were carried out using sets of gold electrodes and the AFM measurements were performed on gold coated glass slides. Each support was prepared and coated to produce an EDC/NHS activated layer in accordance with the procedures laid down previously in Chapter 7.

9.2.1 Streptavidin immobilisation and Glycine Blocking

Following the SAM activation procedure it was necessary to produce the Streptavidin monolayer. The procedure adopted was based upon the optimum procedures described in Chapter 8. The gold coated glass slides and working electrodes were thoroughly rinsed in DI water and immersed in Streptavidin solution at 21^{o}C for 2 h. They were then thoroughly rinsed again in deionised water to remove Streptavidin molecules which were not covalently bound to the surface. A second cleaning stage then followed where the substrates were immersed in glycine solution for 1h. Glycine was provided by Sigma and was made up to a 0.1 M solution in DI water. The second cleaning stage served to further desorb non-chemisorbed Streptavidin and to block remaining activated sites. The modified slides were then rinsed with deionised water to remove any unbound glycine.

9.2.2 Biotinylated IgG immobilisation procedure

Following the glycine blocking stage the immobilisation procedure was carried out. The working electrodes and two of the gold coated glass slides were thoroughly rinsed in DI water and immersed in biotinylated IgG solution at 21 ^{o}C. The biotinylated IgG solution was prepared from biotinylated sheep IgG purchased from by Immunodiagnostic systems Ltd (IDS Ltd.) and diluted to concentrations of 1.5mg/ml in (PBS, pH=7.4).

Modified working electrodes were withdrawn from the solution at a number of different immersion intervals prior to EIS analysis. The gold coated glass slides were withdrawn after 45 min and 2 h, prior to AFM measurement. In preparation for measurement, both electrodes and Au(III) coated glass sides were rinsed sequentially in DI water, Tween 20 solution and in DI water again, to desorb non-chemisorbed biotinylated IgG molecules. A Streptavidin modified, Au(III) coated glass slide that had not been immersed in b-IgG solution was used as a reference for AFM measurements.

9.2.3 Electrochemical measurements

The impedance measurements were made by incorporating each immersion period test electrode into a conventional three electrode system. Measurements were made using an Autolab potentiostat/galvanostat in conjunction with Frequency Response Analyser (FRA) and General Purpose Electrochemical System (GPES) software (Eco Chemie B.V.). The Ag/AgCl reference electrode, platinum wire counter electrode and gold working electrode (MF-2014) were all purchased from BASi instruments Inc and all electrochemical measurements were performed in PBS buffer solution.

For EIS, a 0.1 mV amplitude sine wave was applied to the working electrode in the tested frequency range of 0.1Hz to 1MHz. The working electrode was polarized at a potential of +0.25V/Ag(AgCl) during measurements, which was shown via CV to be the oxidation potential of the redox indicator. EIS measurements were performed after the working electrodes had been cleaned, after they had been immersed in glycine solution and after IgG and biotinylated IgG solution immersion.

9.2.4 AFM measurements

All modified gold coated glass slides were stored in PBS solution, whilst awaiting measurement, before they were rinsed in purified water (15 MΩ) and dried using an air gun. The surfaces were then profiled using a Nano-R™AFM (Pacific nanotechnology, Santa Clara, CA) in close contact mode in air.

9.3 Results

9.3.1 Atomic Force Microscope (AFM) characterisation of biotinylated Antibody (b-IgG) monolayer

As b-IgG is known to be a large macromolecule (150 kDa), it was possible to view the actual b-IgG monolayer structure using an AFM, thereby attaining detailed qualitative information on the structure without the use of labels or spectroscopic profiling techniques.

The topography of the sample collected after a b-IgG solution immersion time of 0 hrs is shown in Figure 9.1 and is similar to the image produced for the Streptavidin tests shown in Figure 8.1A confirming that a saturated monolayer has been produced.

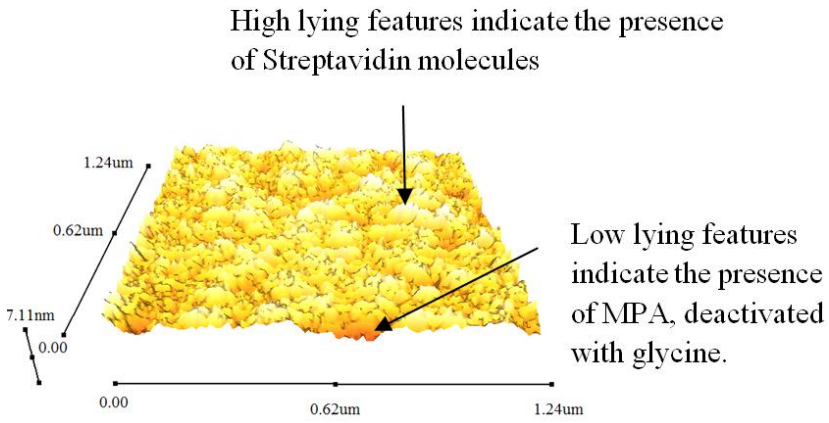

Figure 9.1: AFM profile of a Streptavidin monolayer

Figure 9.2 shows the surface after immersion in b-IgG for 45 minutes. A series of rounded islands approximately 10.66 nm high at the centre and approximately 80 nm in diameter have formed. The height of the island corresponds to the molecular length of a vertically orientated IgG molecule. The diameter is much larger than the molecular length of IgG suggesting that a number of IgG molecules have adsorbed in the vertical orientation around a central point. The island has no discernable features to allow identification of individual antibodies, meaning that the nanoscopic islands formed are densely packed. This implies that the growth mechanism is influenced by IgG already adsorbed on the surface.

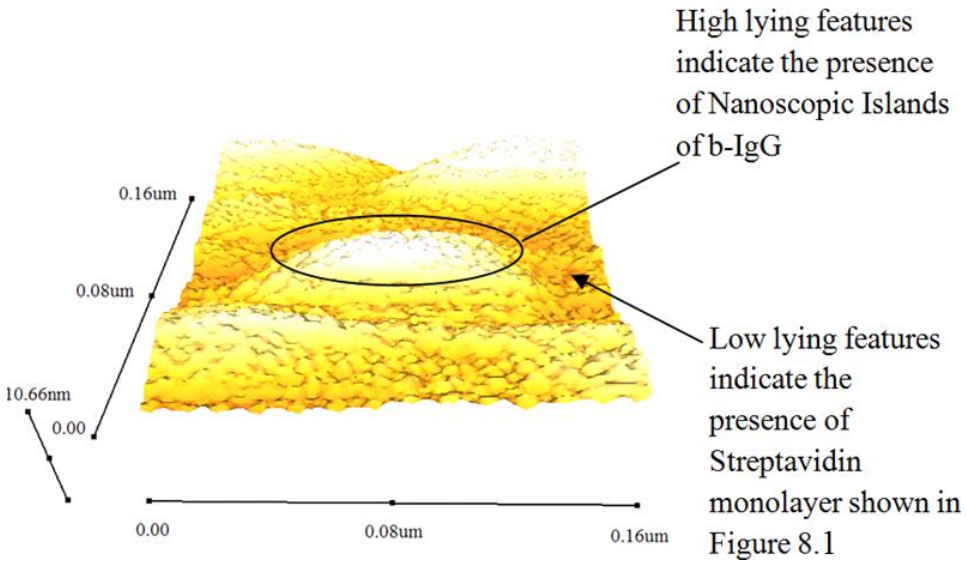

Figure 9.2: AFM profile of the glass slide after an immersion time of 45min in biotinylated IgG solution at 21^{o}C

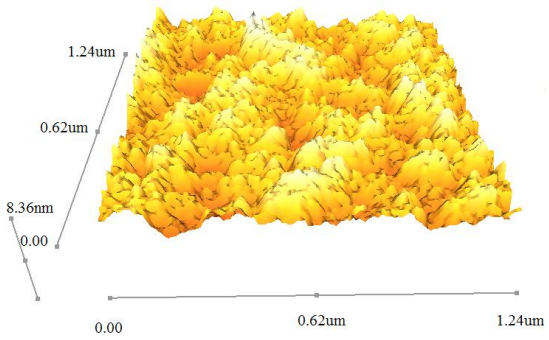

Figure 9.3: AFM profile of the glass slide after an immersion time of 2 hours in biotinylated IgG solution at 21°C, showing how the layer is restructured as the nanoscopic islands grow and merge into a single monolayer. High lying features indicate the presence of b-IgG. Low lying features indicate the presence of the Streptavidin monolayer.

In Figure 9.3 a series of peaks are observed that have a maximum height of 8.36 nm. It is speculated that the nano-crystals observed in Figure 9.2 after 45 minutes of immersion have continued to grow and merge. When merging occurred, arginine, glutamine and asparagine amino acid groups from b-IgG molecules on the fringes of neighbouring islands have interacted causing all the b-IgG molecules in all of the islands involved to rearrange themselves into a different structure. The observed drop in peak height is commensurate with the molecules not being vertically orientated and is a function of the realignment process. This results in a less dense monolayer being formed, affording b-IgG a greater degree of freedom, which has been known to increase sensor sensitivity and is consistent with extant the literature (Diaz-Gonzalez et al, 2005).

9.3.2 EIS characterisation of the biotinylated layer

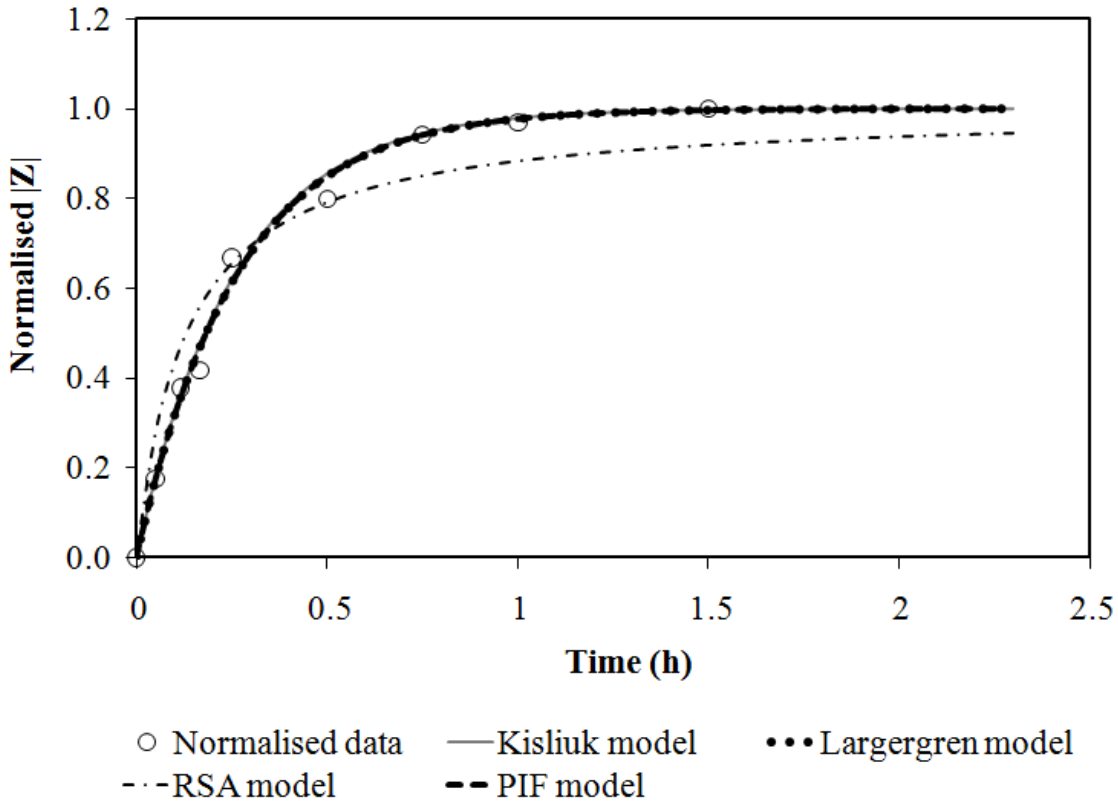

Figure 9.4: A plot of normalised impedance, at 0.1Hz, as a function of biotinylated IgG solution immersion time on a Streptavidin modified substrate, showing the fit achieved by the Kisliuk and Langmuir adsorption isotherms.

The effect of the strength of Streptavidin interactions with constituent b-IgG biotin molecules causes an unusual effect to occur during adsorption. Instead of adsorption taking place predominantly through the ~~–e~~rystal growth" mechanism, traditionally observed in protein adsorption (Shimoni and Gusker, 1995), the vast majority of adsorption in this monolayer takes place through random adsorption and little crystal growth occurs. This results in a high degree of island nucleation occurring through random adsorption followed by a small amount of adsorption occurring through crystal growth. Hence, a large number of nanoscopic islands form that grow and coalesce to form a monolayer.

This is supported by the EIS data (Figure 9.4), which displays a trend that is typical of a process dictated largely by random adsorption, and by AFM measurements (Figure 9.2), which show a number of nanoscopic islands over a 160 x 160 nm area.

9.3.2.1 Equivalent circuit model of the biotinylated layer

The equivalent circuit, shown in Figure 9.5, was used to model impedance data yielded from the Streptavidin modified working electrode and the working electrodes modified with biotinylated IgG monolayers. The reorientation in crystal structure described by Shimoni and Glusker (1995) for protein adsorption during crystal coalescence was not evident from the EIS data. Hence, a single equivalent circuit was used to model each of the complex impedance profiles.

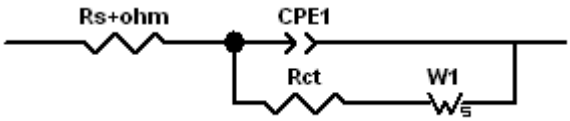

Figure 9.5 The equivalent circuit used to simulate the behaviour of a cleaned gold working electrode signal, the Streptavidin baseline impedance signal and the signals yielded after a b-IgG solution immersion time of 0 h, 15 min, 30 min and 2 h.

As in Chapter 8, it is possible to deduce a number of characteristic from the trends in the constants shown in Table 9.1 and from the impedance plot shown as Figure 9.6. The ohmic resistance and the uncompensated solution resistance are modelled using the Rs+Ohm element, which is constant.

The equivalent circuit data demonstrates that the b-IgG layer that forms over the Streptavidin layer is porous and significantly deeper than the Streptavidin layer itself. This is demonstrated by the increase of W1-T with time, which varied on a scale that is three orders of magnitude greater than that of Streptavidin. The thickness of the b-IgG monolayer also caused a greater hindrance to mass transfer of redox ions than the Streptavidin layer. This was reflected by the increase in W1-R with immersion time, which varied on a scale that was two orders of magnitude greater than that observed for Streptavidin adsorption; was reflected in the increase of Rct (charge transfer resistance of the biolayer) with immersion time, indicating that the rate of charge transfer from redox ions decreased as a function of immersion time, and was indicated in the CPE1-P values, which approached a value of 1 as immersion time increased.

The b-IgG monolayer was also revealed to be low density, serving to decrease the layer capacitance (CPE1-T) as immersion time increased. The monolayer also adsorbed significant amounts of electric field energy, causing the total amount of

measured impedance to have greater dependency on imaginary impedance at low frequency. This is reflected by the increase in W1-P value as immersion time increased.

Table 9.1: Equivalent circuit element values, used in Figure 9.5 to model complex impedance data, shown in Figure 9.6, for biotinylated IgG monolayers formed on Streptavidin modified working electrodes over various biotinylated IgG solution immersion periods. Constants were determined via ZView2 (Scribner Associates). Inc).

	Rs+Ohm	**CPE1-T**	**CPE1-P**	**Rct**	**W1-R**	**W1-T**	**W1-P**
glycine	108	1.14×10^{-6}	0.929	301	1.88×10^{7}	1.15×10^{9}	0.50696
t=15min	108	1.15×10^{-6}	0.928	381.5	2.05×10^{7}	1.35×10^{9}	0.50688
t=30min	108	1.1×10^{-6}	0.939	405.7	2.52×10^{7}	1.36×10^{9}	0.51703
t=2h	108	7.35×10^{-6}	0.974	433.7	2.87×10^{7}	1.52×10^{9}	0.52002

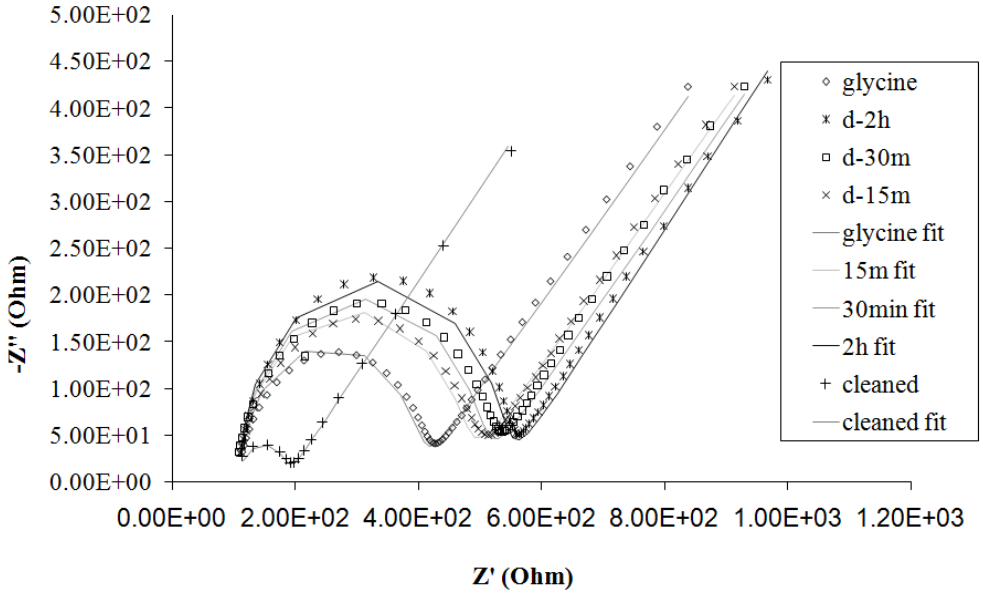

Figure 9.6: A complex impedance plot showing the variation in imaginary (Z‘‘) and real (Z‘) impedance brought about by the presence of biotinylated IgG monolayers on a modified work electrode, as a function of immersion time in biotinylated IgG solution.

9.4 Modelling the b-IgG adsorption process.

In an attempt to model the adsorption process four models RSA, Largergren, Kisliuk and PIF were fitted to the data. The PTCS model was not used in this Chapter as restructuring of the layer did not bring about a detectable change in biolayer electrical

properties at 0.1 Hz. Hence, φ_1 and φ_2 values would be equal and it would not be possible to assign reasonable values to rate constants.

The Newton and Conjugate methods contained within Microsoft Solver routine were used to perform the fits and the objective functions used during the fitting process, for each model, are given in Chapter 3.2. The fitted parameters and the goodness of fit to the experimental data are shown in Table 9.2 for each adsorption isotherm model.

Table 9.2: The RSA, Langmuir, Kisliuk and PIF adsorption isotherm coefficients determined by the least squares method and used to model normalised impedance data at 0.1Hz.

Model	**B**	**R**	**R‟**	k_E	k_R	k'_I	**Chi squared test (χ^2)**	
							χ^2	**Nº of data points**
RSA	0.132	-	-	-	-	-	0.114	9
Largergren	-	3.780	-	-	-	-	0.015	9
Kisliuk	-	-	3.858	$2.29x10^{-06}$	-	-	0.015	9
PIF	-	-	-	-	3.780	1.30×10^{-3}	0.015	9

The fitted isotherms of the RSA, Largergren, Kisliuk and PIF isotherms (equations (3.3), (3.13), (3.19) and (3.38)) are displayed with the normalised experimental impedance data in Figure 9.4. The error between the normalised impedance data collected and the values predicted for the models are shown in Appendix 4.

It can be seen from Figure 9.4 and the tabulated data given in Appendix 4 that each of the models provided a good fit to the experimental data but each of the models had difficulty in following the trend shown by the experimental data over the immersion period 0.5 hrs to 1 hr.

Of the models considered here, the Largergren, Kisliuk and PIF adsorption models approximate the data the best, where the data appears to be scattered randomly about the model curves. The random error here can be attributed to two factors: microscopic Au surface irregularities (brought about during cleaning of the Au surface) and slight irregularities in the Streptavidin modified surface. The values of the rate constants modelling random adsorption in these models (R, R‘ and k_R) are approximately equal. The PIF also provides an additional insight into the relative rate of crystal growth through the rate constant k'_I, which demonstrates that the rate of island growth is four orders of magnitude less than that of random adsorption. This is concurrent with the expected rate values for the nucleation, formation and coalescence of a large number of nanoscopic crystals.

In contrast, the RSA model predicts a much lower rate of formation than is the case. This model provides the least best fit of the models tested in this report, as shown in Table 9.2 and Figure 9.4. Hence, should not be used to model the data over the other adsorption isotherm equations

9.5 Summary

AFM was used in conjunction with EIS data to analyse the growth kinetics and structural properties of the b-IgG monolayer to facilitate the optimisation of the process and providing an insight into how charge transfer occurs over the monolayer.

The strength of the Streptavidin layer interactions with the b-IgG adsorbate caused monolayer growth to primarily occur through random adsorption with a small amount of crystal growth also occurring. Hence, the monolayer formed via the nucleation and growth of large numbers of dense nanoscopic crystals.

The IgG structure that was formed across the surface was found to be porous to redox active ions. However, the b-IgG monolayer substantially inhibited the mass transfer rate of the ions and absorbed significantly more of the detection signal‘s electric field than the Streptavidin monolayer.

Models used to simulate the EIS data included the RSA, Largergren, Kisliuk and PIF models. All models were proven to fit the experimental data well. The Largergren, Kisliuk and PIF models provided the best fit and approximated the data equally as

well as each other. The RSA model demonstrated the least best fit of the four models investigated. The fitted constants from the PIF and Kisliuk models were mutually supportive and were consistent with a large degree of monolayer adsorption being random and a small degree of adsorption being through crystal growth.

Chapter 10: A Comparison between the adsorption kinetics of Biotinylated-IgG monolayers and monolayers consisting of IgG molecules adsorbed directly on to metal substrate.

10.1 Introduction

This chapter aims to compare different methods of attaching IgG to the immunosensor surface. The two methods chosen for comparison were direct adsorption of IgG onto a metal substrate and b-IgG adsorption to a metal surface modified with a Streptavidin monolayer. This comparison was chosen because the direct adsorption process is the simplest route with fewest stages and is likely therefore to represent the cheapest route to market. The Streptavidin process is likely to represent the most sensitive and durable sensor with fewest stages and is therefore the next most promising route.

So far it has been shown that formation of each layer can be modelled and by careful manipulation of the process conditions optimised to give maximum uniform coverage of the surface. The next step is to compare the adsorption processes involved in producing the Streptavidin b-IgG layer with those of the direct addition of IgG to the bare metal substrate. This is a much simpler process and this study should provide some insight into the quantitative benefit of the complex Streptavidin based process.

10.2 Experimental work

To make the comparison between the two preferred routes of sensor manufacture it was necessary to perform extra experimental measurements for IgG direct coating of the gold metal substrates. Two types of experiments were performed to allow comparison with the data gathered for the biotinylated Streptavidin layer reported and discussed in Chapter 9. The experiments involved qualitative measurements made with an atomic force microscope (AFM) and quantitative measurements made using electrochemical impedance spectroscopy (EIS).

The AFM measurements were performed on five gold coated borosilicate glass slides. The EIS measurements were performed using matched sets of three gold electrodes, which had been used in the experimental investigations featured in Chapters 4 to 9. Each of these electrodes had a diameter of 1.6 mm and a surface area of 2.0 mm^2. Each slide or electrode was cleaned using the protocol previously stated for the Streptavidin process (see Chapter 8).

A series of isotherms (at 4, 20,27, 32 and 40 °C) were measured using EIS to identify the optimum temperature then the atomic force measurements were made at the optimum temperature of 20 °C.

10.2.1 Chemicals and solutions

Extra chemicals were required for this process. The IgG coating was produced using sheep IgG provided by Immunodiagnostic systems Ltd (IDS Ltd.) and diluted to a concentration of 1.5 mg/ml in (PBS, pH=7.4). The electrochemical cell solutions consisted of 0.1 M phosphate buffer solution (PBS, pH = 7.4), which contained 0.1 M KCl as supporting electrolyte and 0.05M $K_3Fe(CN)_6$ as redox mediator. All DI water used over the course of this experiment was 15 MΩ, unless stated otherwise.

10.2.2 IgG immobilisation and testing

For the EIS measurements, after cleaning, working electrodes were rinsed with DI water and then immersed in IgG solution at 4 ^{o}C, 20 ^{o}C, 27 ^{o}C, 32 ^{o}C and 40 ^{o}C. After a prescribed immersion time the working electrodes were removed from the solution and rinsed in DI water immediately before and after a Tween 20 solution rinse. This desorbed non-chemisorbed IgG molecules, prior to EIS measurements. The EIS measurements were made in accordance with the procedure set out for the Streptavidin process (see Chapter 8).

For the AFM measurements all modified gold coated glass slides were stored in PBS solution, whilst awaiting measurement. When a measurement was started a glass slide was removed from the PBS solution and rinsed in purified water (15 MΩ) and dried using an air gun. The surface of the substrate was then profiled using a Nano-R™AFM (Pacific nanotechnology, Santa Clara, CA) in close contact mode in air to establish a base case. A second gold coated glass slide was then profiled via AFM This time it was removed from the PBS solution, rinsed in DI water and submerged in IgG solution. The slide was removed from solution after 45 min and rinsed with DI water before and after a subsequent Tween 20 solution rinse to desorb non-chemisorbed IgG molecules. The AFM IgG measurements were only made for a single temperature of 20 ^{o}C which had previously been identified as the optimum process temperature by the EIS measurements.

10.3 Results

10.3.1 EIS Results

The impedance measurements have been processed to produce a normalized impedance plot versus immersion time as shown in Figure 10.1. There are two distinct types of curve. The first type is observed at 4 and 20 °C where a progressive rise is seen from the initial impedance value to a final value which is same for both data sets within the band of experimental error. This seems to suggest that the same degree of surface coverage at saturation is observed at both temperatures and that both final monolayers have similar structures.

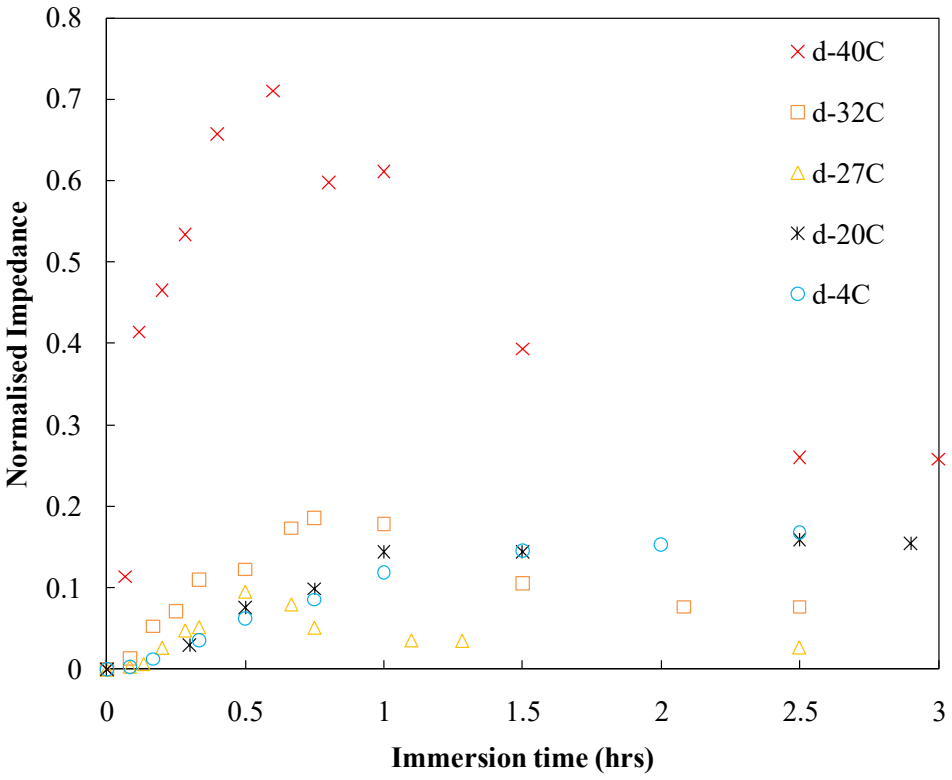

Figure 10.1: Plot of normalised impedance versus immersion time for the immobilisation of IgG directly on to the metal substrate. Five data sets are shown each corresponding to one of the five isotherms at 4, 20, 27, 32 and 40 °C. The data sets at 27, 32 and 40 °C each show a maxima in the curve which is indicative of an equilibrium existing between rate of formation of IgG orientated in the first structure and the rate of formation of second structure at these temperatures.

The curves at 27, 32 and 40°C show much steeper initial rates of impedance rise that increase with temperature and reach maxima after immersion times of between 30 minutes and 1 hour. The curves then show a drop off in impedance with immersion time and do not reach the same final impedance values. The drop in impedance for the datasets measured at temperatures above 20 °C implies that the nature and structure of the adsorbed surface is changing with increased immersion times

The shape of the impedance curves is very reminiscent of those observed for MPA formation which was explained by the presence of two competing structures on the surface. This could be true in this case. There is extant evidence that two structures could exist as a result of reordering of the molecules on the surface in areas of higher adsorbed concentrations of IgG, caused by the intermolecular interactions of proteins in different crystals on the surface and which would give rise to different dielectric properties in the monolayer (Shimoni and Glusker, 1995). The implication of two structures forming is that the reordering process is relatively slow in comparison to the rate of adsorption at higher temperatures. The fact that the final impedance values are different for each temperature implies that the reordering of the layer is temperature dependant and that each temperature gives rise to different degrees of final surface coverage and amount of disorder.

10.3.2 AFM results

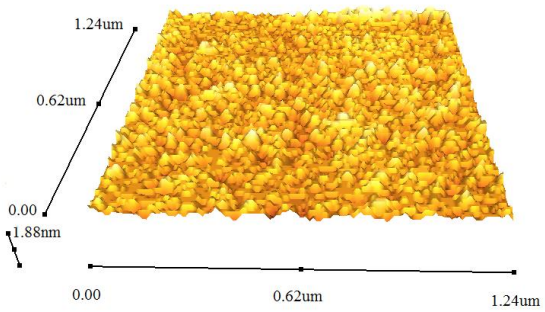

Figure 10.2: The AFM close contact profile of a gold surface at an adsorption temperature of 20 ^{o}C, showing a surface roughness of less than 1 nm;

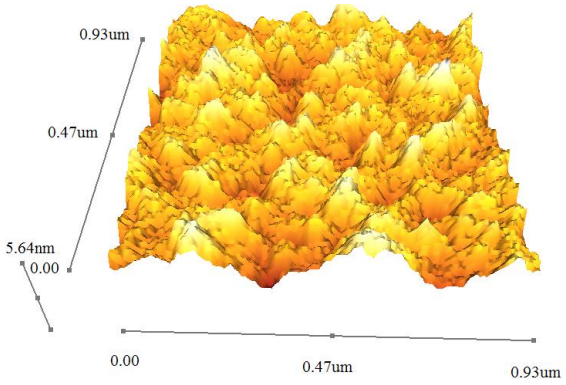

Figure 10.3: The AFM close contact profile of an IgG monolayer adsorbed to a gold substrate surface.

An AFM study was conducted to support the EIS measurements to verify the existence of an IgG monolayer over the gold substrate surface at the suggested optimum immersion temperature (20 ^{o}C) and to study the structure of the monolayer that was formed. 20 °C was selected as the optimum temperature because it was the highest temperature where a single consistent structure on the surface.

The surface topological profile of a smooth gold surface was measured (Figure 10.2) before the antibody monolayer was adsorbed to the surface and the monolayer was profiled (See Figure 10.3). The difference between the two figures indicates a

significant change in surface roughness which is commensurate with the successful attachment of the antibody layer.

Individual Fab and Fc fragments cannot be discerned as it is expected that arginine, asparagine and glutamine amino acid side chain interactions between adjacent IgG molecules distort the IgG molecules about their hinge region. This causes the shape of the macromolecules to deviate from their traditional ―Y" shape and cause them to aggregate together in non-uniform shapes.

10.4 Modelling the EIS results

It is proposed to treat the modelling of the EIS results as two separate sets to mirror the observed shapes of the impedance immersion time isotherms shown in Figure 10.1.

10.4.1 Modelling of isotherms at 4 and 20 °C.

These two data sets were grouped together because neither seemed to exhibit the formation of more than one structure on the surface. The adsorption was thought to be affected by molecules already adsorbed on the surface as part of the process because the molecules involved are large and will exert significant Van der Waals forces in addition to strong intermolecular amino acid side chain interactions. Thus it was decided to fit these data sets with two adsorption models, those of Kisliuk and the PIF model. The Kisliuk model includes a sticking factor that accounts for interactions with adsorbed molecules on the substrate. The PIF model is more specific and has two constants which account for the specific adsorption of molecules randomly on the surface and the absorbance of molecules influenced by species already on the surface respectively (crystal growth).

Fitting was undertaken using the least squares method as defined by the objective function given in equation (3.14) for the Kisliuk model and equation (3.39) for the PIF model.

The objective functions were minimized using the Newton and Conjugate methods contained within Microsoft Solver routine. The fitted parameters and the goodness of fit to the experimental data are shown in Table 10.1 for the 4 ^{o}C and 20 ^{o}C temperature data sets.

Table 10.1 Fitted parameters for the Kisliuk and PIF adsorption isotherm models at 4 and 20 °C

Temperature	**Kisliuk**				**PIF**			
	k_E	**R**	φ	χ^2	k_{R1}	k''_{I1}	φ	χ^2
4 ^{o}C	7.954	0.372	0.154	0.00760	0.523	2.458	0.155	0.00565
20^{o}C	15.317	0.321	0.159	0.00586	0.323	4.915	0.159	0.00586

The fitted isotherms calculated by application of the Kisliuk and PIF models are displayed with the normalised experimental impedance data in Figure 10.4.

The error between the normalised experimental data and the values predicted by the Kisliuk model at 4 ^{o}C are shown in Table A5.1 and the corresponding error for the values predicted by the PIF model are shown in Table A5.2.

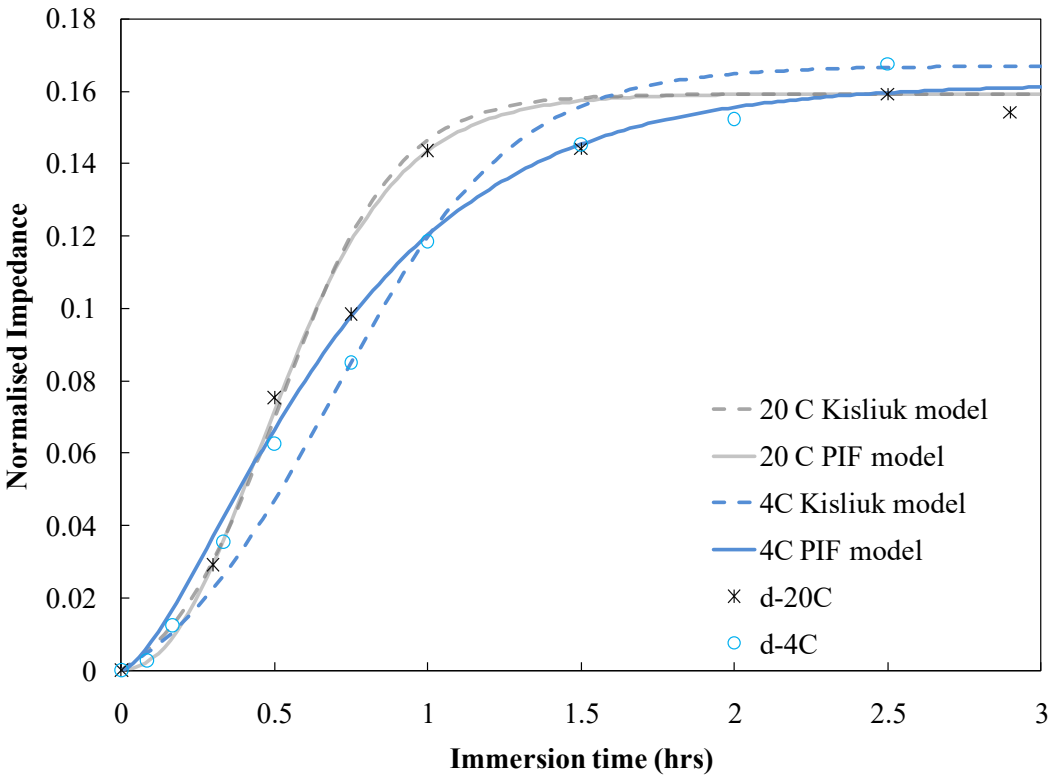

Figure 10.4: Plot of the normalised impedance versus the immersion time for isotherms measured at 4 and 20 °C the graph also shows the curves derived from the Kisliuk and PIF models for the both isotherms. For the 4°C data set it is clear that the PIF model gives a much better fit of the data. For the 20°C data set no discernable difference is seen.

It can be seen that a good fit and similar levels of uncertainty are observed for both models and isotherms, as the temperature datasets predicted by both models provided a χ^2 value significantly less than the number of data points obtained at a particular temperature. The majority of the data is scattered randomly about the model curves with no trend between the amount of error observed and immersion period. These random errors could be attributed to the microscopic Au surface irregularities brought about during cleaning of the Au surface. Visual inspection of the fits (See Figure 10.4) and the measured chi squared values (Table 10.1) suggests that for the 4 °C temperature trace the PIF model provides the best fit. No such observation can be made for the 20 °C data set.

It is concluded that both the Kisliuk and PIF models can be effectively applied to model the adsorption of an IgG monolayer to an Au surface via nitrogen atom lone pairs of electrons. However the PIF gives more information about the relative contributions of random and island growth adsorption to adsorption through the fitted constants.

10.4.1.1 Observations about the mechanism for immobilisation of IgG between 4 and 20 °C

A more detailed examination of the impedance isotherms and the fitted constants of the adsorption models can give some insight into the mechanism for the immobilisation of IgG. From Figure 10.1 it can be seen that for immersion times up to 20 minutes the impedance changes for both isotherms are very similar. This indicates that temperature has little effect and that the mode of adsorption is random adsorption on the surface. After 20 minutes the impedance measurements start to rise more rapidly for the 20 °C data set. This suggests a second, temperature sensitive, adsorption process is taking place and that this is a consequence of the molecules of IgG already adsorbed on the surface. This is supported by the data presented in Table 10.1. For the PIF model k_{R1} and k'_{I1} are constants representing relative adsorption by random processes and by island growth mechanisms respectively. It is noticed that the k_{R1} is significantly greater than k'_{I1}, indicating that island formation is more significant than random formation at both temperatures. It can also be seen that k'_{I1} decreases as k_{R1} rises with an increase in temperature. This is consistent with the change in impedance with temperature observed in Figure 10.1 and indicates that the island growth process is becoming more dominant at higher temperatures. For the Kisliuk model the k_E sticking factor is also seen to rise with temperature indicating the increase in the affect of adsorbed species on the process and confirming observed behaviour. Both curves seem to level off at the same impedance value indicating the same surface coverage and structure is achieved for both isotherms.

10.4.2 Modelling of isotherms at 27, 32 and 40 °C.

The remaining three isotherms at 27, 32 and 40 °C were treated together because from Figure 10.1 they seem to form two structures on the substrate surface. The same two absorbance models were used because island growth is thought to become more significant at higher temperatures. To account for the two structures the absorbance models were used in conjunction with the PTCS model (equation (3.43)). The objective functions used for the PTCS-Kisliuk and the PTCS-PIF equations are included as equation (3.46) and (3.47), respectively.

The objective functions were minimized using the Newton and Conjugate methods contained within Microsoft Solver routine.

The fitted isotherms for these three isotherms are displayed with all of the normalised experimental impedance data in Figure 10.5. From a visual inspection one data point (immersion time 0.75 hours) for the isotherm a 27 °C appears to be reading low and may be an erroneous data point which appears to be skewing the fit of the PTCS-Kisliuk model. Careful examination of the 32°C isotherm seems to show that a further point (immersion time 0.5 hours) is also reading low and again seems to be distorting the PTCS-Kisliuk model fit. No sifting of the data can be carried out for the 40 °C dataset because it is not possible to discriminate which points may be in error.

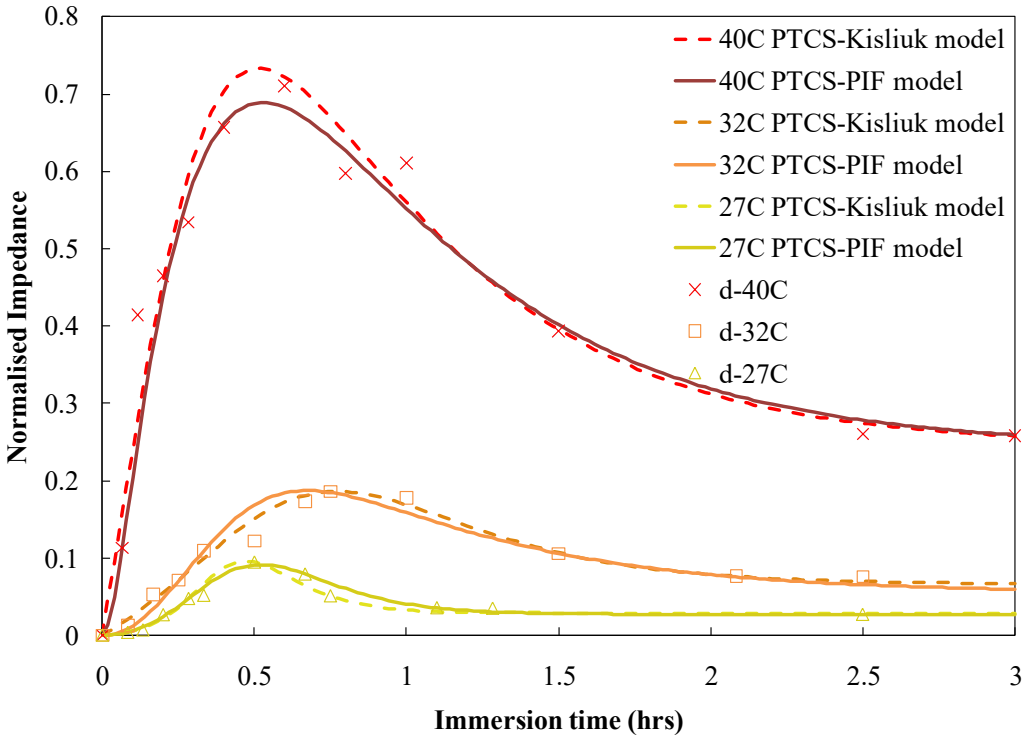

Figure 10.5: Plot of the normalised impedance versus the immersion time for isotherms measured at 27, 32 and 40 °C. The graph also shows the curves derived from the PTCS-Kisliuk and PTCS-PIF models for all isotherms. The fits achieved by the models appear to be in line with the uncertainty in the data.

It was decided to refit the models to the isotherm data sets with the spurious points removed. These results are shown in Figure 10.6 and the fitted parameters and the goodness of fit to the PTCS-Kisliuk and PTCS-PIF models are shown in Table 10.2 and 10.3 respectively.

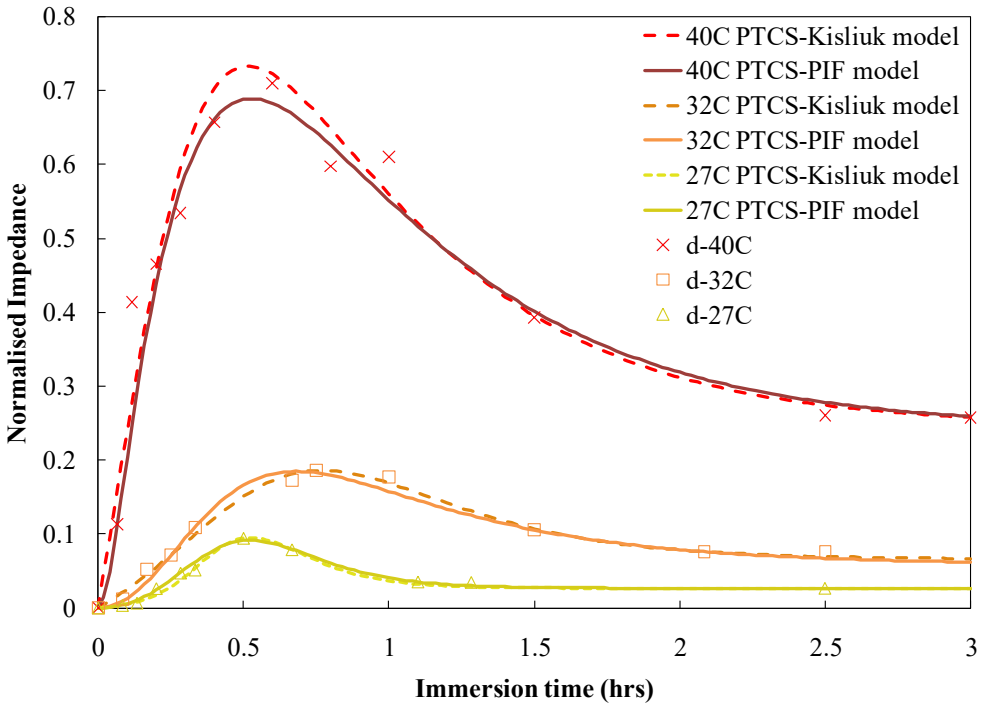

Figure 10.6: Plot of the normalised impedance versus the immersion time for isotherms measured at 27, 32 and 40 °C with erroneous data points removed. The graph also shows the curves derived from the PTCS-Kisliuk and PTCS-PIF for the 27°C isotherm now line up perfectly indicating the Kisliuk model is less reliable when the base data set contain spurious data points.

For the 27 °C data set the Kisliuk model curve now lies on top of the PIF model curve. A minor improvement in agreement between the two models is reported for the 32 °C. It can be seen that a good fit is obtained for both models at 40 °C. The uncertainty of using either model over the temperatures range of 27 °C to 40 °C, is small given that χ^2 values are significantly less than the number of data points obtained at a particular temperature. Finally, the results seem to suggest that the PIF model is less susceptible to error induced by the presence of spurious data points and should be given greater credence when using the models to infer possible adsorption mechanisms.

Table 10.2 Fitted parameters for the PTCS-Kisliuk adsorption isotherm models at 27-40 °C.

Temperature	PTCS-Kisliuk						
	k_{E1}	R_1	k_{E2}	R_2	φ_1	φ_2	χ^2
27 °C	66.94	0.170	40.8	0.179	0.200	0.0289	0.008598
32 °C	8.069	0.453	4.03	0.509	0.499	0.0660	0.011203
40 °C	2.089	1.927	1.26	0.769	1.227	0.246	0.092678

Table 10.3 Fitted parameters for the PTCS-PIF adsorption isotherm models at 27-40 °C.

Temperature	PTCS-PIF						
	k_{R1}	k'_{I1}	k_{R2}	k'_{I2}	φ_1	φ_2	χ^2
27 °C	0.259	9.268	0.0289	5.250	0.201	0.0268	0.00610
32 °C	0.521	3.490	0.3946	2.117	0.432	0.0642	0.01093
40 °C	2.557	3.036	0.3204	2.152	1.008	0.2522	0.08423

10.4.2.1 Observations about the mechanism for immobilisation of IgG between 20 and 40 °C

The impedance isotherms are complex and difficult to rationalise above 20 °C from the given data. However, a more detailed examination of the profiles in conjunction with an examination of the fitted constants of the adsorption models is warranted.

From Figure 10.6 it appears that the initial change in impedance increases rapidly with increasing temperature. This is indicative that the adsorption process has changed from that observed for the 4 and 20 °C isotherms. Careful examination of the k_{R1} and k'_{I1} constants suggested that k_{R1} increases rapidly while k'_{I1} decreases with temperature. This implies that the number of successful random collisions of IgG molecules with the gold substrate has increased with temperature. Further this implies that the random adsorption process of IgG on to gold is controlled by a significant activation energy barrier. This activation energy barrier is overcome at the higher temperatures and the random adsorption process dominates.

The peak impedance values ($_1$) are observed to increase significantly with temperature. This implies that the rate of adsorption of structure 1 onto the surface is much quicker than the reordering of molecules to produce structure 2. Further it implies that the nature of both structures formed has changed with temperature.

After about 2.5 hours all isotherms seem to have reached steady state plateaux (Figure 10.6). Final impedance values are observed to drop from 1.59 at 20 °C to 0.028 at 27°C before rising again to 2.4 at 40 °C. This implies that the final structure undergoes complex changes as the temperature increases that require further investigation. The current experimental evidence is insufficient to conclude whether these thermal changes are beneficial or detrimental to the final sensors performance.

10.5 Summary

An experimental investigation of the effects of temperature and immersion time on the formation of IgG directly on to a metal substrate has been performed. The results of the tests have been analysed using EIS and AFM. The EIS impedance measurements have been modelled successfully using variations of the PTCS-Kisliuk and PTCS-PIF adsorption models.

The EIS measurements and fitted adsorption models suggest that the direct adsorption of IgG onto gold substrates is a complex process that is significantly dependant on temperature. The optimum conditions for forming an IgG layer on the bare metal substrate were considered to be 20 °C and an immersion time of 2 hours. These conditions represent the highest temperature where a stable single structure is known to form on the surface in the shortest time. Above this temperature multiple structures have been shown to form that could affect the sensitivity of the sensor and further work is required to definitively determine the optimal structure.

For chapter 9 it was concluded that the final stage of the IgG addition via the multistage process involving Streptavidin is a simple process involving the formation of a single structure largely by random adsorption. It is therefore easier to control to produce a repeatable layer of a given consistency than the direct addition method.

Comparison of the AFM studies for both processes at 20 °C suggest that the IgG molecules adsorbed via the Streptavidin multilayer process protrude further above the surface (10.66 nm) than the layer produced by direct adsorption to the metal surface (5.64 nm). This implies that the b-IgG is more vertically orientated and that a higher packing density of IgG molecules is achieved for the multistage process. Therefore, the sensor formed via the multilayer process is more likely to have a greater number of Fab fragments orientated away from the surface than the IgG layer, possibly affording the immunosensor a better sensitivity and a lower limit of detection. This would be consistent with extant literature findings.

Chapter 11: Conclusions

A systematic survey was carried out to investigate the different routes of producing an IgG based immunosensor. Two methods, direct adsorption of IgG onto a metal substrate and b-IgG adsorption to a metal surface modified with a Streptavidin monolayer were chosen for further study from this survey as they seemed to show the most promise for further development. These processes were chosen because the direct adsorption process is the simplest route with fewest stages and is likely therefore to represent the cheapest route to market. The Streptavidin process was thought to represent the most sensitive and durable sensor with fewest stages and is therefore the next most promising route.

The Streptavidin based process was the most complex and therefore examined first. It consists of 5 stages: cleaning of the metal substrate, MPA adsorption, activation with EDC/NHS solution, adsorption of Streptavidin and adsorption of biotinylated IgG. It was decided to concentrate on the bulk properties of each layer as it was produced and how the layer properties varied as functions of immersion time and temperature. EIS was identified as principle measurement technique to be used to measure the bulk properties and confirmations studies were carried out using a combination of different techniques including. Contact angle measurements, FTIR microscopy with BSA molecular labels and Fluorescence microscopy for small adsorbed molecules and AFM for layers assembled from macromolecules.

For the cleaning stage two different cleaning techniques were required depending on whether inorganic contaminants are present on the surface. It was found that the optimum working electrode pre-treatment ordinarily involves mechanical polishing followed by ultrasonication in purified water for 10 min and subsequently ultrasonication in piranha solution for 40 min. However, mechanical polishing followed by ultrasonication in purified water for 10 min and subsequently electropolishing should be employed to remove contamination when inorganic contaminants are present on the surface. The electropolishing is undertaken in 1M sulphuric acid and over the period of 30 sweeps, where each sweep occurs between potentials of 0 V and 1.5 V and occurs at a rate of 0.5 V/s.

For the MPA adsorption process characterisation was carried out using Electrochemical Impedance Spectroscopy (EIS) for temperature–time isotherms ranging from 4 ^{o}C to 40 ^{o}C. Infra-red reflection absorption spectroscopy (IRRAS) was used to confirm EIS data at an immersion temperature of 20 ^{o}C.

Changes in the resistance and capacitance of the monolayer over immersion time allowed the recognition of two distinct structures in monolayer self assembly. Initially, MPA occupying the lying down configuration was formed and evolved into a structure consisting entirely of MPA in the standing up configuration. Both structures displayed an increase in disorder with increased immersion temperature above 20 ^{o}C. Also, a disordered structure at an immersion temperature of 4 ^{o}C was displayed as a result of decreased solubility of MPA in ethanol.

No extant adsorption model can model the presence of two sequentially forming structures on the surface of a substrate. Therefore a new model (PTCS) was developed which uses a mass balance to account for the percentages of each structure on the surface and an existing adsorption model for example Kisliuk to model the actual adsorption process. The PTCS was used to model the normalized impedance data for all isotherms. The model was found to provide a good fit to all experimental data and allowed the deduction of the optimum immersion conditions as being 12 hrs at 22 °C.

EDC/NHS activation was studied initially by Contact Angle measurement and subsequently by FTIR profiling and fluorescent microscopy at 22 ^{o}C. These techniques suggested that activation of the carboxylic layer occurred by more than one process and that the presence of adsorbed activation species on the surface influenced the adsorption processes.

EIS was then used to look at the bulk properties of the activated layer during activation and the influence of temperature in more detail. A systematic study of the activation process was carried out by measuring seven different isotherms from 4 ^{o}C to 30 ^{o}C. The measurements clearly confirmed that the activation process proceeded in two stages and that two structures could be present on the surface. They also suggested that the relative rates of growth of the structures could be controlled by manipulation of the temperature to optimize the activated layer.

Determination of the optimum conditions for activation required an understanding of the kinetics and mechanisms of the processes taking place. To acquire this knowledge a new mathematical model (PTCS- PIF) that accounts for the individual contributions to activation by both random and island growth processes and the effects of surface coverage by two sequential structures was developed.

This model allowed the following deductions to be made. At very low temperatures (less than 4 °C) adsorption of both EDC and NHS is mainly by random adsorption. At temperatures between 4 °C and the Gyepi-Garbrah temperature for the MPA (~24 °C) EDC adsorption is controlled by island growth and NHS is a much slower process controlled by random adsorption. At temperatures above the Gyepi-Garbrah temperature for the MPA, both adsorption processes are controlled by island growth. A more uniform activation is achieved by island growth therefore the optimum conditions for activation are at or above the Gyepi-Garbrah temperature for the MPA formation.

Formation of the subsequent Streptavidin and b-IgG monolayers were studied using Electrochemical Impedance Spectroscopy (EIS) and Atomic Force Microscopy (AFM).

During Streptavidin monolayer formation, three distinct stages of formation were identified from the AFM results. Initially random adsorption is the dominant process, then crystal growth becomes evident where adsorption is influenced by adsorbed Streptavidin and finally the adsorption rate decreases as surface approaches saturation.

The EIS measurements were modelled using the RSA, Largergren, Kisliuk and PIF isotherm models and the statistical analysis of the fitted models revealed that the PIF isotherm provided the best approximation to experimental data. The optimum immersion period was identified as 2 hours.

During b-IgG monolayer adsorption, the strength of the Streptavidin layer interactions with the b-IgG adsorbate caused monolayer growth to primarily occur through random adsorption with a small amount of crystal growth also occurring. Hence, the monolayer formed via the nucleation and growth of large numbers of dense nanoscopic crystals.

Models used to simulate the EIS data yielded from the b-IgG adsorption process included the RSA, Largergren, Kisliuk and PIF models. All models were proven to fit the experimental data well. The Largergren, Kisliuk and PIF models provided the best fit and approximated the data equally as well as each other and the RSA model demonstrated the least best fit of the four models investigated. The fitted constants from the PIF and Kisliuk models were mutually supportive and were consistent with a large degree of monolayer adsorption being random and a small degree of adsorption being through crystal growth.

For the direct adsorption of IgG onto metal substrates a systematic study was performed using EIS and AFM to investigate the effects of temperature and immersion time on the properties of the adsorbed monolayer. The EIS impedance measurements have been modelled successfully using variations of the PTCS-Kisliuk and PTCS-PIF adsorption models. The EIS measurements and fitted adsorption models suggest that the direct adsorption of IgG onto gold substrates is a complex process that is significantly dependant on temperature. It was concluded that the optimum conditions for the formation of the layer were 20 °C and an immersion time of 2 hours. These conditions represent the highest temperature where a stable single structure is known to form on the surface in the shortest time. Above this temperature multiple structures have been shown to form that could affect the sensitivity of the sensor and further work is required to definitively determine the optimal structure.

Overall, it is concluded that the final stage of the multilayer Streptavidin process is a simple process involving the formation of a single structure largely by random adsorption. It is therefore, easier to control to produce a repeatable layer of a given consistency than the direct addition method. Comparison of the AFM studies for both processes at 20 °C suggest that the IgG molecules adsorbed via the Streptavidin multilayer process are more vertically orientated and that a higher packing density of IgG molecules is achieved for the multi stage process.

Chapter 12: Future work

The studies featured in this thesis cover a wide range of areas each of which can be expanded upon to provide a potentially valuable contribution to knowledge. Ways in which these areas can be expanded are as follows.

12.1 Further cleaning studies

The cleaning studies carried out as part of this thesis enabled an effective cleaning and polishing regime to be developed to facilitate reproducible measurements. However, it would be useful to expand this study to obtain additional information, allowing this process to be optimised. Two studies that would contribute toward this goal include:

1. Identifying the nature of the effects of initial surface contamination on the completed immunosensor‘s sensitivity and reproducibility. This involves constructing calibration curves from several b-IgG modified electrodes, based on surfaces which have been cleaned to a predetermined extent.
2. Producing regular, flat surfaces through the use of flame annealing, electroplating and electropolishing techniques to improve sensor sensitivity and reproducibility. A range of different electrodes with different roughnesses would be prepared. The effect of roughness will then be correlated against calibration curves from immunosensors that have been constructed on top of the prepared electrode surfaces.

12.2 Further SAM studies

Chapter 6 provides a fundamental investigation, which could form a basis for a number of other SAM modelling studies. Such studies would provide a number of other useful insights, allowing SAM adsorption to be modelled to a greater extent. This has a wide range of applications; both to the optimisation of the device studied in this thesis as well as for other examples of SAM use.

Ways in which the study of the PTCS-Kisliuk adsorption isotherm equation can be expanded upon include:

1. A study to apply the PTCS-PIF adsorption isotherm equation to model SAM adsorption. This will provide additional insights into SAM adsorption as it has done for the subsequent monolayer adsorption stages in this thesis.

2. Examining the relationship between fitted PTCS-Kisliuk and PTCS-PIF variables and SAM chain length.
3. Examination of the relationship between the adsorption models‘ variables and temperature. This requires more temperature traces to be obtained and modelled.
4. Observing how varying concentrations of two or more SAMs in a mixture affects the variables of the fitted PTCS-Kisliuk and PTCS-PIF models (where each SAM consists of different chain lengths).
5. The affect of the SAM molecules‘ functional end groups on the fitted PTCS-Kisliuk and PTCS-PIF model.
6. The effect of using different solvents on the variables of the fitted PTCS-Kisliuk and PTCS-PIF models.

12.3 Expansion of the MPA activation study

The work done to optimise carboxylic acid group activation using EDC and NHS in this thesis could be expanded to include:

1. The effect of temperature on fitted PTCS-Kisliuk variables and fitted PTCS-PIF variables. However, more temperature traces would need to be obtained before there is an adequate amount of data to deduce what these relationships are.
2. It has been established that hydrolysis of EDC, *O*-acylisourea and NHS-ester is a hindrance to the activation process. Hydrolysis may be minimised by using alternative solvents, in place of water. It is expected that this study, if successful, could improve the final yield of NHS-ester on the surface and increase the sensor sensitivity.

12.4 Expansion of the Streptavidin and b-IgG monolayer studies and optimisation of the activated carboxylic acid blocking step

The optimisation studies for Streptavidin and b-IgG provided a useful insight into monolayer kinetics. However, another useful study that could be undertaken is the activated carboxylic acid blocking stage. Though the time period for blocking used in this study is widely accepted as being adequate, it may be possible to optimise this stage further by determining the influence of temperature and immersion time on adsorption.

The Streptavidin and b-IgG layers were effectively optimised for immersion time and a number of insights were gained into the adsorption kinetics. The process could be optimised by investigating the effect of temperature on adsorption.

12.5 Detection of Analyte (antisheep IgG)

The final step in sensor construction is to construct a calibration curve by using the immunosensor developed to detect various concentrations of analyte and correlating the impedance signal obtained at a particular frequency (which returns the largest response at a given concentration). As the type of monoclonal antibody used in this study is ―sheep IgG," the appropriate analyte is antisheep IgG.

Nomenclature

C	-	Capacitance
c	-	Concentration of the adsorbate in the liquid phase
C_{dl}	-	Double layer capacitance
CPE-P	-	An equivalent circuit modelling coefficient for a CPE that is equal to capacitance when CPE-T is equal to 1.
CPE-T	-	An equivalent circuit modelling coefficient for a CPE, reflecting the amount of real and imaginary impedance contributed by the CPE element that can occupy a value between 0 and 1. A value of 0 represents a purely resistive element and a value of 1 represents a purely capacitive element.
C^*_o	-	Oxidant concentration at the electrode surface
C^*_r	-	Reductant concentration at the electrode surface
D_o	-	Oxidant diffusion coefficient
D_r	-	Reductant diffusion coefficient
d	-	Monolayer thickness
e	-	Charge on an electron
F	-	Faraday constant
Fi	-	A coefficient representing the additional interactions that only exist around Streptavidin crystals present on the substrate surface.
Fs	-	A coefficient encompassing all forces encouraging random adsorption of Streptavidin to the substrate.
f	-	A.C. electrical current frequency
ΔG_{ads1}	-	Gibbs free energy of the MPA adsorption that is dictated mainly by the S-Au interaction.
ΔG_{ads2}	-	Gibbs free energy of MPA adsorption over the transitional structural formation stage.
$\Delta G_{R\text{-}Au}$	-	Gibbs free energy evolved from the MPA chain-Au Van Der Waals interactions.
ΔH_{ads1}	-	Enthalpy evolved from MPA adsorption to gold.
I	-	Electrical current
K	-	A Freundlich adsorption isotherm constant that is determined experimentally.

k_a	-	Rate of rod deposition in the random sequential adsorption model
k_B	-	Boltzmann constant
k_E	-	Kisliuk model sticking coefficient
k_{ES}	-	Rate of desorption from the precursor state into the bulk solution in the Kisliuk model
k_{EC}	-	Rate of adsorption around adsorbate molecules on the surface from the precursor state in the Kisliuk model
k_I‘	-	PIF island formation rate constant
k_R	-	PIF random adsorption rate constant
k_{p1}	-	Largergren rate constant
n_i	-	The population of ions at a particular distance along the electrode surface normal.
n_i^0	-	Bulk concentration ion population
N_{S0}	-	Original number of moles of sites that are available for binding in the PIF model
N_S	-	Moles of vacant sites at any time t in the PIF model
N_{St}	-	Number of moles of sites that are available for binding after time t in the PIF model
P	-	Equilibrium adsorbate pressure
R	-	Universal gas constant
R_{ct}	-	Charge transfer resistance of the multilayer in an equivalent circuit
R_s	-	Solution resistance in an equivalent circuit
Rs+ohm	-	Ohmic resistance and the uncompensated solution resistance in a Zview simulation of an equivalent circuit
R‘	-	Kisliuk random adsorption rate constant.
S_D	-	Probability of an adsorbate molecule randomly adsorbing to the surface from the precursor state, in the Kisliuk model.
S_E	-	Probability of a molecule forming around an adsorbate molecule on the adsorbate surface from the precursor state, in the Kisliuk model.
ΔS_{ads1}	-	Entropy introduced as a result of MPA molecule adsorption
SM	-	Filled particle sites

S^*	-	Empty surface sites
T	-	Absolute temperature
t	-	Adsorption time
V	-	Potential difference
W1	-	Finite-length Warburg impedance
W1-P	-	Models the difference between the observed phase angle at low frequency and the ~~i~~deal" phase angle, which is 0.5 for experimental data with ideal mass transfer.
W1-R	-	A Warburg impedance equivalent circuit constant formed as a result of Warburg impedance equation simplification and is dictated by the Warburg coefficient.
W1-T	-	A Warburg impedance equivalent circuit function of diffusion layer thickness and diffusion coefficient of redox ions through the diffusion layer media.
x	-	Mass of final adsorbate present on the adsorbent
Y_0	-	A CPE constant that is equal to capacitance when n is 1
$\|Z\|$	-	Total impedance arising from a vector consisting of imaginary and real impedance
$\|Z\|_{CPE}$	-	Total impedance introduced by the CPE
$z_{t(expt)}$	-	Measured normalised impedance of the layer after an adsorption time of t.
z_i	-	charge on ion i
Z'	-	Real impedance
Z''	-	Imaginary impedance

Greek letters

γ	-	Euler constant
ε_r	-	Relative permittivity
δ	-	A function that represents Nernst diffusion layer thickness
Θ	-	Fractional coverage of a surface with adsorbate
Θ_1	-	Fraction of the surface covered with the first structure at a certain immersion time in the PTCS adsorption isotherm model

$\Theta_{1(t)}$	-	Fractional coverage of structure one as a function of immersion time in the PTCS adsorption isotherm model.
Θ_2	-	Fractional coverage of the substrate surface with the second structure in the PTCS adsorption isotherm model.
$\Theta_{2(t)}$	-	Fractional coverage of structure two as a function of immersion time in the PTCS adsorption isotherm model.
$\Theta(\infty)$	-	Fractional coverage of a saturated substrate
Θ_{S0}	-	Available fraction of the substrate for adsorbate to form on.
$\Theta_{(t)}$	-	Fractional coverage of the substrate surface after adsorption time t.
Θ_{Total}	-	Total fractional coverage of the substrate with adsorbate in the PTCS adsorption isotherm equation
$\rho(t)\sigma$	-	Rod number density on the surface after immersion time t, in the RSA model
$\rho(\infty)\sigma$	-	Saturated rod density, in the RSA model
φ	-	Proportionality constant
φ_1	-	A PTCS coefficient corresponding to the peak coverage of structure 1 on the surface
φ_2	-	A PTCS coefficient corresponding to the final concentration of structure 2 on the surface
χ^2	-	Chi squared value, determining the goodness of fit between isotherm model predicted values and experimental data.
ω	-	radial frequency

References

Al-Mekhnaqi, A.M., M.S. Mayeed, G.M. Newaz., (2006) ―Adsorption of Protein/Polypeptide on Bioimplant Surfaces by Monte Carlo Simulations,‖ Nanomed: Nanotechnol. Biol. Med., 2, 313.

Alon, R., E.A. Bayer, M. Wilchek, (1993), ―Affinity cleavage of cell surface antibodies using the avidin-biotin system,‖, J. Immunol. Methods., 165, 127.

Alqaradawi, S.Y., A. S. Aljaber, M. M. Khader, (2003), ―Activation and stabilization of gallium arsenide anode in an aqueous photoelectrochemical cell.‖ Thin Solid Films, 444, 282.

Angerstein-Kozlowska, H., B.E. Conway, A. Hamelin, L. Stoicoviciu, (1986), ―Elementary steps of electrochemical oxidation of single-crystal planes of Au—I. Chemical basis of processes involving geometry of anions and the electrode surfaces‖, Electrochim. Acta, 31, 1051.

Barber J.P. (2006), ―Fabrication of hollow optical waveguides on planar substrates,‖ A thesis submitted in partial fulfilment of the requirements of Brigham Young University for the degree of Doctor of Philosophy. Utah, USA: Brigham Young University.

Bard A.J., L.R. Faulkner, (2001), ―Electrochemical Methods Fundamentals and Applications,‖ Hoboken, John Wiley and Sons, Inc.

Barreiros dos Santos, M., C. Sporer, N. Sanvicens, N. Pascual, A. Errachid, E. Martinez, M.-P. Marco, V. Teixeira, J. Samiter, (2009), ―Detection of pathogenic Bacteria by Electrochemical Impedance Spectroscopy: Influence of the immobilization strategies on the sensor performance,‖ Procedia Chemistry, 1, 1291.

Barton, A.C., S.D. Collyer, F. Davis, G.Z. Garifallou, G. Tsekenis, E. Tully, R. O‘Kennedy, T Gibson, P.A. Millner, S.P.J. Higson, (2009), ―Labeless AC impedimetric antibody-based sensors with pg ml−1 sensitivities for point-of-care biomedical applications.‖, Biosens. Bioelectron., 24, 1090.

Ben-Jacob, E., Z. Hermon, S. Caspi, (1999) ―DNA Assembly on 2-Dimensional Array of Colloidal Gold‖, Phys. Lett., A263, 199.

Booth, B.D., S.G. Vilt, C. McCabe, G. Kane Jennings, (2009) ―Tribology of Monolayer Films: Comparison between n-Alkanethiols on Gold and n-Alkyl Trichlorosilanes on Silicon‖, Langmuir, 25, 9995.

Briand, E., M. Salmain, C. Compère , C.M. Pradier, (2006), ―Immobilization of Protein A on SAMs for the elaboration of immunosensors.‖, Colloid. Surface. B., 53, 215.

Buchatip, S., C. Ananthanawat, P. Sithigorngul, P. Sangvanich, S. Rengpipat, V.P. Hoven, (2010), –Detection of the shrimp pathogenic bacteria, Vibrio harveyi, by a quartz crystal microbalance-specific antibody based sensor", Sensor. Actuat. B., 145, 259.

Cabrita, J.F., L.M. Abrantes, A.S. Viana, (2005), –N-hydroxysuccinimide-terminated Self-Assembled Monolayers on Gold for Biomolecules Immobilisation.", Viana, Electrochim. Acta, 50, 2117.

Campuzano, S., M. Pedrero, C. Montemayor, E. Fatás, J.M. Pingarrón, (2006), –Characterization of alkanethiol-self-assembled monolayers-modified gold electrodes by electrochemical impedance spectroscopy", J. Electroanal. Chem., 586, 112.

Caruso, F., E. Rodda, D.N Furlong, K. Niikura, Y. Okahata, (1997), –Sensor sensitivity training", Anal. Chem., 69, 2043.

Carvalhal, R.F., R.S Freire, L. T. Kubota, (2004), –Polycrystalline Gold Electrodes: A Comparative Study of Pretreatment Procedures Used for Cleaning and Thiol Self-Assembly Monolayer Formation," Electroanalysis, 17, 1251.

Casalini, R., L.M. Goldenberg, C. Pearson, M.R. Bryce, M.C. Petty, (1997) –An electrical impedance study of Langmuir - Blodgett films containing a tetrabutylammonium Ni(dmit)$_2$ complex," J. Phys. D: Appl. Phys. 30, 2928.

Chamberlin S.I., Merino E.J., Weeks K.M., (2002) –Catalysis of amide synthesis by RNA phosphodiester and hydroxyl groups," P Natl Acad Sci Usa , 99, 14688.

Chang, M. C., W. H. Douglas, (2007) –Cross-linkage of hydroxyapatite/gelatin nanocomposite using imide-based zero-length cross-linker." J Mater Sci: Mater Med, 18, 2045.

Choi J., Y. Kim, B. Oh, (2005), –The development of protein chip using protein G for the simultaneous detection of various pathogens", Ultramicroscopy, 108, 1396.

Choi, S.H., J.W. Lee, J.W. S.J. Sim, (2005), –Enhanced performance of a surface plasmon resonance immunosensor for detecting Ab–GAD antibody based on the modified self-assembled monolayers," Biosens. Bioelectron, 21, 378

Chow, E., E.L.S. Wong, T. Bocjing, Q.T. Nguten, D.B. Hibbert, J.J Gooding, (2005) –Analytical performance and characterization of MPA-Gly-Gly-His modified sensors", Sens. Actuators, B, 111, 540.

Cohen, E.R., H. Reiss., (1963), –Kinetics of Reactant Isolation. I. One-Dimensional Problems", J. Chem. Phys. 38, 680.

Collinson, M., Bowden, E.F., Tarlov, M.J., (1992) –Voltammetry of covalently immobilized cytochrome c on self-assembled monolayer electrodes." Langmuir, 8, 1247.

Cortés, J., E. Valencia, (2002), –Random sequential adsorption kinetics of dimers and trimers on geometrically disordered substrates.”, J. Colloid. Interface. Sci., 252, 256.

Cosnier S, (2005) –Affinity Biosensors Based on Electropolymerized Films.”, Electroanalysis, 17, 1701.

Creager, S.E., L.A. Hocket, G.K. Rowe, (1992), –Consequences of microscopic surface roughness for molecular self-assembly.” Langmuir, 8, 854.

Cui X., R. Pei, Z. Wang, F. Yang, Y. Ma, S. Dong, X. Yang, (2003), –Layer-by-layer assembly of multilayer films composed of avidin and biotin-labeled antibody for immunosensing”, Biosens. Bioelectron., 18, 59.

Damink, O, L.H.H., P.J. Dijkstra, M.J.A. van Luyn, P.B. van Wachem, P. Nieuwenhuis, J. Feijen, (1996) –Crosslinking of dermal sheep collagen using a water-soluble carbodiimide”, Biomaterials, 17, 765.

Dannenberger O., M. Buck, M. Grunze, (1999), –Self-Assembly of n-Alkanethiols: A Kinetic Study by Second Harmonic Generation”, J. Phys. Chem. B, 103, 2202.

Darain F., S.U. Park, Y.B. Shim, (2003), –Disposable amperometric immunosensor system for rabbit IgG using a conducting polymer modified screen-printed electrode,” Biosens. Bioelectron, 18, 773

Das, R.D., C. RoyChaudhuri, S. Maji, S. Das, H. Saha, (2009), –Macroporous silicon based simple and efficient trapping platform for electrical detection of Salmonella typhimurium pathogens.”, Biosens. Bioelectron., 24, 3215.

Dean A.K. (2008), –A piezoelectric biosensor for DNA hybridisation detection,” Teesside University. A thesis submitted in partial fulfilment of the requirements of Teesside University for the degree of Doctor of Philosophy. Middlesbrough: Teesside University.

Delayen, J. R., J. Mammosser, L. Phillips, A.T. Wu, (2001) –Alternate Electrolyte Composition for Electropolishing of Niobium Surfaces”, STAR, Report No.(s): DE2002-792481.

Díaz-González, M., D. Hernández-Santos, M.B. González-García, A. Costa-García, (2005), –Development of an immunosensor for the determination of rabbit IgG using streptavidin modified screen-printed carbon electrodes,” Talanta, 65, 565.

Ding, S.J., B.W. Chang, C.C. Wu, M.F. Lai, H.C. Chang, (2005) –Electrochemical evaluation of avidin–biotin interaction on self-assembled gold electrodes.” Electrochim. Acta, 50, 3660.

Ding, S.J., B.W.Chang, C.C. Wu, C.J.Chen, H.C. Chang, (2007), —A new method for detection of endotoxin on polymyxin B-immobilized gold electrodes.” Electrochem Commun., 9, 1206.

Dong, D., D. Zheng, F.Q. Wang, X.Q. Yang, N. Wang, Y.G. Li, L.H. Guo, J. Cheng, (2004), –Quantitative photoelectrochemical detection of biological affinity reaction: biotin-avidin interaction", Anal. Chem., 76, 499

Dong, S., J. Li, (1997), –Self-assembled monolayers of thiols on gold electrodes for bioelectrochemistry and biosensors", Bioelectrochem. Bioenerg.,42, 7.

Farace G., G. Lillie, T. Hianik, P. Payne, P. Vadgama, (2002), –Reagentless biosensing using electrochemical impedance spectroscopy.", Bioelectrochemistry, 55, 1.

Feder, J., I. Giaever, (1980), –Adsorption of ferritin.", J. Colloid Interf Sci, 78, 144.

Feder, J., (1980) –Random Sequential Adsorption.", J. Theor Biol, 87, 237.

Foulds, N.C., C.R. Lowe, (1986), –Enzyme entrapment in electrically conducting polymersimmobilization of glucose oxidase in polypyrrole and its application in amperometric glucose sensors." J. Chem. Soc., Faraday Trans. 1, 82, 1259.

Freundlich, H., (1907), –Over the adsorption in solution.", J. Phys. Chem. A., 54, 385.

Frey, B.L., R.M. Corn, (1996) –Covalent Attachment and Derivatization of Poly(L-lysine) Monolayers on Gold Surfaces As Characterized by Polarization-Modulation FT-IR Spectroscopy", Anal. Chem, 68, 3187.

Garca-Sanchez, P., A. Ramos, N. G. Green, H. Morgan, (2008) –Traveling-Wave Electrokinetic Micropumps: Velocity, Electrical Current, and Impedance Measurements," Langmuir, 24, 9361.

Ge, C., J. Liao, W. Yu, N. Gu, (2003), –Electric potential control of DNA immobilization on gold electrode." Biosens. Bioelectron., 18, 53.

Glaser, R., S. Rayat, M. Lewis, M.S. Son, S.Meyer, (1999) –Theoretical Studies in DNA Base Deamination 2. Ab Initio Study of Linear, Unimolecular Dediazoniation Paths." J. Am. Chem. Soc., 121, 6108. Gooding, J.J., Hibbert, D.B., TRAC-Trend Anal Chem, 1999, 18, 525-533.

Gooding, J.J., Hibbert, D.B., (1999) –The application of alkanethiol self-assembled monolayers to enzyme electrodes", TRAC-Trend Anal Chem, 18, 525.

Gondran,C., M. Orio, D. Rigal, B. Galland, L. Bouffier, T. Gulon, S. Cosnier, (2010), –Electropolymerized biotinylated poly (pyrrole–viologen) film as platform for the development of reagentless impedimetric immunosensors," Electrochem. Commun., 12, 311.

Grabowski, K., A. Patrykiejew, S. Sokolowski, (2002), –Monte Carlo simulation of adsorption on preadsorbed layers," Surf. Sci, 506, 47.

Green, N. M., (1963), –Avidin 3. The nature of the biotin-binding site," Biochem. J. 89, 599.

Gyepi-Garbrah S. H., R. Šilerová (2001), Probing temperature-dependent behaviour in self-assembled monolayers by ac-impedance spectroscopy, Phys. Chem. Chem. Phys., 3, 2117.

Hafaid I., A. Gallouz, W. Mohamed Hassen, A. Abdelghani, Z. Sassi, F. Bessueille, N. Jaffrezic-Renault, (2009), –Sensitivity Improvement of an Impedimetric Immunosensor Using Functionalized Iron Oxide Nanoparticles.” J. Sensors, 2009, ID 746548.

Hang, T.C., A. Guiseppi-Eli, (2004), –Frequency dependent and surface characterization of DNA immobilization and hybridization.”, Biosens. Bioelectron., 19, 1537.

Hao R., Wang D, Zhang X, Zuo G, Wei H, Yang R, Zhang Z, Cheng Z, Guo Y, Cui Z, Zhou Y, (2009), –Rapid detection of Bacillus anthracis using monoclonal antibody functionalized QCM sensor.” Biosens. Bioelectron., 24, 1330.

Hermanson G. T. (2008), –Bioconjugate Techniques,” San Diego, Academic Press.

Hassanzadeh, A., M.H. Habibi, A. Zeini-Isfahani, (2004), –Study of electronic structure of tin-doped In2O3 (ITO) film deposited on glass”, Acta Chim. Slov., 51, 507.

Hays H.C.W., P.A. Millner, M.I. Prodromidis, (2006) –Development of capacitance based immunosensors on mixed self-assembled monolayers.” Sens. Actuators B, 114, 1064.

Heineman, W. R., J. H. Thomas, A. Wijayawardhana, H. B. Halsall, T. H. Ridgway, J. W. Choi, K. W. Oh, C. Ahn, S. Dharmatilleke, P. Medis, T. H. Henderson, (2001), –BioMEMS: Electrochemical Immunoassay with Microfluidic Systems,” Anal. Sci., 17, 281.

Helmholtz. II., H., (1853), –Some laws concerning the distribution of electrical currents in conductors with applications to experiments on animal electricity”. Ann Phys-Leipzig, 89, 211.

Henderson, A.P., L.N. Seetohul, A.K. Dean, P. Russell, S. Pruneanu and Z. Ali (2009). –A Novel Isotherm, Modelling Self-Assembled Monolayer Adsorption and Structural Changes,” Langmuir, 25, 931.

Henderson, A.P., P. A. Russell, Z. Bajuszova, G. Pasirayi, Z. Ali (2010), –Macroscopic Adsorption Kinetics of EDC and NHS during Carboxylic Acid Activation,” Langmuir (submitted).

Hinrichsen, E.L., J. Feder, T. Jøssang, (1986), –The Geometry of Random Sequential Adsorption.”, J. Stat. Phys., 44, 793.

Hleli, S., A. Abdelghani, A. Tlili, (2003), –Impedance Spectroscopy Technique for DNA Hybridization” Sensors, 3, 472.

Hnaien, M., M. F. Diouani, S Helali, I. Hafaid, W. M. Hassen, N. J. Renault, A. Ghram, A. Abdelghani, (2008) –Immobilization of specific antibody on SAM functionalized gold electrode for rabies virus detection by electrochemical impedance spectroscopy", Biochem. Eng. J., 39, 443.

Hoogvliet, J.C., M. Dijksma, B. Kamp, W.P. van Bennekom, (2000) –Electrochemical Pretreatment of Polycrystalline Gold Electrodes To Produce a Reproducible Surface Roughness for Self-Assembly: A Study in Phosphate Buffer pH 7.4.", Anal. Chem., 72, 2016.

Huang, E., F. Zhou, L. Deng, (2000) –Studies of Surface Coverage and Orientation of DNA Molecules Immobilized onto Preformed Alkanethiol Self-Assembled Monolayers", Langmuir, 16, 3272.

Huberman, T., Y.Eisenberg-Domovich, G.Gitlin, T.Kulik, E.A.Bayer, M.Wilchek, O.Livnah, (2001), –Chicken Avidin Exhibits Pseudo-catalytic Properties. Biochemical, Structural, and electrostatic consequences.". J. Biol. Chem., 276, 32031.

Hytönen, V.P., J.A.E. Määttä, H. Kidron, K.K Halling, J. Hörhä, T. Kulomaa, T.K.M. Nyholm, M.S. Johnson, T.A. Salminen, M.S. Kulomaa, T.T. Airenne, (2005), –Avidin related protein 2 shows unique structural and functional features among the avidin protein family", Biotechnology, 5, 28.

Jang, L.S., H.K. Keng, (2008) –Modified fabrication process of protein chips using a short-chain self-assembled monolayer", Biomed. Microdevices, 10, 203.

Janolino, V.G., Swaisgood H.E., (1982), –Analysis and optimization of methods using water-soluble carbodiimide for immobilization of biochemicals to porous glass.", Biotechnol. Bioeng., 24, 1069.

Jones, T., –Electropolishing of precious metals," (2004), Metal Finishing, 102, 45.

Katz, E., I. Willner, –Probing Biomolecular Interactions at Conductive and Semiconductive Surfaces by Impedance Spectroscopy: Routes to Impedimetric Immunosensors, DNA-Sensors, and Enzyme Biosensors" (2003), Electroanalysis, 15, 913

Kaur, J., R.C. Boro, N. Wangoo, K. R. Singh, C. Raman Suri, (2008), –Direct hapten coated immunoassay format for the detection of atrazine and 2,4-dichlorophenoxyacetic acid herbicides", Anal. Chim. Acta., 607, 92.

Khoshman J. M., (2005), –Spectroscopic Ellipsometry Characterization of Single and Multilayer Aluminium Nitride/Indium Nitride Thin Film Systems," Ohio University.

Kim, M.G., Y.B. Shin, J.M Jung, H.S. Ro, B H Chung, (2005), –Enhanced sensitivity of surface plasmon resonance (SPR) immunoassays using a peroxidase-catalyzed precipitation reaction and its application to a protein microarray", J. Immunol Methods, 297, 125.

Kim, S. K., (2004), –Redox cycling for an in-situ enzyme labeled immunoassay on interdigitated array electrodes" A thesis submitted in partial fulfilment of the requirements of Georgia Institute of Technology for the degree of Doctor of Philosophy. USA: Georgia Institute of Technology.

Kisliuk, P., (1957), –The sticking probabilities of gases chemisorbed on the surfaces of solids." J. Phys. Chem. Solids, 3, 95.

Küster, F.W., (1894), –Contributions to the molecular weight determination of –fixed" solutions.", J. Phys. Chem., 13, 445.

Kyprianou, D., A.R. Guerreiro, M. Nirschl, I. Chianella, S. Subrahmanyam, A.P.F. Turner, S. Piletsky, (2010), –The application of polythiol molecules for protein immobilisation on sensor Surfaces", Biosens. Bioelectron, 25, 1049.

Lagergren S.,(1898), –Zur theore der sogeannten adsorption geloster satte kugliga Svenska Vetenskapsakdemiens," Handlingar, 24, 1.

Landolt, D., (1987), –Fundamental aspects of electropolishing.", Electrochim. Acta, 32, 1.

Langmuir, I., (1916), –The Constitution and Fundamental Properties of Solids and Liquids. Part I. Solids.", J. Am. Chem. Soc., 38, 2221.

Langmuir, I., (1918), –The adsorption of gases on plane surfaces of glass, mica and platinum.", J. Am. Chem. Soc., 40, 1361.

Lee, J.W., S.J. Sim, S.M. Cho, J. Lee, (2005), –Signal enhancement of surface plasmon resonance immunoassay using enzyme precipitation-functionalized gold nanoparticles: A femto molar level measurement of anti-glutamic acid decarboxylase antibody." Biosens. Bioelectron., 20, 1422.

Li, J., Cheng, G., Dong, S., (1996), –Immobilization of cytochrome c oxidase into electrode-supported lipid bilayer membranes for in vitro cytochrome c sensing.", J. Electroanal. Chem., 416, 97.

Liu, S., X. Zhang, Y. Wu, Y. Tu, L He, (2008), –Prostate-specific antigen detection by using a reusable amperometric immunosensor based on reversible binding and leasing of HRP-anti-PSA from phenylboronic acid modified electrode.", Clin. Chim. Acta, 395, 51.

Liu X., Y. Sun, D. Song, Q. Zhang, Y. Tian, H. Zhang, (2006), –Enhanced optical immuosensor based on surface plasmon resonance for determination of transferring", Talanta, 68, 1026.

Macdonald, J.R., (1987), –Impedance spectroscopy," Hoboken, USA: John Wiley and Sons, Inc

Melamed, M. D., N. M. Green, (1963), –Avidin 1. Purification and composition", Biochem. J., 89, 591

Mitchell J.S., Y. Wu, C.J. Cook, L. Main, (2006) –Estrogen conjugation and antibody binding interactions in surface plasmon resonance biosensing.", Steroids, 7, 618.

Mouffouk F., S.J. Higgins, (2006), –A biotin-functionalised poly(3,4-ethylenedioxythiophene)-coated microelectrode which responds electrochemically to avidin binding," Electrochem Commun, 8, 15.

Mura-Galelli, M.J., J.C. Voegel, S. Behr, E.F. Bres, P.Schaaf, (1991), –Adsorption/desorption of human serum albumin on hydroxyapatite: a critical analysis of the Langmuir model.", P. Natl. Acad. Sci. USA, 88, 5557.

Neish C. S., I.L. Martin, R.M. Henderson, J. M. Edwardson, (2002), –Direct visualization of ligand-protein interactions using atomic force microscopy" Br. J. Pharmacol. 135, 1943.

Norlin A., J. Pan, C. Leygraf, (2002), –Investigation of interfacial capacitance of Pt, Ti and TiN coated electrodes by electrochemical impedance spectroscopy," Biomol. Eng. 19, 67.

Nowall W.B., N. Dontha, W.G. Kuhr, (1998), –Electron transfer kinetics at a biotin/avidin patterned glassy carbon electrode." Biosens. Bioelectron., 13, 1237.

Nuzzo, R.G., D.L. Allara, (1983), –Adsorption of Bifunctional Organic Disulfides on Gold Surfaces", J. Am. Chem. Soc., 105, 4481.

Oellerich, M., (1980), –Enzyme Immunoassays in Clinical Chemistry: Present Status and Trends," J. Clin. Chem. Clin. Biochem., 18, 197

Oesch U., J. Janata, (1983), –Electrochemical study of gold electrodes with anodic oxide films—I. Formation and reduction behaviour of anodic oxides on gold.", Electrochim. Acta, 28, 1237

Ouerghi, O., A. Touhami, N. Jaffrezic-Renault, C. Martelet, H. Ben-Ouada, S. Cosnier, (2002), –Impedimetric Immunosensor Using Avidin-Biotin for Antibody Immobilization", Bioelectrochemistry, 56, 131.

Palmieri, V., V. Rampazzo, (2007), –Automated Electropolishing." Unpublished.

Sciencelab.com, Inc, 2005, –Perchloric Acid, 70%, Reagent, ACS," (online) Available at: <http://www.sciencelab.com/page/S/PVAR/10423/SLP4492>

Pomeau, Y., (1980), –Some asymptotic estimates in the random parking problem." J. Phys. A: Math. Gen., 13, L193.

Pravda, M., C. O'Meara, G. Guilbault, (2001), –Polishing of screen-printed electrodes improves IgG adsorption", Talanta, 54, 887.

Pruneanu, S., A. Boughriet, A. Henderson, C. Malins, Z. Ali, Liliana Olenic (2008), –Impedimetric Measurements for Monitoring Avidin-Biotin Interaction on Self-Assembled Monolayer," Particul. Sci Technol, 26, 136.

Ramsden, J.J., (1993), –Concentration scaling of protein deposition kinetics." Phys Rev Lett., 71, 295.

Ratner, B. D., (1993), –New ideas in biomaterials science - a path to engineered biomaterials", J. Biomed. Mater. Res, 27, 837.

Rényi, A., (1958), –On a One-Dimensional Problem Concerning Random Space-Filling", Publ. Math. Inst. Hung. Acad. Sci., 3, 109.

Ribaut, C., K. Reybier, B. Torbiero, J. Launay, A. Valentin, O. Reynes, P.-L. Fabre, F. Nepveu, (2008), –Strategy of red blood cells immobilisation onto a gold electrode: Characterization by electrochemical impedance spectroscopy and quartz crystal microbalance.", IRBM, 29, 141.

Ricci, S.M., J. Talbot, P. Viot, (1994), –Computation of the free area in a 2-D configuration of anisotropic particles", Mol. Simul., 13, 1.

Roussel L. Y., D. J. Stokes, I. Gestmann, M. Darus, R. J. Young, (2009), –Extreme high resolution scanning electron microscopy (XHR SEM) and beyond," Proc. of SPIE 7378, 73780W-1

Rubio-Gonzalez, C., M.T. Fernandez-Abedul, A. Costa-Garcia, (1999), –Comparative electrochemical behaviour of biotin hydrazide and photobiotin. Importance in the development of biosensors.", Biosens. Bioelectron., 14, 729

Sapper, A., B. Reiss, A. Janshoff, Joachim Wegener, (2006), –Adsorption and Fluctuations of Giant Liposomes Studied by Electrochemical Impedance Measurements," Langmuir, 22, 676.

Sam, S., L. Touahir, J. Salvador Andresa, P. Allongue, J.-N. Chazalviel, A. C. Gouget-Laemmel, C. Henry de Villeneuve, A. Moraillon, F. Ozanam, N. Gabouze, S. Djebbar, (2010), –Semiquantitative Study of the EDC/NHS Activation of Acid Terminal Groups at Modified Porous Silicon Surfaces," Langmuir, 26, 809.

Savitskii, E.M. and A. Prince, (1989), –Handbook of Precious Metals", New York: Taylor & Francis Group.

Schaaf, P., A. Johner, J. Talbot, (1991), –Asymptotic behavior of particle deposition", Phys. Rev. Lett., 66, 1603.

Schaaf, P., P. De´jardin, A. Johner, A. Schmitt, (1992), –Characteristic time scales for the adsorption process for fibrinogen on silica.", Langmuir, 8, 514.

Schasfoort R.B.M., A. J. Tudos, (2008), –Handbook of Surface Plasmon Resonance," Cambridge, RSC Publishing.

Schreiber, F., (2000) –Structure and growth of self-assembling monolayers.", Prog. Surf. Sci., 65, 151.

Sehgal, D., I.K.Vijay, (1994) –A method for the high efficiency of water-soluble carbodiimide-mediated amidation." Anal. Biochem., 218, 87.

Shimoni L., J.P. Glusker, (1995), –Hydrogen bonding motifs of protein side chains: descriptions of binding of arginine and amide groups," Protein Sci., 4, 65

Song, X., B.I. Swanson, (2001), –Rapid assay for avidin and biotin based on fluorescence quenching .", Anal. Chim. Acta., 442, 79

Staros, J.V., Wright, R.W., Swingle, D.M., (1986), "Enhancement by N-hydroxysulfosuccinimide of water-soluble carbodiimide-mediated coupling reactions." Anal. Biochem., 156, 220.

Stewart, G. N. (1899), –Changes produced by the growth of bacteria in the molecular concentration and electrical conductivity of culture media," J. Exp. Medicine, 4, 235.

Striemer, C.C., T.R. Gaborski, J.L. McGrath, P.M. Fauchet (2007), –Charge and size based separation of Macromolecules using ultrathin silicone membranes," Nature, 445, 749.

Štulik, K., C. Amatore, K. Holub, V. Mareček, W. Kutner, (2000), –Microelectrodes. definitions, characterization, and applications", Pure Appl. Chem., 72, 1483.

Sugawara, K., R. Kato, T. Shirotori, H Kuramitz, S Tanaka, (2002) –Voltammetric behavior of avidin_/biotin interaction at a biotin/thionine modified Au electrode" J. Electroanal Chem 536, 93.

Sugawara, K., S. Hoshi, K. Akatsuka, S. Tanaka, (1996), –Electrochemical evaluation of avidin-biotin interaction using N-iodoacetyl-N-biotinylhexylenediamine", Bioelectrochem. Bioenerg., 39, 309.

Swendsen, R.H., (1981) –Dynamics of random sequential adsorption," Phys. Rev. A: At. Mol. Opt. Phys., 24, 504.

Talbot, J., G. Tarjus, P.R. Van Tassel, P.Viot, (2000), –From car parking to protein adsorption: An overview of sequential adsorption processes," Colloid. Surface. A, 165, 287.

Tlili, A., A. Abdelghani , S. Ameur, N. Jaffrezic-Renault, (2006), –Impedance spectroscopy and affinity measurement of specific antibody–antigen interaction." Mat. Sci. Eng. C., 26, 546.

Turrell G., J. Corset, (1996), –Raman Microscopy: Developments and Applications,” New York, Elsevier.

Tweedie, M., R. Subramanian, I. Craig, E.T. McAdams and J.A.D. McLaughlin, (2006), –Fabrication of impedimetric sensors for label-free Point-of-Care immunoassay cardiac marker systems, with microfluidic blood flow delivery, and results telemetry to PDA,” Nanotech, 2, 236.

Umana, M., J. Waller, (1986), –Protein modified systems. The glucose oxidase/polypyrrole systems”, Anal. Chem., 58, 2979.

Van Weemen, B.K., Schuurs AHWM., (1971), –Immunoassay using antigen-enzyme conjugates,” FEBS Letts, 15, 232.

Wang, J.S., (1998) –Random sequential adsorption, series expansion and Monte Carlo simulation”, Physica, 254, 179.

Wang, Z., Y Tu, S Liu, (2008), –Electrochemical immunoassay for fetoprotein through a phenylboronic acid monolayer on gold”, Talanta, 77, 815.

Ward, C., M.R.A. Morgan, (1993), "Food Immunoassay," Nutr Food Sci, 89, 2.

Wissink, M.J.B., R. Beernink, J.S. Pieper, A.A. Poot, G.H.M. Engbers, T Beugeling, W.G. van Aken, J. Feijen, (2001), –Binding and release of basic fibroblast growth factor from heparinized collagen matrices.” Biomaterials, 22, 2291.

Weber, P.C., D.H. Ohlendorf, J.J. Wendoloski, F.R. Salemme, (1989), –Structural origins of high-affinity biotin binding to streptavidin”, Science, 243, 85.

Yalow, R.S., S.A. Berson, (1960), –Immunoassay of endogenous plasma insulin in man,” J. Clin. Invest., 39, 1157.

Yang H.,, R. Yuan, Y. Chai, Y. Zhuo, H. Su , (2010), –Electrochemical immunoassay for human chorionic gonadotrophin based on Pt hollow nanospheres and silver/titanium dioxide nanocomposite matrix,” J. Chem Technol Biot, 85, 577

Yang, Z., A. Gonzalez-Cortes, G. Jourquin, J.C. Vire, J.M. Kauffman, J.L. Delplancke, (1995), –Analytical application of self assembled monolayers on gold electrodes: critical importance of surface pretreatment”, Biosens. Bioelectron., 10, 789.

Zhang, Y., H. Wang, J. Nie, Y. Zhang, G. Shen, R. Yu, (2009), –Individually addressable microelectrode arrays fabricated with gold-coated pencil graphite particles for multiplexed and high sensitive impedance immunoassays”, Biosens. Bioelectron. 25, 34.

Zhou, C., A.V. Walker, (2006), –Dependence of Patterned Binary Alkanethiolate Self-Assembled Monolayers on –UV-Photopatterning” Conditions and Evolution with Time, Terminal Group, and Methylene Chain Length.” Langmuir, 22, 11420.

Appendix 1: Simulated Equivalent circuit elements in "ZView2" by Scribner associates, Inc.

Even though construction of an equivalent circuit is relatively simple, provided one has an appropriate knowledge of the electrical properties of the electrochemical system under consideration and has an understanding of typical equivalent circuits employed, fitting parameters to accurately model experimental data can often prove a time consuming process. For this reason simulations have been created which attempt to fit theoretical impedance data from a user-specified equivalent circuit with values very roughly approximating that of the finished model. The equivalent circuit values are then altered by the simulation program software until modelled impedance data provides a fit to experimental data.

For the sake of simplicity, equivalent circuit variables independent of frequency are often grouped together in –ZView2" and assigned coefficients such as R, T and P, thereby reducing the number of variables involved in the necessary computer modelling iterations and allowing fast and accurate modelling. In the case of the CPE, T and P simply replace Y_0 and n respectively (equation (A1.1)), however, in the case of ZView2 –Short Circuit Terminus Warburg impedance" (equation (A1.2)), element R is a constant formed as a result of Warburg impedance element equation simplification and is dictated by the Warburg coefficient. In this instance, T is defined in equation (equation (A1.3)), where L is the diffusion layer thickness and D is the diffusion coefficient of redox ions through the diffusion layer media and P is 0.5 for experimental data with ideal mass transfer.

$$|Z| = \frac{1}{T(j\omega)^P} \tag{A1.1}$$

$$|Z| = \frac{R \tanh\left[(jT\omega)^P\right]}{(jT\omega)^P} \tag{A1.2}$$

$$T = \frac{L^2}{D} \tag{A1.3}$$

Unfortunately, not all electrochemical cells display ideal linear diffusion and as a result phase angle diverges from 45^{o}. Thus, the parameter P in equation (A1.2) can occupy any value between 0 and 1, although it typically remains approximately equal to 0.5 in fitted aqueous electrochemical models. In spite of the accuracy of the Short Circuit Terminus Warburg impedance element for an aqueous electrochemical system, other electrochemical systems require the application of a different Warburg element called an ~~–O~~pen Circuit Terminus," which exhibits a phase angle of 45^{o} initially but changes to exhibit pure capacitive behaviour beneath a particular frequency. As the Open Circuit Terminus Warburg element is not relevant to this study it will not be discussed in further detail nor will the other types of simulated impedance elements unrelated to the electrochemical system under analysis in this study.

As the constants of R, T and P for each simulated equivalent circuit component vary depending on electrochemical system properties and kinetics, trends can be identified in these constants for varying monolayer immersion periods, which allows trends in individual physical properties of the system to be deduced.

Appendix 2: Chapter 7 Model and experimental data for adsorption of EDC and NHS to an MPA modified surface, during activation.

Table A2.1: Fitted values and chi squared values (χ^2) for the PTCS-Kisliuk model, showing goodness of fit

Adsorption temperature (C)	R_1^{∞}	R_2^{∞}	k_{E1}	k_{E2}	φ_1	φ_2	χ^2
4	3.478	0.1531	0	5.053	0.1953	0.0654	0.02604
15	1.412	0.1531	63.22	148.8	0.2115	0.11032	0.8828
18	0.0946	0.3781	223.5	20.33	0.4382	0.0749	0.1776
22	0.0503	0.6505	330.7	7.696	1.364	0.1336	0.02583
25	0.4620	0.1054	58.24	99.31	1.308	0.05078	0.5961
27	0.5650	0.1054	52.91	101.4	0.5367	0.05076	0.09572
30	0.5764	0.1211	52.61	115.2	0.1090	0.05063	0.007997

Table A2.2: Experimental and calculated impedances for the fitted PTCS-Kisliuk model at 27 ^{o}C.

	Normalised impedance values		
Immersion time (hrs)	**Experimental Values**	**Predicted Values**	**Error (abs)**
0	0	0	0
0.02	0.0152	0.00821	4.90×10^{-5}
0.063	0.0270	0.0524	0.000642
0.08	0.127	0.0860	0.00166
0.19	0.429	0.435	3.29×10^{-5}
0.28	0.469	0.454	0.000219
0.37	0.350	0.370	0.000422
0.46	0.309	0.254	0.002936
0.55	0.159	0.155	1.58×10^{-5}
0.64	0.126	0.0961	0.000897
0.73	0.0434	0.0690	0.000654
0.82	0.0702	0.0578	0.000154
0.91	0.0302	0.0535	0.000542
1	0.0385	0.0518	0.000176
1.5	0.0466	0.0508	1.75×10^{-5}
1.667	0.0288	0.0508	0.000481
		Average Error	0.000747

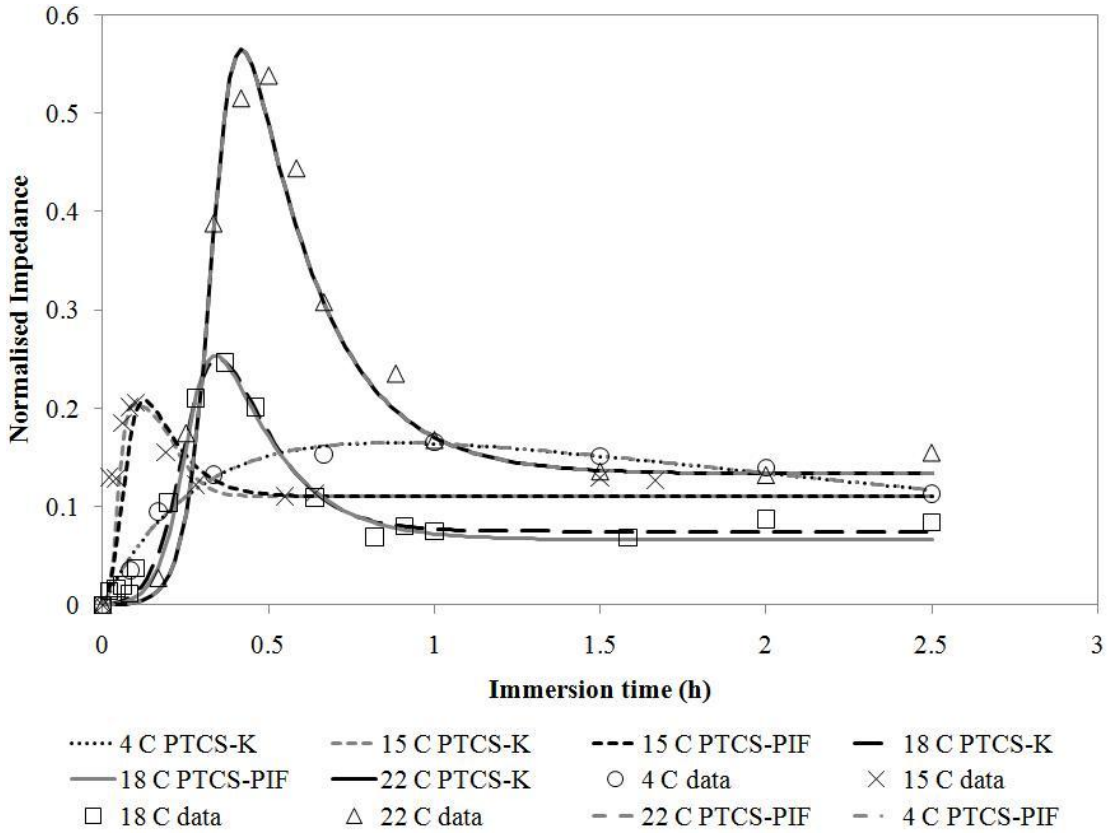

Figure A2.1: Normalised Raw EIS data at temperatures less than the Gyepi-Garbrah critical temperature (Tc) (Gyepi-Garbrah and Šilerová, 2001) of the MPA monolayer. Discrete points show the actual experimental data, the lines show the calculated impedance from the fitted PTCS-Kisliuk model and PTCS-PIF model.

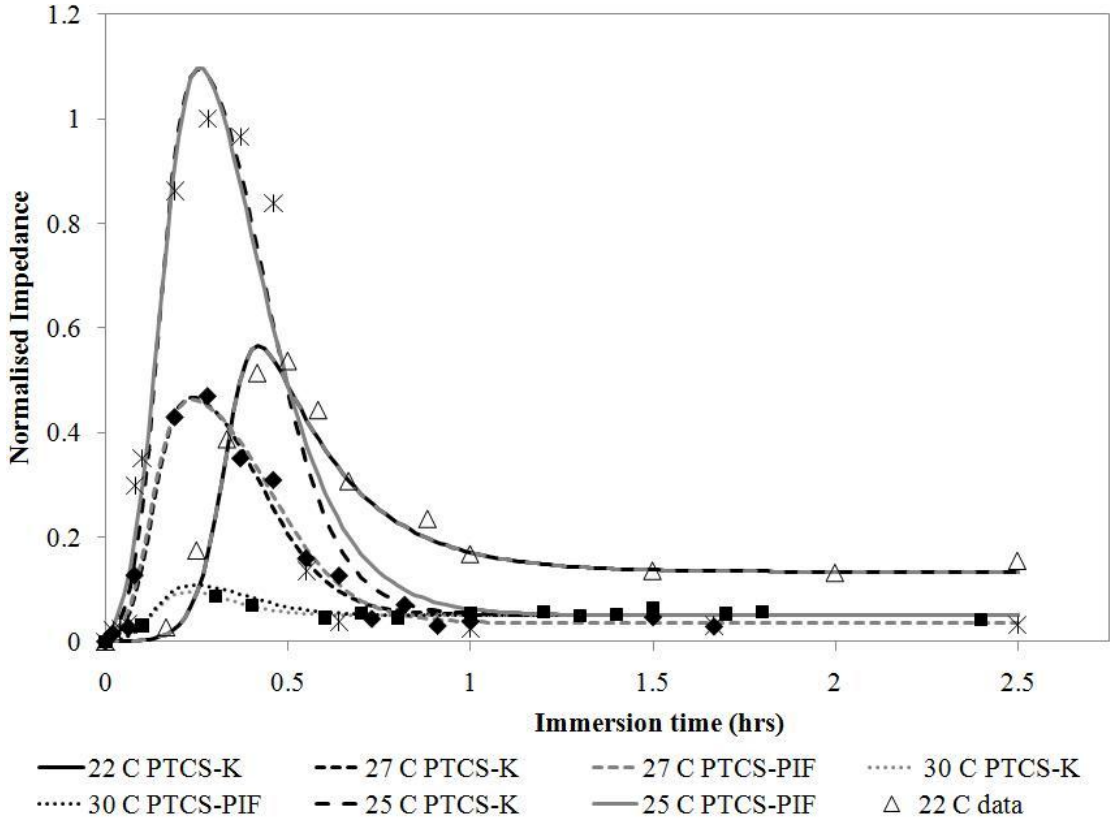

Figure A2.2: Raw EIS data at temperatures greater than the Gyepi-Garbrah critical temperature (Tc) (Gyepi-Garbrah and Šilerová, 2001) of the MPA monolayer. The isotherm at 22 °C is also included for comparison. The discrete points show the actual experimental data. The lines show the calculated impedance from the fitted PTCS-Kisliuk model and the PTCS-PIF model.

Table A2.3: Fitted values and chi squared values (χ^2) for the PTCS-PIF model, showing goodness of fit.

Adsorption temperature (C)	k_{R1}	k_{R2}	k''_{I1}	k''_{I2}	φ_1	φ_2	χ^2
4	3.496	0.1478	0	0.7924	0.195	0.065	0.005916
15	2.239	2.040	43.00	10.10	0.2914	0.1103	0.8038
18	0.03322	1.539	24.96	4.402	0.6748	0.0663	0.4016
22	0.003651	2.216	25.85	2.515	2.141	0.1333	0.4687
25	0.6428	0.4391	21.34	7.278	1.652	0.05000	0.4255
27	0.7020	0.1253	29.25	9.385	0.5296	0.03514	0.06710
30	0.5274	0.1250	29.99	11.53	0.1220	0.05087	0.008938

Table A2.4: Experimental and calculated impedances for the fitted PTCS-PIF model at 27 ^{o}C

	Normalised impedance values		
Immersion time (hrs)	**Experimental Values**	**Predicted Values**	**Error (abs)**
0	0	0	0
0.02	0.0152	0.0100	2.75×10^{-5}
0.063	0.0270	0.0615	0.001186
0.08	0.127	0.0990	0.00077
0.19	0.429	0.436	4.52×10^{-5}
0.28	0.469	0.451	0.00031
0.37	0.350	0.380	0.000926
0.46	0.309	0.278	0.000918
0.55	0.159	0.179	0.000391
0.64	0.126	0.108	0.000325
0.73	0.0434	0.069	0.000652
0.82	0.0702	0.0501	0.000406
0.91	0.0302	0.0416	0.00013
1	0.0385	0.0379	3.64×10^{-7}
1.5	0.0466	0.0352	0.00013
1.667	0.0288	0.0351	4×10^{-5}
		Average Error	0.000391

Appendix 3: Model and experimental data for adsorption of Streptavidin onto an activated MPA monolayer

Table A3.1: Experimental and calculated impedances for the fitted RSA model

	Normalised impedance values		
Immersion time (hrs)	**Experimental Values**	**Predicted Values**	**Error (abs)**
0.0000	0.0000	0.0000	0.0000
0.0833	0.0298	0.1926	0.1628
0.1667	0.0726	0.3230	0.2504
0.2500	0.1391	0.4171	0.2780
0.3333	0.3006	0.4883	0.1877
0.5000	0.4543	0.5887	0.1344
0.5833	0.5453	0.6255	0.0802
0.6667	0.6483	0.6562	0.0079
0.7500	0.6714	0.6822	0.0108
0.8333	0.7361	0.7046	0.0314
0.9167	0.8507	0.7241	0.1267
1.0833	0.9594	0.7562	0.2033
1.1667	0.8668	0.7696	0.0973
1.2500	0.9271	0.7816	0.1456
1.3333	0.9981	0.7924	0.2057
1.5000	0.9392	0.8111	0.1281
1.7500	0.9710	0.8336	0.1374
2.0000	0.8513	0.8513	0.0000
2.5833	1.0000	0.8774	0.1226
		Average Error	0.1283

Table A3.2: Experimental and calculated impedances for the fitted Lagargren model

	Normalised Impedance Values		
Immersion time (hrs)	**Experimental Values**	**Predicted Values**	**Error (abs)**
0.0000	0.0000	0.0000	0.0000
0.0833	0.0298	0.1272	0.0119
0.1667	0.0726	0.2382	0.0624
0.2500	0.1391	0.3351	0.3351
0.3333	0.3006	0.4197	0.0347
0.5000	0.4543	0.5579	0.1036
0.5833	0.5453	0.6141	0.0688
0.6667	0.6483	0.6632	0.0149
0.7500	0.6714	0.7060	0.0346
0.8333	0.7361	0.7434	0.0073
0.9167	0.8507	0.7761	0.0747
1.0833	0.9594	0.8294	0.1300
1.1667	0.8668	0.8511	0.0157
1.2500	0.9271	0.8700	0.0571
1.3333	0.9981	0.8866	0.1116
1.5000	0.9392	0.9136	0.0256
1.7500	0.9710	0.9425	0.0284
2.0000	0.8513	0.9618	0.1105
2.5833	1.0000	0.9831	0.0169
		Average Error	0.0691

Table A3.3: Experimental and calculated impedances for the fitted Kisliuk model

	Normalised Impedance Values		
Immersion time (hrs)	**Experimental Values**	**Predicted Values**	**Error (abs)**
0.0000	0.0000	0.0000	0.0000
0.0833	0.0298	0.0546	0.0247
0.1667	0.0726	0.1194	0.0468
0.2500	0.1391	0.1940	0.0549
0.3333	0.3006	0.2767	0.0239
0.5000	0.4543	0.4543	0.0000
0.5833	0.5453	0.5416	0.0037
0.6667	0.6483	0.6229	0.0254
0.7500	0.6714	0.6958	0.0244
0.8333	0.7361	0.7587	0.0227
0.9167	0.8507	0.8114	0.0393
1.0833	0.9594	0.8885	0.0709
1.1667	0.8668	0.9154	0.0485
1.2500	0.9271	0.8700	0.0571
1.3333	0.9981	0.8866	0.1116
1.5000	0.9392	0.9732	0.0339
1.7500	0.9710	0.9889	0.0180
2.0000	0.8513	0.9955	0.1442
2.5833	1.0000	0.9992	0.0008
		Average Error	0.0417

Table A3.4: Experimental and calculated impedances for the fitted PIF model

	Normalised Impedance Values		
Immersion time (hrs)	**Experimental Values**	**Predicted Values**	**Error (abs)**
0.0000	0.0000	0.0000	0.0000
0.0833	0.0298	0.0236	0.0063
0.1667	0.0726	0.0851	0.0125
0.2500	0.1391	0.1706	0.0315
0.3333	0.3006	0.2675	0.0331
0.5000	0.4543	0.4600	0.0057
0.5833	0.5453	0.5453	0.0000
0.6667	0.6483	0.6204	0.0279
0.7500	0.6714	0.6851	0.0137
0.8333	0.7361	0.7399	0.0038
0.9167	0.8507	0.7859	0.0649
1.0833	0.9594	0.8557	0.1038
1.1667	0.8668	0.8817	0.0149
1.2500	0.9271	0.9031	0.0240
1.3333	0.9981	0.9207	0.0774
1.5000	0.9392	0.9469	0.0077
1.7500	0.9710	0.9710	0.0000
2.0000	0.8513	0.9841	0.1328
2.5833	1.0000	0.9953	0.0047
		Average Error	0.0314

Appendix 4: Model and experimental data for adsorption of Biotinylated IgG onto a Streptavidin monolayer

Table A4.1: Experimental and calculated impedances for the fitted RSA model

Time (hrs)	Normalised Impedance values	Predicted Impedance values	Error
0	0.00	0	0
0.05	0.175	0.275	0.0997
0.116667	0.379	0.470	0.0912
0.166667	0.418	0.557	0.1404
0.25	0.668	0.655	0.0127
0.5	0.941	0.792	0.0068
0.75	0.798	0.851	0.0906
1	0.969	0.884	0.0850
1.5	1.000	0.919	0.0807
		Average	**0.0675**

Table A4.2: Experimental and calculated impedances for the fitted Lagergren model

Time (hrs)	Normalised Impedance values	Predicted Impedance values	Error
0	0.00	0	0
0.05	0.175	0.172	0.0032
0.116667	0.379	0.357	0.0220
0.166667	0.418	0.467	0.0492
0.25	0.668	0.611	0.0564
0.5	0.941	0.849	0.0506
0.75	0.798	0.941	2.204E-12
1	0.969	0.977	0.0085
1.5	1.000	0.997	0.0034
		Average	**0.0215**

Table A4.3: Experimental and calculated impedances for the fitted Kisliuk model

Time (hrs)	Normalised Impedance values	Predicted Impedance values	Error
0	0.00	0	0
0.05	0.175	0.175436	$4.37x10^{-09}$
0.116667	0.379	0.362436	0.016138
0.166667	0.418	0.474287	0.056072
0.25	0.668	0.618826	0.04888
0.5	0.941	0.854707	0.056434
0.75	0.798	0.944618	0.00335
1	0.969	0.97889	0.010248
1.5	1.000	0.996933	0.003067
		Average	**0.0216**

Table A4.4: Experimental and calculated impedances for the fitted PIF model

Time (hrs)	Normalised Impedance values	Predicted Impedance values	Error
0	0.00	0	0
0.05	0.175	0.160	0.016
0.116667	0.379	0.360	0.019
0.166667	0.418	0.491	0.073
0.25	0.668	0.668	0.000
0.75	0.941	0.924	0.125
0.5	0.798	0.984	0.043
1	0.969	0.997	0.028
1.5	1.000	1.000	1.251E-04
		Average	**0.0338**

Appendix 5: Model and Experimental data for direct adsorption of IgG on gold substrates.

Table A5.1: Experimental and calculated impedances for the fitted Kisliuk model for the 4 °C isotherm.

Time	Normalised Experimental impedance value	calculated value	Error
0	0	0	0
0.083333	0.002636	0.004681	0.002045
0.166667	0.012386	0.010498	0.001888
0.333333	0.035557	0.026076	0.009481
0.5	0.06259	0.047067	0.015523
0.75	0.08514	0.08485	0.00029
1	0.118657	0.11964	0.000984
1.5	0.145326	0.155961	0.010634
2	0.152421	0.164865	0.012443
2.5	0.16757	0.166603	0.000967
		Average	**0.005426**

Table A5.2: Experimental and calculated impedances for the fitted PIF model for the 4 °C isotherm

Time	Normalised Experimental impedance value	Predicted value	Error
0	0	0	0
0.083333	0.002636	0.003158	0.000523
0.166667	0.012386	0.011318	0.001068
0.333333	0.035557	0.035557	8.33×10^{-10}
0.5	0.06259	0.06205	0.00054
0.75	0.08514	0.095766	0.010626
1	0.118657	0.119578	0.000921
1.5	0.145326	0.145316	1.01E-05
2	0.152421	0.155629	0.003208
2.5	0.16757	0.159629	0.007941
		Average	0.002484

Table A5.3: Experimental and calculated impedances for the fitted Kisliuk model for the 40 °C isotherm.

Time	Normalised Experimental impedance value	Predicted value	Error
0	0	0	0
0.066667	0.1132	0.160222	0.047022
0.116667	0.413939	0.278877	0.135062
0.2	0.465419	0.457249	0.00817
0.283333	0.53414	0.594168	0.060028
0.4	0.657106	0.703539	0.046432
0.6	0.710086	0.722314	0.012229
0.8	0.597859	0.648697	0.050837
1	0.610751	0.560531	0.05022
1.5	0.393046	0.39538	0.002335
2.5	0.260142	0.274148	0.336603
3	0.257794	0.257794	0.135251
		Average	0.073682

Table A5.4: Experimental and calculated impedances for the fitted PTCS-PIF model for the 40 °C isotherm

Time	Normalised Experimental impedance value	Predicted value	Error
0	0	0	0
0.066667	0.1132	0.113453	0.000253
0.116667	0.413939	0.247824	0.166115
0.2	0.465419	0.438516	0.026903
0.283333	0.53414	0.566711	0.032572
0.4	0.657106	0.661485	0.004379
0.6	0.710086	0.682856	0.027229
0.8	0.597859	0.62613	0.028270
1	0.610751	0.551951	0.058800
1.5	0.393046	0.401556	0.008510
2.5	0.260142	0.278197	0.018055
3	0.257794	0.259157	0.001362
		Average	0.031037

Appendix 6: Publications resulting from this thesis